



Forschungszentrum Karlsruhe
in der Helmholtz-Gemeinschaft

Wissenschaftliche Berichte
FZKA 7095

Land Surface Temperature and Emissivity Retrieval from Satellite Measurements

P. Dash

Institut für Meteorologie und Klimaforschung

Februar 2005

Forschungszentrum Karlsruhe

in der Helmholtz-Gemeinschaft

Wissenschaftliche Berichte

FZKA 7095

**Land surface temperature and emissivity retrieval from
satellite measurements***

Prasanjit Dash

Institut für Meteorologie und Klimaforschung

*Von der Fakultät für Physik der Universität Karlsruhe (TH)

genehmigte Dissertation

Forschungszentrum Karlsruhe GmbH, Karlsruhe

2005

Impressum der Print-Ausgabe:

**Als Manuskript gedruckt
Für diesen Bericht behalten wir uns alle Rechte vor**

**Forschungszentrum Karlsruhe GmbH
Postfach 3640, 76021 Karlsruhe**

**Mitglied der Hermann von Helmholtz-Gemeinschaft
Deutscher Forschungszentren (HGF)**

ISSN 0947-8620

urn:nbn:de:0005-070957

Land surface temperature and emissivity retrieval from satellite measurements

Zur Erlangung des akademischen Grades eines
DOKTORS DER NATURWISSENSCHAFTEN

von der Fakultät für Physik der
Universität Karlsruhe (TH)

genehmigte
DISSERTATION

von
Prasanjit Dash
aus Cuttack (Indien)

Tag der mündlichen Prüfung	: 5. November 2004
Referent	: Prof. Dr. Herbert Fischer
Korreferent	: Prof. Dr. Christoph Kottmeier

Abstract

Land surface temperature (LST) is maintained by the incoming solar and longwave irradiation, the outgoing terrestrial infrared radiation, the sensible and latent heat flux, and the ground heat flux. Therefore, LST is a good indicator of the energy balance at the Earth's surface. Long-term and reliable estimates of LST are required for multiple purposes, *e.g.* as input to general circulation models, numerical weather prediction, climate change detection, vegetation health monitoring, change detection related to desertification processes *etc.* Only satellite-based radiance measurements provide the temporal coverage and spatial resolution required to run these models and analyze the processes. For measurements in the atmospheric windows, the top-of-the-atmosphere (TOA) radiance is dominated by surface-leaving radiance. Therefore, LST can be estimated from radiances measured by satellite sensors.

The sensor-specific TOA measurements are influenced by surface properties (LST and emissivity) and atmospheric absorption and transmission. Besides the complications due to atmospheric attenuation, a direct separation of LST and emissivity from passive radiometric measurements alone is not feasible because the problem is underdetermined: for a sensor with N spectral channels, there are N measurements but $N + 1$ unknowns (*i.e.* N spectral emissivities and LST). In order to make this ill-posed problem solvable, different assumptions for regularization of the underdetermined condition are made.

This work is a contribution to the field of spaceborne remote sensing for measurement of Earth's surface temperature and emissivity from passive radiometry. At the *Institute of Meteorology and Climate Research, Forschungszentrum Karlsruhe/University of Karlsruhe, Germany*, NOAA AVHRR data are archived at the *Meteorological Satellite Applications (MSA)* group since several years and MSG SEVIRI data are received from 2004 using a *High Rate User Station*. The aim of this study was to select an appropriate method for estimating LST, which necessitates emissivity estimation as a pre-requisite, and establish an operational set-up with the method adapted to NOAA AVHRR and MSG SEVIRI data.

The temperature independent thermal infrared spectral indices (TISI) method, which is a physical method, was employed for emissivity estimation, and subsequently LST and emissivity were decoupled from surface radiances. A physical method was approved, rather than methods based on empirical relationships which could be easily implemented, in order to capture the emissivity dynamics for various land surface types. During daytime, reflected solar irradiance and surface emission at $\sim 3.8 \mu\text{m}$ are approximately equal. The reflectivity is derived using atmospherically corrected surface radiances and a combination of day-night radiance ratios (TISI) between two channels. In order to resolve the underdetermination, it was assumed that emissivity remains constant for day and night and land surface behaves like a Lambertian surface. The TISI method was adapted to NOAA 9-16 AVHRR channels and MSG-1 SEVIRI channels. A numerical analysis was performed with simulated surface radiances showing that the achievable accuracy is better than 1.5 K – 2 K for LST and about 0.005 for emissivity (AVHRR channel 5) independent of surface type. The major source of error could be improper atmospheric information, because the atmospheric corrections cannot be better than the supplied information. However, it was assumed that atmospheric information used in the present study was correct. The method was applied to AVHRR data for a large part of central Europe, and for different days in order to observe seasonal differences. Additionally, a simple normalized difference vegetation index (NDVI)-based method for emissivity estimation was tuned for the study area using TISI-based emissivity as an input and results from both the approaches were intercompared.

Bestimmung der Temperatur und des Emissionsvermögens aus Satellitenmessungen

Zusammenfassung

Die Landoberflächentemperatur (LST – land surface temperature) wird durch die solare und langwellige Einstrahlung, die ausgestrahlte, terrestrische Infrarotstrahlung, den sensiblen und latenten Wärmefluss, sowie den Wärmefluss im Boden bestimmt. Deswegen ist die LST ein guter Indikator für das Energiegleichgewicht am Erdboden. Langfristige und zuverlässige Schätzungen der LST werden für viele Zwecke benötigt, z.B. als Eingabe für Modelle der globalen atmosphärischen Zirkulation, für numerische Wettervorhersagen, zur Erkennung von Klimaveränderungen, zur Überwachung des Vegetationszustandes, zur Erkennung von Veränderungen, die mit Desertifikationsprozessen verknüpft sind, *etc.* Nur satellitengestützte Strahlungsmessungen haben die zeitliche und räumliche Auflösung, die die Modelle und die Analyse der Prozesse benötigen. In den Spektralbereichen der „atmosphärischen Fenster“ wird die am Oberrand der Atmosphäre (TOA – top-of-atmosphere) gemessene Strahlung durch die von der Oberfläche emittierte Strahlung dominiert. Deshalb kann die LST aus satellitengestützten Messungen der elektromagnetischen Strahlung abgeleitet werden.

Die sensorspezifischen TOA-Messungen sind ein Ergebnis von Oberflächeneigenschaften (LST und Emissionsvermögen) und atmosphärischer Emission, Absorption und Transmission. Neben den durch den Einfluss der Atmosphäre verursachten Schwierigkeiten ist außerdem eine direkte Trennung von LST und Emissionsvermögen, die allein auf passiven, radiometrischen Messungen basiert, nicht durchführbar, weil das Problem unterbestimmt ist: Ein Sensor mit N spektralen Kanälen liefert N -Messungen, aber es sind N spektrale Emissionsvermögen und eine LST zu bestimmen, also $N + 1$ Unbekannte. Um dieses schlecht gestellte Problem zu lösen, werden in der Literatur verschiedene Annahmen zur Regularisierung gemacht.

Diese Arbeit ist ein Beitrag im Bereich der weltraumgestützten Fernerkundung zur Bestimmung der Oberflächentemperatur und des Emissionsvermögens der Erde aus passiven, radiometrischen Messungen. Die Gruppe *Meteorologische Satelliten Anwendungen* (MSA) am *Institut für Meteorologie und Klimaforschung, Forschungszentrum Karlsruhe / Universität Karlsruhe, Deutschland*, archiviert NOAA AVHRR - Daten und seit 2004 MSG SEVIRI – Daten, die über eine „High Rate User Station“ empfangen werden. Das Ziel dieser Arbeit war es, eine geeignete Methode zur Ableitung der LST zu finden, was eine Ermittlung des Emissionsvermögens voraussetzt, und diese Methode an NOAA AVHRR und MSG SEVIRI-Daten anzupassen und für einen operationellen Betrieb zu implementieren.

Die Temperatur unabhängige „Thermal Infrared Spectral Indices“ (TISI) Methode wurde zur Schätzung des Emissionsvermögens eingesetzt. Danach wurden die Anteile der LST und des Emissionsvermögens an der Oberflächenstrahlung voneinander entkoppelt. Es wurde eine physikalische statt einer leichter zu implementierenden, auf empirischen Beziehungen beruhende Methode ausgewählt, um so die Dynamik des Emissionsvermögens verschiedener Landoberflächen zu erfassen. Tagsüber sind die reflektierte solare Einstrahlung und die von der Oberfläche bei $\sim 3.8 \mu\text{m}$ emittierte Strahlung annähernd gleich. Das Reflexionsvermögen wird aus der atmosphärenkorrigierten Strahlung an der Oberfläche und einer Kombination von Verhältnissen der Tag/Nacht Strahlung in zwei Kanälen (TISI-Ratios) bestimmt. Um die Unterbestimmtheit des Gleichungssystems zu beseitigen, wurde angenommen, dass das Emissionsvermögen über einen Tag und eine Nacht konstant ist und dass sich die Landoberflächen wie eine Lambert'sche Fläche verhalten. Die TISI-Methode wurde an die Kanäle von NOAA 9-16 AVHRR und MSG-1 SEVIRI angepasst. Für Simulationen der Strahlung an der Oberfläche wurde eine numerische Analyse durchgeführt, die zeigt, dass die erreichbare Genauigkeit für die LST besser als $1.5 \text{ K} - 2 \text{ K}$ und für das Emissionsvermögen

ungefähr 0.005 ist (AVHRR Kanal 5). Dabei sind diese Ergebnisse unabhängig von der Oberflächenart. Die bedeutendste Quelle des Fehlers könnten falsche oder ungenaue Informationen über die Atmosphäre sein, da die atmosphärischen Korrekturen nicht besser als die zur Verfügung stehenden Informationen über die Atmosphäre sein können. Für diese Studie wurde angenommen, dass die verwendeten Informationen über den Zustand der Atmosphäre korrekt sind. Um saisonbedingte Unterschiede zu beobachten, wurde die Methode auf AVHRR-Daten verschiedener Tage eines großen Teils von Mitteleuropa angewandt. Unter Verwendung des TISI-basierten Emissionsvermögens wurde zusätzlich ein einfaches, auf dem „Normalized Difference Vegetation Index“ (NDVI) basierendes Verfahren auf das Studiengebiet angepasst und die Ergebnisse der beiden Verfahren miteinander verglichen.

Contents

1	Introduction	1
2	Theoretical background and radiative transfer	5
2.1	Spectral measurements by sensors and response functions	6
2.2	Useful part of the electromagnetic spectrum for surface temperature estimation	7
2.3	Radiance measurements by top-of-the-atmosphere sensors	10
2.4	Atmospheric corrections to obtain surface radiances	11
3	Temperature estimation with known emissivity	15
3.1	Surface temperature estimation using single-channel method.....	15
3.2	Split-window techniques (SWT).....	16
3.3	Multi-angle method.....	17
4	Basis and methods of emissivity estimation	18
4.1	Channel emissivity for SEVIRI and AVHRR.....	18
4.2	Methods of emissivity estimation from passive IR and visible data	21
5	Thermal infrared spectral indices (TISI) method.....	22
5.1	Obtaining directional emissivity from day-night data in 2 channels	23
5.2	Optimizing the two-channel TISI for AVHRR and SEVIRI	29
5.3	Method validation using simulated surface radiances	29
5.4	Error reduction and performance enhancement	31
6	Description of the present work and data.....	33
6.1	Study area.....	33
6.2	Data description	35
6.3	Spatial interpolation of atmospheric information	40
6.4	Cloud detection and screening	40
6.5	Software and programs used	41
6.6	Application to the area of interest	42
7	Comparison between spectral and vegetation method	61
7.1	A vegetation index based method for emissivity estimation in 8-13 μm window.....	61
8	Conclusions and outlook.....	69
	References	72
	Notations	78
	Abbreviations.....	79
	List of figures	81
	List of tables.....	84

1 Introduction

Anybody who has been seriously engaged in scientific work of any kind realizes that over the entrance to the gates of the temple of science are written the words: 'Ye must have faith.' It is a quality which the scientist cannot dispense with.

Max Karl Ernst Ludwig Planck (1858 - 1947)
In *Where Is Science Going?* (1932)

Land surface temperature (LST) is an important variable required for a wide variety of applications, *e.g.* climatological, hydrological, agricultural, biogeochemical, and change detection studies. It is maintained by the incoming solar and longwave irradiation, the outgoing terrestrial infrared radiation, the sensible and latent heat flux, and the ground heat flux. Therefore, LST is a good indicator of the energy balance at the Earth's surface. This radiative balance depends on the infrared transmission properties of water vapor, clouds, other trace constituents, *e.g.* greenhouse gases like carbon dioxide (CO_2) *etc.* The concentrations of some of these gases are increasing, *e.g.* CO_2 due to the burning of fossil fuels, which constitute to the change of climate. The average global surface air temperature has risen by $0.6^\circ C$ over the last century and $0.2^\circ C$ to $0.3^\circ C$ over the last 40 years (Jones, 1994) which can be attributed, at least partially, to anthropogenic causes. Another rise by $1.6^\circ C$ to $3.1^\circ C$ is anticipated by 2100, unless intervened by natural processes (Bertrand, van Ypersele, and Berger, 2002). Continuous estimates of LST on a global scale are indispensable for characterizing such climatic changes.

The scientific goals involve not only observation but also determination of the cause and effects of these phenomena, *e.g.* climatic changes indicated above. Hence, operational and long-term LST determination is gaining increasing scientific interest. For large areas and at the spatial-scale of many global circulation models, LST can only be derived from satellite sensors that provide a synoptic bird's-eye view of Earth's surface. Furthermore, measuring LST with high temporal resolution and accessing the rather unfeasible areas is only possible using space-borne and air-borne instruments. The only feasible remote measurements are those which are directly related to the thermal properties of the Earth's surface or atmosphere, *e.g.* measurements of emitted, reflected, scattered, or transmitted electromagnetic radiation. Passive instruments (*e.g.* radiometers) sense the emission from the target and, within suitable wavelength ranges, can be used to deduce the temperature from measured radiances. The concept of remote temperature measurements using 'satellite thermometers' can be dated back at the least to the late 1950s (King, 1956; Kaplan, 1959) and remote LST measurements to the early 1960s with the launch of Television and Infrared Observation Satellite (TIROS)-II (Wark, Yamamoto, and Lienesch, 1962). However, a complete conceptual as well as computational LST deduction scheme can be traced back to the early 1980s (Price, 1983; Price, 1984).

Over the decades, the techniques for measuring surface temperature from space radiometry have improved in terms of method, instrumentation, as well as computation. The current state-of-the-art allows quantification of the atmospheric and surface effects fairly well. However, the approach has achieved a fast and routine-performance only for sea surface temperature (SST) estimation. It was shown that if radiometric measurements of the sea surface are made at different wavelengths or pathlengths, it is possible to relate the two top-of-the-atmosphere (TOA) measurements to the surface temperature: this forms the basis of SST estimation (Prabhakara, Dalu, and Kunde, 1974; McMillin, 1975; Deschamps and Phulpin, 1980). The operational SST-techniques were initially based on a linear algorithm (McClain, Pichel, and Walton, 1985) and were improved using a non-linear technique (Walton, 1988). The SSTs are currently measured operationally using data from the Advanced Very High Resolution Radiometer (AVHRR) onboard the National Oceanic and Atmospheric Administration (NOAA) series of satellites, the Along Track Scanning Radiometer (ATSR) onboard the European Remote

Sensing Satellites (ERS), and recently from the Moderate-resolution Imaging Spectroradiometer (MODIS) onboard the Terra satellite. At present, the attainable SST retrieval accuracy is about $\pm 0.26^\circ\text{C}$ from MODIS data made available by a fully operational scheme (<http://modis-ocean.gsfc.nasa.gov/>).

The success in SST estimation made researchers anticipate similar success for LST. In contrast, it was identified after initial efforts that LST estimation is much more complicated. Apart from the attenuation in the transmitted radiance caused by the atmosphere, the problem is also complicated by the highly variable land surface emissivity (LSE). For the sea surface, which is comparatively homogeneous, a constant emissivity can be assumed or a few *in situ* buoy measurements suffice to obtain a realistic emissivity. But in case of land surface, the emissivity dynamics has a wider range and can vary over short distances. Moreover, a proper LST validation is also difficult because the derived LST is representative for the whole pixel, while point temperature measurements can vary over short distances. Hence, a field validation is possible only for homogeneous areas such as dense vegetation, desert *etc.* and, for other areas, validation is made using simulated data or accuracies are inferred from results of field validation over homogeneous areas.

LST estimation has not yet reached the generality and accuracy desired by the scientific community, but considerable improvements have been made over the past 20 years. The main problem associated with LST determination is three-fold: a) surface-emitted radiance is altered by the atmosphere before reaching TOA sensors, b) radiance measurements by sensors are made in one direction which is not necessarily representative for the upper hemisphere, hence, angular characterization of emissivity is difficult depending on the anisotropy, and c) even after removing the atmospheric effects, a direct separation of temperature from surface radiances is unfeasible because of underdetermination: for a sensor with N spectral channels, there are N measurements but $N + 1$ unknowns (*i.e.* N spectral emissivities and the surface temperature). Therefore, the corresponding system of equations has no unique solution. The combined effect of atmospheric perturbations and varying emissivity increases the difficulty. For resolving this ill-posed problem, additional assumptions are necessary to constrain the extra degree-of-freedom, which has led to different temperature-emissivity separation methods. A few reviews explain the various methods focussing on either emissivity estimation (Hook, Gabell, Green, and Kealy, 1992; Li, Becker, Stoll, and Wan, 1999), or LST determination (Prata, Caselles, Coll, Sobrino, and Ottlé, 1995), or LST and ground-based emissivity (Qin and Karnieli, 1999). A recent comprehensive review of both LST and LSE estimation techniques from passive sensor data is given by Dash, Göttsche, Olesen, and Fischer (2002a).

The main approaches to estimate LST are a) to first separate the effect of the intervening atmosphere and then decouple LST and LSE, and b) to simultaneously remove atmospheric and emissivity effects. Hence, the prevalent methods of LST estimation require *a priori* surface emissivity information. There are 3 distinct LST estimation methods:

- Single-channel method: in this method the TOA radiances are directly compared with radiative transfer calculations for known LSEs, and the LSTs are derived. The method is accurate but needs exact atmospheric information (Price, 1983; Susskind, Rosenfield, Reuter, and Chahine, 1984).
- Split-Window Technique (SWT)/ Multi-channel method: this is based on differential absorption in two spectral channels within 10-12 μm atmospheric window and LST is related to these two measurements (McMillin, 1975). When adjacent channels within one atmospheric window are used, the technique is called SWT and when channels in different atmospheric windows are used, the technique is referred to as a multiple-window technique. Due to operational simplicity SWT is the most popular, however, its coefficients are strictly valid only for the dataset used to derive them and do not always reflect the real situation.

- Multi-angle method: this method is similar to SWT, but the differential absorption is due to different atmospheric slant path-lengths when the same target is observed under different viewing angles in the same spectral range.
- If LSE is known, LST can also be separated from surface radiances (radiances at surface level after atmospheric correction of TOA radiances).

Due to the underdetermination problem, estimating LSE is also a challenging task. However, as LSE is less variable, in space and time than LST, it is reasonable to estimate LSE first and then calculate LST. The earlier methods to estimate LSE either initially assume a constant emissivity, *e.g.* the normalized-emissivity method (Gillespie, 1985), or temperature, *e.g.* the spectral-ratio method (Watson, 1992) and then recalculate the unknown variables. Some methods neglect the surface-reflection term, *e.g.* the alpha-residual method (Kealy and Gabell, 1990; Kealy and Hook, 1993), or require *a priori* surface-information, *e.g.* classification-based emissivity (Snyder, Wan, Zhang, Feng, 1998a; Snyder and Wan, 1998b). The temperature-emissivity separation (TES) method (Gillespie, Rokugawa, Matsunaga, Cothorn, Hook, and Kahle, 1998) hybridizes several methods and uses an empirical relationship to predict the minimum emissivity from the spectral contrast of the ratioed values, which allow to recover the emissivity spectrum. However, TES requires at least 4 to 5 infrared (IR) channels within 10-12 μm and is aimed at the Advanced Spaceborne Thermal Emission and Reflection Radiometer (ASTER); it cannot be used for many existing sensors, *e.g.* AVHRR. Another approach is to link the normalized difference vegetation index (NDVI) to LSE (van de Griend and Owe, 1993), which has been subsequently improved by Valor and Caselles (1996). The NDVI-based methods are suitable for operational purposes but are effective only for vegetated areas, *e.g.* crop growth monitoring. However, NDVI methods cannot cover the dynamic variation of LSE especially due to changes in moisture. Another practical way of estimating LSE is to form spectral indices which are almost independent of the other unknown variable (*i.e.* LST), and to subsequently relate these indices to absolute emissivities. The temperature independent thermal infrared spectral indices (TISI) method (Becker and Li, 1990a), which is a physical method, is an example of such an approach where no empirical relationship is used. The method is robust, applicable to any number of channels except one, and can be tuned to most of the existing and planned multi-spectral sensors. The goal of this work is to choose and establish the most appropriate LSE estimation algorithm in an operational set-up and subsequently to derive LST. In order to make the algorithm suitable for areas on a continental scale (*e.g.* central Europe), the method should have a physical basis independent of empirical relations and surface types. The work is aimed at developing the capacity to process and derive LSE and LST from long-time series of AVHRR data (1996-2002) and to also process data from Spinning Enhanced Visible and Infrared Imager (SEVIRI) onboard Meteosat Second Generation (MSG). At the Meteorological Satellite Applications (MSA) group (Institute of Meteorology and Climate Research, Forschungszentrum Karlsruhe), long-term AVHRR data are obtained from the Institute of Meteorology, FU Berlin, and archived. The MSG SEVIRI data will be received with a High Rate User Station (HRUS with 1028 Kbit/s) already installed at MSA. Hence, the chosen LSE scheme is tuned to AVHRR (NOAA12 - 16) and MSG-1 SEVIRI.

Chapter 2 briefly describes the theoretical background, gives definitions of the variables (LST, LSE, and other radiation-related terms), discusses the suitable part of the electromagnetic spectrum for LST estimation, and explains the atmospheric effects and the radiative transfer equation. Spectral measurements made by actual sensors are described and, the atmospheric correction procedure for individual channels is explained.

Chapter 3 comprehensively describes various approaches for LST retrieval. The single-channel method, SWTs, and the multi-angle method are explained, all of which require surface emissivity as an input. Furthermore, interpolation of atmospheric variables (*e.g.* upwelling and downwelling radiances) derived from atmospheric information, *e.g.* from radiosondes, numerical weather prediction (NWP) models *etc.*, to pixel spatial-scale is addressed.

Chapter 4 explains the theoretical basis of spectral emissivity estimation from passive radiometry. The currently existing methods of emissivity estimation from satellite sensor data are also briefly described and their characteristics and range of application are discussed. The emission behavior of common natural surface types is explained and importance of sensor specific spectral emissivities is emphasized. Using the ASTER spectral library, AVHRR (NOAA 12-16) and SEVIRI (MSG-1) specific emissivity values are derived for various surfaces, which aid the production of synthetic radiances for validation purposes.

Chapter 5 describes the TISI method and forms the theoretical and scientific core of this work. In its basic form, the TISI method only allows the derivation of emissivity ratios. Assuming invariableness of spectral emissivity ratios between day and night, emissivity in 3-4 μm channel can be retrieved via reflectivity of the solar irradiance. This forms the basis of emissivity estimation. Additionally, the chapter deals with the derivation of emissivity in 10-12 μm channels using TISI for emissivity (TISIE) ratios, and LST using surface radiance and determined emissivity. The method has been tuned to NOAA AVHRR and MSG SEVIRI and is validated using simulated radiances.

Chapter 6 presents the results obtained for real data. Data from various sensors and auxiliary information used in the study are explained, *e.g.* AVHRR and SEVIRI IR-data, European Centre for Medium-Range Weather Forecasts (ECMWF) atmospheric reanalyses, the United States Geological Survey (USGS) GTOPO30 digital elevation model (DEM), University of Maryland (UMD) 1 km Global Data Set for surface type, and the World coastline vector database. An overview about the approach for the removal of cloudy pixels is given and some aspects concerning the computational demands are discussed. A comparative study is made between LST retrieved with the TISI approach and with an assumed fixed emissivity value.

Chapter 7 compares TISIE-based and vegetation-based emissivities. In addition, a qualitative comparison is made between TISIE-emissivities and UMD land surface cover types for an area of interest.

Chapter 8 summarizes the present work and gives some conclusions and outlooks. The advantages, disadvantages, and limitations of chosen approach are discussed and some ideas for future improvements are outlined.

2 Theoretical background and radiative transfer

The physicist may be satisfied when he has the mathematical scheme and knows how to use it for the interpretation of the experiments. But he has to speak about his results also to non-physicists who will not be satisfied unless some explanation is given in plain language. Even for the physicist the description in plain language will be the criterion of the degree of understanding that has been reached.

Werner Karl Heisenberg (1901 - 1976)
In Physics and Philosophy (1958)

The land surface is laterally inhomogeneous and is composed of various materials with different geometries which together complicate surface temperature estimation (Qin and Karnieli, 1999). Hence, LST (land surface temperature) on the scale of a grid cannot be measured by point measurements. Additionally, the spatial resolution of satellite observations increases the inhomogeneity; only for homogeneous surfaces at thermal equilibrium temperature can be defined unambiguously. From a remote sensing point-of-view LST is a representative skin-temperature for each pixel. LST measured with radiometry is the “surface radiometric temperature” corresponding to the field-of-view (FOV) of a radiometer (Prata, Caselles, Coll, Sobrino, and Ottlé, 1995). Norman and Becker (1995) defined LST more precisely as “ensemble directional radiometric surface temperature”, where “ensemble” denotes total contribution of an inhomogeneous pixel. LST depends on within-pixel temperature and emissivity distribution, and is a directional quantity (Becker and Li, 1995).

In case of thermodynamic point-measurements (using a thermometer), the temperature is measured at the surface-atmosphere-thermometer interface. Thermodynamic measurements are based on “zeroth law of thermodynamics”, *i.e.* two systems in equilibrium with a third system (*e.g.* a thermometer) are also in equilibrium with each other. Here, the contact-point surface is well defined, *i.e.* the surface should be isothermal and homogeneous (the sub-systems have the same thermodynamic temperature). In contrast, radiometric LST is representative for an area and is not limited to homogeneous isothermal surfaces. Only for a homogeneous isothermal surface radiometric and thermodynamic temperatures are equivalent. However, even for a small-scale ensemble of black bodies at different temperatures there is no equivalent black body temperature yielding the same distribution of spectral radiances (Norman and Becker, 1995). The exact definition of surface and LST also depends on the acquisition device, *e.g.* its spatial resolution, and should match the scale of the target model (Becker and Li, 1995).

Land surface emissivity (LSE) is an intrinsic property of a matter characterizing its emission-behavior and is a spectral quantity. Spectral emissivity is the ratio of the spectral radiance actually emitted by an object at some temperature and the radiance emitted by a black body at the same temperature. Like LST, LSE also is a property of a pixel. It depends on the emissivity distribution within the pixel, the spectral range of measurement, and view angle. Only so-called black bodies have an emissivity of 1; all natural bodies are non-black bodies ($0 < \text{emissivity} < 1$). Electromagnetic radiation transports energy that is quantifiable in terms of spectral radiance ($\text{Wm}^{-2}\mu\text{m}^{-1}\text{sr}^{-1}$), defined as the energy per unit time per unit wavelength per unit solid angle crossing an unit area perpendicular to the viewing direction of the sensor. For measurements over large emitting surfaces (*e.g.* Earth’s surface), with constant FOV and sensor cross section, radiance is independent of path length between surface and sensor (neglecting atmospheric attenuation). Spectral radiance $R(\lambda, T)$ emitted at wavelength λ (μm) from a non-black body at temperature T (K) is given by spectral emissivity $\varepsilon(\lambda)$ times Planck's radiation function $B(\lambda, T)$:

$$R(\lambda, T) = \varepsilon(\lambda)B(\lambda, T) = \varepsilon(\lambda) \frac{C_1 \lambda^{-5}}{\pi \left[\exp\left(\frac{C_2}{\lambda T}\right) - 1 \right]} \quad (1)$$

where C_1 and C_2 are constants ($C_1 = 2\pi hc^2 = 3.7418 \cdot 10^{-16} \text{ Wm}^2$; $C_2 = hc/k = 1.4388 \cdot 10^{-2} \text{ mK}$), h is Planck's constant ($6.626076 \cdot 10^{-34} \text{ Js}$), c is velocity of light ($2.99792458 \cdot 10^8 \text{ ms}^{-1}$), k is Boltzmann's constant ($1.380658 \cdot 10^{-23} \text{ JK}^{-1}$), and spectral radiances are in $\text{Wm}^{-2}\mu\text{m}^{-1}\text{sr}^{-1}$. If there is no influence of the atmosphere and the surface is assumed to be Lambertian, T can be derived by inverting equation (1):

$$T = \frac{C_2}{\lambda \ln \left[\frac{\varepsilon(\lambda)C_1}{\pi \lambda^5 R} + 1 \right]} \quad (2)$$

2.1 Spectral measurements by sensors and response functions

Real sensors measure neither at a particular wavelength nor over the whole electromagnetic spectrum but over a finite range. Channel-radiances (radiant energy per unit wavenumber) measured by sensors with given bandwidths (e.g. AVHRR) for a black body, are given by Planck's function for channel radiance B_k (NOAA-Technical Report NESDIS 71, 1993):

$$B_k(T) = \frac{\int_{\nu_1}^{\nu_2} f_k \frac{c_1 \nu^{-3}}{\exp\left(\frac{c_2 \nu}{T}\right) - 1} \partial \nu}{\int_{\nu_1}^{\nu_2} f_k \partial \nu} \quad (3)$$

where $B_k(T)$ is channel-radiance ($\text{mWm}^{-2}\text{sr}^{-1}\text{cm}$) measured in channel k , ν is wavenumber in cm^{-1} , c_1 ($1.191066 \cdot 10^{-5} \text{ mWm}^{-2}\text{sr}^{-1}\text{cm}^4$) and c_2 (1.438833 cmK) are constants, and f_k is the normalized channel response function of the sensor. For a non-black body equation (3) is multiplied with channel emissivity ε_k .

2.1.1 Normalized channel response function of the sensors

Channel response functions characterize the response of a sensor to available radiance in a particular wavelength range, at small discrete steps. Usually the response functions are normalized to 1, *i.e.* the highest possible response is assumed as unity, and for real calculations Planck's function is convolved with the response function [equation (3)]. Figure 1 and Figure 2 show the similar IR channels of NOAA-14 AVHRR and MSG-1 SEVIRI.

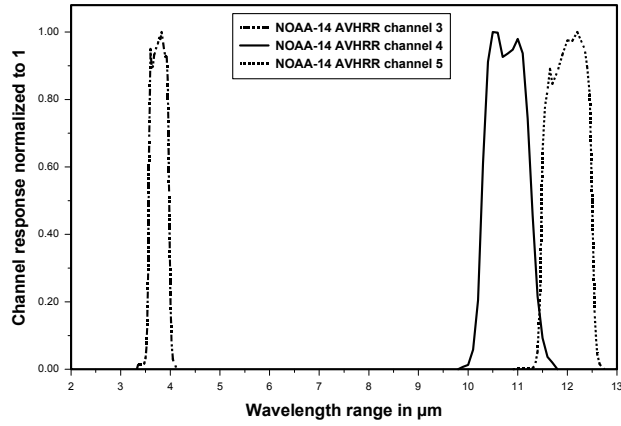


Figure 1: Normalized response functions of NOAA-14 AVHRR channels 3, 4, and 5.

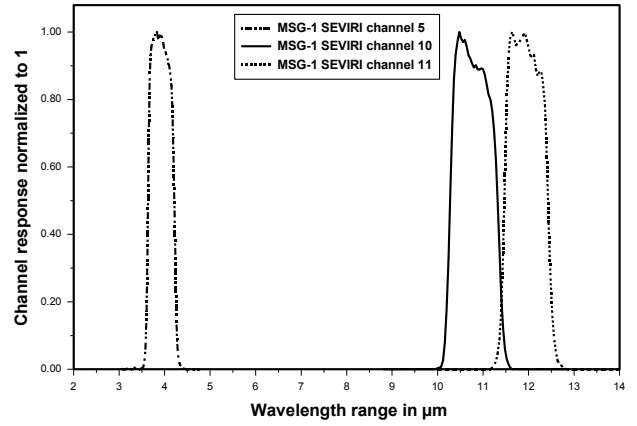


Figure 2: Normalized response functions of MSG-1 SEVIRI channels 5, 10, and 11.

SEVIRI channels (5, 10, and 11) were built upon the heritage and the experience gained from NOAA AVHRR channels (3, 4, and 5). A list of response functions can be obtained from <http://isccp.giss.nasa.gov/docs/response.html> and for SEVIRI from <http://www.eumetsat.de>. A detailed explanation for practical use is available at <http://imk-msa.fzk.de>.

2.2 Useful part of the electromagnetic spectrum for surface temperature estimation

Planck's law of radiation implies that emitted radiance increases with T ; the increase in radiation is a function of both T and λ and for every given temperature the maximum amount of radiation is emitted at a particular wavelength λ_m . Wien's displacement law states that the peak of Planck's function curve shifts to shorter λ with an increase in T and the product of temperature (T) and the corresponding λ_m is constant:

$$T\lambda_m = 2897.9 \text{ K}\mu\text{m} \quad (4)$$

Sun's surface temperature is about 6000 K; a part of the solar radiation reaches Earth's surface and is partly reflected, and partly absorbed at shorter wavelengths and re-emitted as terrestrial infrared (TIR) radiation after heating up the surface. Both reflection and emission form the basis of passive remote sensing. The reflection is used for acquiring optical data, and infrared data is acquired using the emitted part. The fraction of the solar irradiance from S_{Sun} that reaches Earth's surface depends on the opening angle α at the Sun's disc ($\alpha = 0.267^\circ$), part of which is homogeneously reflected over the halfspace S_{half} ($S_{\text{half}} = 2\pi\text{-sr}$). Figure 3 shows the reflection of solar-irradiance from Earth's surface and ambient terrestrial emission.

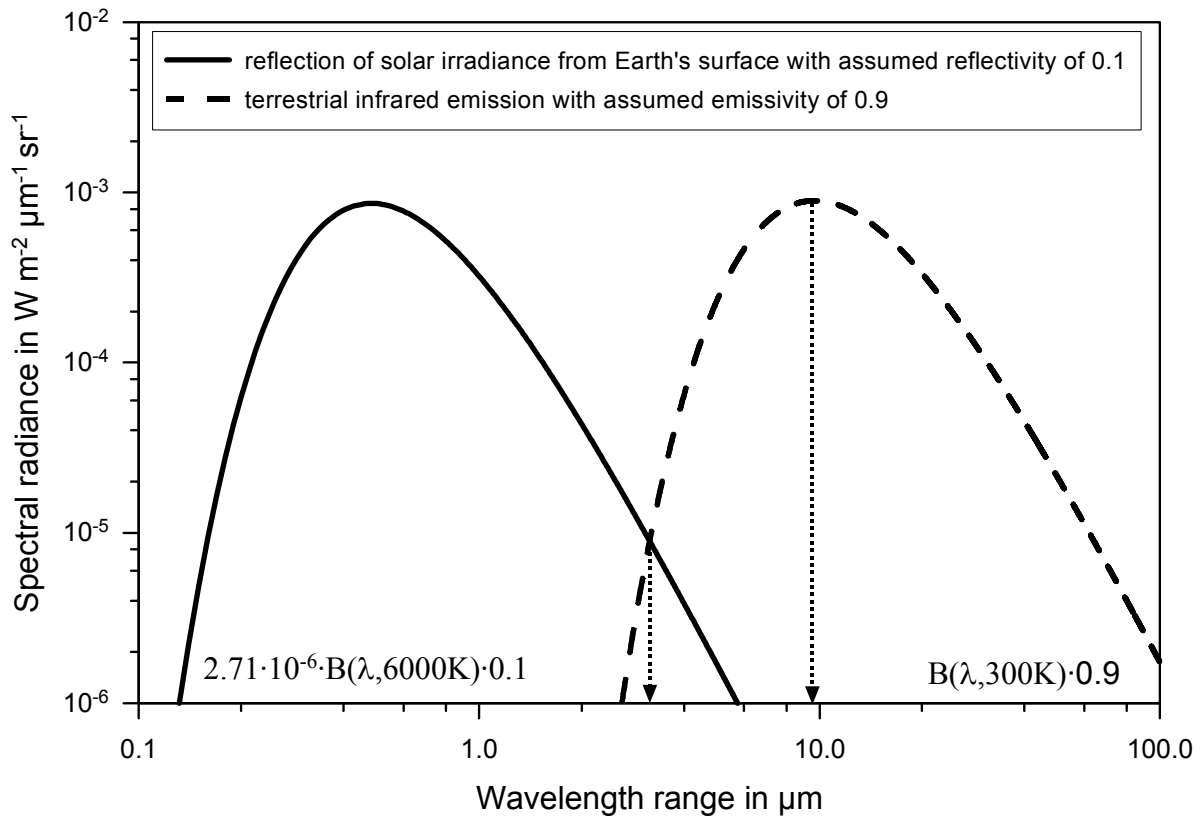


Figure 3: Reflection of solar irradiance from Earth's surface with assumed reflectivity of 0.1 (solid line), and infrared terrestrial emission with assumed emissivity of 0.9 (dashed line). The terrestrial emission is maximum at about $9.7\mu\text{m}$, and reflection of solar irradiance and terrestrial emission are of same order of magnitude at about $3.8\mu\text{m}$.

The amount of solar irradiance reaching Earth's surface (only from the sky geometry; the atmospheric effect is not considered here) is determined by $S_{\text{Sun}}/S_{\text{half}}$. Figure 4 shows the geometry used to derive the fraction of solar irradiance reaching Earth's surface. S_{Sun} denotes the

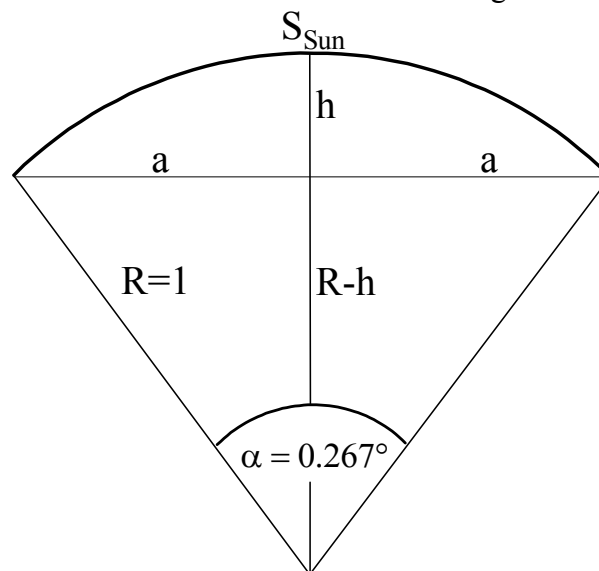


Figure 4: Geometry for deriving the fraction of Sun's irradiance that reaches Earth's surface.

segment of the sky covered by the Sun on a unit sphere centered on Earth's surface. S_{Sun} is determined by the opening angle $\alpha = 0.267^\circ$ (exaggerated in the figure). Using the relation

$S_{\text{Sun}} = \pi \cdot (h^2 + a^2)$, $a = \sin(\alpha/2)$, and $h = 1 - \cos(\alpha/2)$, yields $(S_{\text{Sun}}/S_{\text{half}}) = 1.7 \cdot 10^{-5} / 2\pi = 2.71 \cdot 10^{-6}$ which is the factor multiplied to total solar irradiance for deriving the fraction reaching the Earth.

For Earth with an ambient temperature of ~ 300 K, the peak of the spectral radiance lies at about $9.7 \mu\text{m}$, *i.e.* sensors receive maximum input at this wavelength. At around $3.78 \mu\text{m}$ in the mid-infrared (MIR), the reflection of the solar irradiance and terrestrial emission are of the same order of magnitude. At daytime there is both emission and reflection but at night there is only emission, hence, studies involving reflection of incident solar energy can be made using day and night data from sensors working around $3.8 \mu\text{m}$, *e.g.* AVHRR channel-3 (Dash, Göttsche, Olesen, and Fischer, 2002a) and SEVIRI channel-5 (Dash, Göttsche, and Olesen, 2002b). Additionally, the atmosphere is relatively transparent in the so-called atmospheric windows at $3\text{--}4 \mu\text{m}$ ($W1$) and $8\text{--}13 \mu\text{m}$ ($W2$), where atmospheric absorption is at a minimum and signals are least attenuated. For measurements in these windows, the TOA (top-of-the-atmosphere) radiance is dominated by surface-leaving radiance. The $8\text{--}13 \mu\text{m}$ range also has importance for geological applications, since it covers the important “reststrahlen” bands, where emissivity decreases due to resonance vibrations associated with silicon-oxygen bonds in silica tetrahedra. As the silica content in minerals increases, emissivity decreases and shifts as wavelengths become longer (Hunt, 1980). However, it is worth mentioning that $W2$ is split by the O_3 absorption band at $9.6 \mu\text{m}$; usually the $10\text{--}12 \mu\text{m}$ range is used for LST determination. Apart from the signal strength (S/N ratio), the sensitivity of the measured quantity (radiance) to changes of the target quantity, *i.e.* temperature, is critical. The sensitivity to variations in T is described by the first derivative of $B(\lambda, T)$ with respect to T :

$$\frac{\partial B}{\partial T} = \frac{C_1 C_2 \lambda^{-6} e^{-\frac{C_2}{\lambda T}}}{T^2 \left(e^{\frac{C_2}{\lambda T}} - 1 \right)^2} \quad (5)$$

where the variables and constants are the same as in equation (1). Figure 5 shows $B(\lambda, T)$ and $\partial B/\partial T$ in dependence of λ for a blackbody at 300 K. The two maximums are separated by $\sim 1.7 \mu\text{m}$: the peak of $\partial B/\partial T$ is close enough to the peak of the emitted spectral radiance. Hence, this range not only receives maximum energy but also is sensitive to T changes.

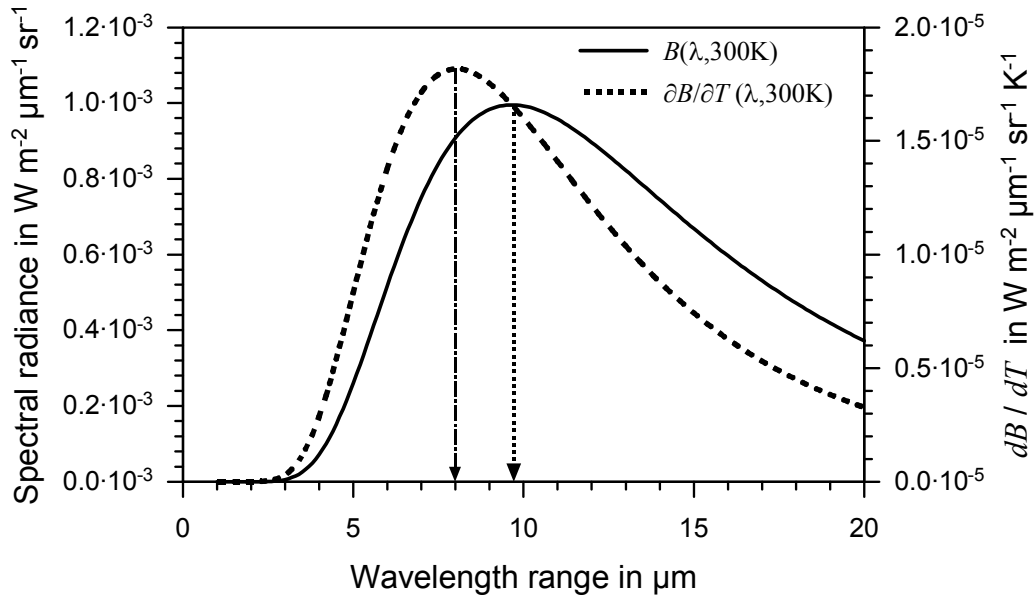


Figure 5: Comparison of $B(\lambda, T)$ versus $\partial B/\partial T$ dependant on λ for a blackbody at 300 K; the peaks are at $9.7 \mu\text{m}$ and $8 \mu\text{m}$ respectively.

In the light of the discussions above, it is evident that IR sensors for LST determination usually should operate around 3.5 μm and 11 μm , *e.g.* AVHRR channel 3 (3.55-3.93 μm), channel 4 (11.5-12.5 μm), and channel 5 (10.3-11.3 μm).

2.3 Radiance measurements by top-of-the-atmosphere sensors

Satellite sensors measure TOA radiances for which the corresponding brightness temperatures (BT) are obtained employing equation (2). In the IR-range, BT is also known as equivalent blackbody temperature. The BT obtained from TOA radiances is TOA BT (T_B^{TOA}) and the BT from surface radiances (which contains effect of emissivity and reflected downwelling radiances) is surface BT (T_B^{sfc}). T_B^{TOA} is generally lower than LST and T_B^{sfc} except for an atmosphere that is warmer than the surface (atmospheric inversion). In the 10-12 μm region, the differences between LSTs and BTs range generally from 1-5 K depending on the atmospheric conditions. The main effects to be removed for determining LST from space are: atmospheric attenuation, view angle effects, and emissivity effects. Atmospheric effects include absorption, upward atmospheric emission, and the downward atmospheric irradiance reflected from the surface (Franca and Cracknell, 1994). In the 8-13 μm IR-window, water vapor is mainly responsible for atmospheric effects; aerosol absorption and scattering are negligible (Prata, Caselles, Coll, Sobrino, and Otlé, 1995), except under severe conditions, *e.g.* dusty atmosphere. Other gases, *e.g.* O_3 and CO_2 also influence atmospheric transmission, but CO_2 is evenly distributed in the atmosphere and tropospheric O_3 is only of local importance. Moreover, these gases vary slowly. Hence, water vapor, which is unevenly distributed and varies in short time, is the most relevant gas. Therefore, exact information about the atmosphere is required for atmospheric corrections, particularly about the temperature and water vapor profiles. Radiosondes provide such information which, at the probe-location, is more accurate than any other method, but the soundings have to be synchronous and co-located with the satellite measurements and the horizontal distribution of the soundings is inhomogeneous. Hence, vertical sounders, *e.g.* TIROS Operational Vertical Sounder (TOVS) onboard NOAA polar-orbiters, are preferred for large-scale studies (Reutter, Olesen, and Fischer, 1994; Lakshmi and Susskind, 2000). Satellite sensors observe the land surface at different viewing geometries; the measurements must also be compensated for zenith angles (Kimes, Idso, Pinter, Reginato, and Jackson, 1980; Kimes and Kirchner, 1983; Ignatov and Dergileva 1994) to make LST algorithms independent of observation geometry. As the emissivity of land surfaces varies dynamically (Nerry, Labed, and Stoll, 1988; Salisbury and D' Aria, 1992), its effect must also be compensated for.

2.3.1 Radiative transfer equation in 8-13 μm and 3-4 μm atmospheric windows

The TOA channel radiances in the two atmospheric windows, *i.e.* $W2$ and in $W1$ (only for nighttime), are given by the radiative transfer equation (RTE):

$$L_k^{TOA} = \varepsilon_k \tau_k(\theta) B_k(T_s) + L_k^\uparrow(\theta) + [1 - \varepsilon_k] \tau_k(\theta) L_k^\downarrow \quad (6)$$

where $k = i, j, r$; i, j are channels in $W2$, r is channel in $W1$ (for AVHRR $i, j = 4, 5$, $r = 3$), L_k^{TOA} is TOA channel radiance, $B_k(T_s)$ is Planck's function for channel radiance, T_s is surface temperature, $L_k^\uparrow(\theta)$ is atmospheric upwelling channel radiance (path radiance), θ is satellite zenith angle, L_k^\downarrow is downwelling atmospheric channel radiance (hemispherical irradiance divided by π), τ_k is atmospheric transmissivity, and ε_k is channel surface emissivity.

The first expression in equation (6) denotes the surface-emission attenuated along the upward path, the second term represents the path-radiance (atmospheric contribution in upward direction), and the third term constitutes the atmospheric irradiance reflected from the surface and attenuated along the upward path. For daytime measurements in $W1$, also, the reflection and scattering of solar irradiance and the diffused downward solar irradiance have to be considered:

$$L_k^{TOA} = \varepsilon_r \tau_r(\theta) B_r(T_s) + L_r^\uparrow(\theta) + [1 - \varepsilon_r] \tau_r(\theta) L_r^\downarrow + \tau_r(\theta_{Sun}) E_{Sun}^{TOA} \cos(\theta_{Sun}) \frac{1 - \varepsilon_r}{\pi} F_r(\theta, \theta_{Sun}, \phi) \tau_r(\theta) \\ + \tau_r(\theta, \theta_{Sun}, \phi) E_{Sun}^d(\theta, \theta_{Sun}, \phi) \frac{1 - \varepsilon_r}{\pi} F_r(\theta, \theta_{Sun}, \phi) \tau_r(\theta) + E_{Sun}^s(\theta, \theta_{Sun}, \phi) \quad (7)$$

where E_{Sun}^{TOA} is TOA solar spectral irradiance for channel r , θ_{Sun} is local Sun zenith, $\tau_r(\theta_{Sun})$ is channel transmissivity along the path of sunlight, $F_r(\theta, \theta_{Sun}, \phi)$ is angular form factor of the surface, ϕ is difference between satellite and Sun azimuth angles (see section 2.4), $E_{Sun}^d(\theta, \theta_{Sun}, \phi)$ is diffused downward solar irradiance, and $E_{Sun}^s(\theta, \theta_{Sun}, \phi)$ is scattered path solar radiance.

Calculation of LST requires *a priori* surface emissivity, *i.e.* in order to solve equation (6) for LST, ε_k and τ_k have to be known. Emission and transmission depend on temperature: however, for a temperature range of about 260-320 K the variation of ε_k with T_s is negligible (Becker and Li, 1990a). Atmospheric correction is performed to obtain at-ground radiances [*i.e.*, sum of first and last term divided by τ_k in equation (6), and sum of all the terms except the second term divided by respective τ_k in equation (7)]. If emissivity is known, the contributions of LST and emissivity can be directly separated from surface radiances.

2.4 Atmospheric corrections to obtain surface radiances

In order to retrieve emissivities of land surfaces, surface radiances have to be obtained. Simplifying equations (6) or (7), surface radiances are given by:

$$R_k = \frac{L_k^{sat} - L_k^\uparrow(\theta)}{\tau_k(\theta)} \quad (8)$$

For channels i and j and for channel r (at night-time), R_k in equation (8) contains terrestrial emission and reflected downwelling atmospheric radiance:

$$R_k = \varepsilon_k B_k(T_s) + (1 - \varepsilon_k) L_k^\downarrow \quad (9)$$

For channel r at daytime R_k also contains reflected solar irradiance:

$$R_{r,TOTAL}^D = \varepsilon_r B_r(T_s) + (1 - \varepsilon_r) L_r^\downarrow + \rho_r(\theta, \theta_{Sun}, \phi) E_{Sun} = R_r^D(T_s) + \rho_r(\theta, \theta_{Sun}, \phi) E_{Sun} \quad (10)$$

where D denotes daytime, $\rho_r(\theta, \theta_{Sun}, \phi)$ is bi-directional reflectivity, and E_{Sun} is solar spectral irradiance at ground level in channel r .

Reflectivity is a bi-directional quantity: the position of the Sun gives the incident direction defined by θ_{Sun} (Sun zenith) and ϕ_{Sun} (Sun azimuth), and the observation direction is defined by θ (satellite zenith) and ϕ_{sat} (satellite azimuth). Therefore, $\rho_r(\theta, \theta_{Sun}, \phi)$ is a function of four angles and is properly given as $\rho_r(\theta, \theta_{Sun}, \phi, \phi_{Sun})$. However, in practice radiance is unchanged when a (natural) surface is rotated around the normal and $\rho_r(\theta, \theta_{Sun}, \phi)$ depends on the relative azimuth ϕ ($=\phi_{sat} - \phi_{Sun}$). Variables $L_k^\uparrow(\theta)$ and $\tau_k(\theta)$ are obtained from atmospheric profiles employing a radiative transfer model (RTM), *e.g.* the Moderate Resolution Transmittance (MODTRAN) code (Kneizys *et al.*, 1996). At daytime, $L_r^\uparrow(\theta)$ also contains the path radiance due to scattering of solar irradiance in $W1$ and $R_r^D(T_s)$ in equation (10) also contains the diffused solar irradiance. If

the spatial resolution of available information is less than that of the satellite data, which usually is the case, derived atmospheric variables have to be interpolated to pixel-scale.

2.4.1 Correction of high spectral resolution data without atmospheric information

A few methods exist that aim at atmospheric correction without additional atmospheric information, *e.g.* the autonomous atmospheric compensation (AAC) method (Gu, Gillespie, Kahle, and Palluconi, 2000). The AAC method only requires spatial IR images, with high spectral resolution, to compensate for the atmospheric effect and to obtain surface radiances from at-sensor radiances. It was validated using data of the airborne Spatially Enhanced Broadband Array Spectrograph System (SEBASS). The method is based on the following assumptions: a) over small areas, atmospheric variables are spatially more uniform than surface variables, and b) surface radiance spectra are considerably smoother than atmospheric radiation and absorption. Hence, for two closely placed high spectral resolution channels in and out of an atmospheric absorption band, *e.g.* absorption at 11.73 μm by water vapor, surface radiances for the channels are practically the same, and the difference between the at-sensor radiances is caused by the atmosphere alone. This property is exploited to derive the transmittance ratio and the path radiance difference, from which the atmospheric transmission and the path radiance is inferred using an empirical relationship. However, LST and emissivity have to be subsequently separated from the surface radiance. Initial results are encouraging, but further research is needed to develop this hyperspectral approach.

2.4.2 Analysis of atmospheric effects for various atmospheric models

In order to analyze the atmospheric effect (only path radiance without emissivity), a set of TOA (top-of-the-atmosphere) radiances was simulated using MODTRAN-3.7 and atmospheric information from model data for mid-latitude summer (MLS), mid-latitude winter (MLW), sub-arctic summer (SAS), sub-arctic winter (SAW), US standard 1976 (USS), and one profile from the 1996 TOVS Initial Guess Retrieval (TIGR) tropical (TROP) profiles. A range of temperature was selected (273.16-323.16 K range and 10 K interval) and emissivity was fixed to 0.98. Then, for NOAA-14 AVHRR channels 3, 4, and 5, TOA radiance, path radiance, and transmissivity were calculated. Subsequently, from TOA radiance, path radiance, and transmissivity, surface radiances were calculated and T_B^{sfc} and T_B^{TOA} were obtained from surface radiances and TOA radiances, respectively. In T_B^{sfc} the effect of path radiance is removed but it still contains the effect of emissivity (reflectivity). The difference between T_B^{sfc} and T_B^{TOA} is a measure of the effect of path radiance alone. Figure 6 shows the difference between T_B^{sfc} and T_B^{TOA} plotted against LST, for NOAA-14 AVHRR channels 4, and 5 and MLW and MLS. The other data (numerical values from simulation) are given in appendix-1.

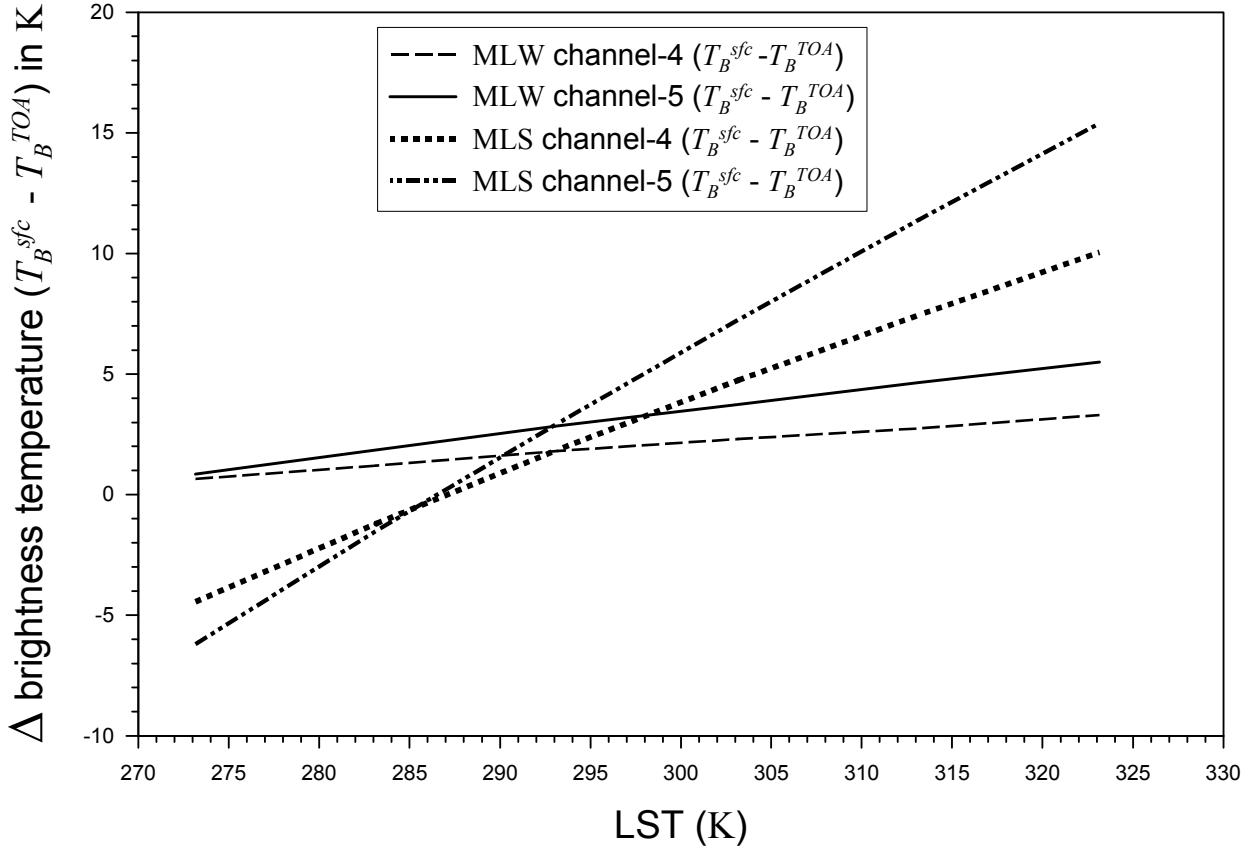


Figure 6: Surface and TOA brightness temperatures differences (path contribution) as a function of LST, for NOAA-14 AVHRR channels 4 and 5, and MLW and MLS.

The atmospheric corrections (effect only of atmospheric path) are approximately linear with respect to LST. The corrections were negative for LST less than (or very close to) lowest air temperature. This is an example of so-called atmospheric inversion. It is also evident from Figure 6 that measurements around 11 μm are less attenuated by water vapor than that around 12 μm , *i.e.* AVHRR channel-4 is less affected than channel-5. However, from absorption spectra, it is known that channel-4 is more affected by CO_2 (some CO_2 absorption lines at 10.4 μm) than channel-5. Nevertheless, as CO_2 varies less than water vapor and is well-known, the corrections are not affected. Hence, it can be concluded that 10-11 μm channels (AVHRR channel-4) are less affected than 11-12 μm (AVHRR channel-5) channels. This is the basis for choosing an appropriate channel in later parts of this work.

Zenith angle and elevation also have a significant effect on TOA radiance as they directly determine the path-length between the source and the target. Hence, it is necessary to accurately account for these variables. For the US standard 1976 model atmosphere and a zenith angle range of 0-60° Figure 7 and Figure 8 show the effect of zenith angle on path-radiance and TOA radiance respectively.

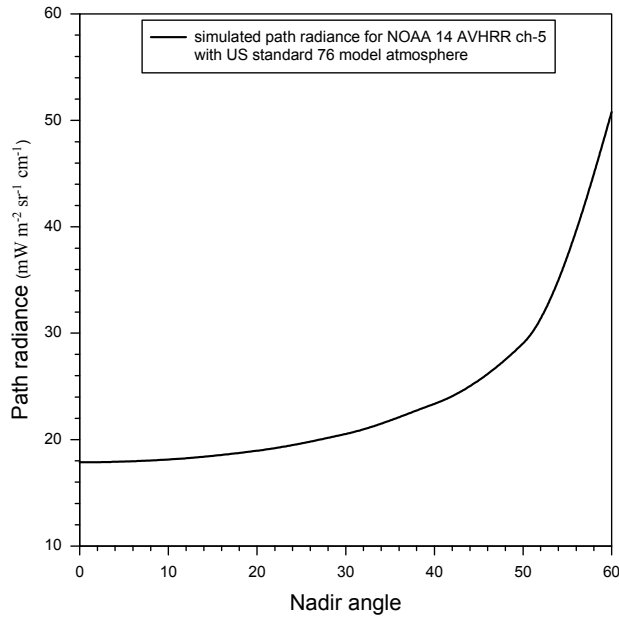


Figure 7: Variation of path-radiance related to zenith angle for NOAA-14 AVHRR channel-5 and US standard 1976 model atmosphere.

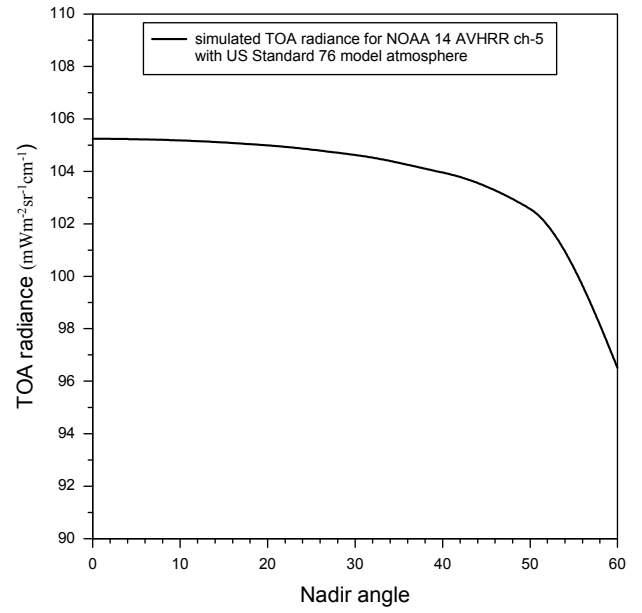


Figure 8: Variation of top-of-the-atmosphere radiance related to NOAA-14 AVHRR channel-5 and US standard 1976 model atmosphere.

Whereas the atmospheric contribution (path-radiance) increases with path-length, the total TOA radiance decreases with increasing path-length. In order to obtain surface radiances, it is necessary to accurately provide the zenith angle and the surface-height in calculation of the variables $L_k^\uparrow(\theta)$ and $\tau_k(\theta)$ in equation (8).

3 Temperature estimation with known emissivity

Have you ever thought...about whatever man builds, that all of man's industrial efforts, all his calculations and computations, all the nights spent over working draughts and blueprints, invariably culminate in the production of a thing whose sole and guiding principle is the ultimate principle of simplicity?...In any thing at all, perfection is finally attained, not when there is no longer anything to add, but when there is no longer anything to take away.

Antoine-Marie-Roger de Saint-Exupery (1900- 1944)
In *Wind, Sand and Stars* (1939)

The three prevalent LST (land surface temperature) estimation methods, with *a priori* emissivity, aim at compensating for atmospheric and angular effects. An overview of various LST estimation techniques is given by Dash, Göttsche, Olesen, and Fischer (2002a; 2001). The corrections are performed either by radiative transfer calculations (RTCs) for one channel (single-channel method), or by exploiting the differential absorption for two different measurements, where the difference is mainly due to the atmosphere. The so-called SWT (split-window technique) makes the two measurements in two different channels in $W2$. If the difference in absorption for two measurements in one channel is due to different viewing angles, and thus different path-lengths, it is called as multi-angle method. Both of these differential-absorption based approaches correlate LST with TOA brightness temperatures through coefficients derived by regression analysis (linear or quadratic). These coefficients compensate for the atmospheric effects (for known emissivities); however, in a strict sense, the coefficients hold only for the dataset used to derive them. Despite this limitation, the SWT is most popular because of its operational simplicity. Single-channel methods are more accurate if sufficient information about the state of the atmosphere is available.

3.1 Surface temperature estimation using single-channel method

As the name depicts, a single-channel method involves atmospheric corrections of measurements in one window-channel (Price, 1983; Susskind, Rosenfield, Reuter, and Chahine, 1984), usually in $W2$. These methods require accurate information about vertical and horizontal distribution of temperature and water vapor in the atmosphere. Such information is obtained from radiosondes, vertical sounding instruments on satellites, *e.g.* TOVS, or from NWP models, *e.g.* European Centre for Medium-range Weather Forecast (ECMWF) Re-analysis (ERA). Using RTMs (radiative transfer models) such as MODTRAN, the method relies on simulation of TOA (top-of-the-atmosphere) measurements, for a given atmosphere, over a range of surface-related variables (temperatures, elevations and emissivities), solar position, and satellite-related variables (scan angles, satellite zenith angles). Afterwards, the atmospheric corrections for each of the profiles are derived from the simulated results and known surface variables. As atmospheric profile data are discrete in space and time, LST and atmospheric corrections are obtained by interpolating these calculations (Schroedter, Olesen, and Fischer, 2003). Because the method is based on the simulation of actual conditions, it is the most accurate. However, it requires exact atmospheric information and corrections will be only as good as these. Prior information about surface emissivity is also required. Only for homogeneous areas a constant emissivity can be assumed with reasonable accuracy, *e.g.* for mid-latitude vegetated areas an assumed emissivity of 0.975 and an error of ± 0.025 introduces an LST error of ± 2 K (Schädlich, Göttsche, and Olesen, 2001).

3.2 Split-window techniques (SWT)

The $W2$ window contains the channels of most operational meteorological satellites and is wide enough to allow observations in several channels. The SWT uses differential absorption between two channels within $W2$ for eliminating the atmospheric influence, and calculates T_s as a combination of two T_B^{TOA} . For the IR spectral region, assuming that radiation comes from the surface and the atmospheric block above, the RTE is given as (McMillin, 1975):

$$L_k^{TOA} = B_k(T_B^{TOA}) = \tau_k B_k(T_s) + B_k(T_a)[1 - \tau_k] \quad (11)$$

where $B_k(T_a) = \frac{1}{1 - \tau_k} \int_0^1 B_k(T) \partial\tau$, and T_a is a mean temperature of the atmosphere.

For the two channels in $W2$ it was assumed that: a) their contribution functions are similar, therefore, T_a is equivalent, and b) the difference in transmittance results due to different absorption by water vapor in the two channels and not due to emissivity differences (Kidder and Vonder Haar, 1995). Writing equation (11) for AVHRR channels 4 and 5, subsequently inserting equation (3) into them, and simplifying further yields the simplest SWT:

$$T_s = T_4 + a(T_4 - T_5) + b \quad (12)$$

where coefficients a and b account for the atmospheric perturbations and *a priori* emissivity is accommodated into one of the coefficients. Despite computational simplicity, this SWT does not always hold, as its coefficients are strictly valid only for the data used to derive them and do not always reflect the real situation. For strongly varying emissivities and water vapor, there can be large errors in derived LSTs. The method is easily validated over oceans where an emissivity can be assumed or measured, *e.g.* from *in situ* radiometer measurements, but this is more complicated over land surfaces. Subsequent studies also have proved that quadratic formulations are more efficient than linear formulations (François and Ottlé 1996; Coll and Caselles, 1997). Using 1761 profiles of the TIGR data, François and Ottlé (1996) performed RTCs with the 4A RTM (Scott and Chédin, 1981) and showed that the assumption of constant T_a in two channels is incorrect. They demonstrated that the classical linear SWT [equation (12)] is invalid on a larger scale and quadratic formulations, which incorporate both emissivity and water vapor, achieve better results. Since it is unfeasible to obtain global *in situ* LST data at satellite sensor spatial resolution to validate the SWTs, the performance of split-window formulations is generally evaluated by intercomparison studies (Prata 1993; Becker and Li 1995; Coll and Caselles, 1997). In this research, LST is derived directly from atmospherically corrected surface radiances and emissivity is estimated using a two-channel TISI method. Hence, the various existing SWTs are not detailed; a comprehensive derivation and the coefficients of various SWTs is given by Dash, Göttsche, Olesen, and Fischer (2002a).

SWTs are derived by simplifying the atmospheric effects calculated using RTMs. The SWT of Price (1984) and Becker and Li (1990b) account only for emissivity variations; the coefficients for removing atmospheric effects are set to (locally valid) fixed values. The coefficients of Sobrino, Coll, and Caselles (1991), and Becker and Li (1995) also depend on the current atmosphere. Considering pixels as a mixture of soil and vegetation, Kerr, Lagouarade, and Imbernon (1992) proposed a method based on vegetation proportion, which they obtained from NDVI (normalized difference vegetation index). The method classifies each pixel as a combination of either bare soil or vegetation and then combines their separate effects to derive LST. The SWT of Coll, Caselles, Sobrino, and Valor (1994) also accounts for the effect of view-angle. Some formulations use quadratic relationships (François and Ottlé 1996; Coll and Caselles, 1997) and account for water vapor and emissivity. In order to generalize the SWT to a global scale, the coefficients must accommodate changes in the atmospheric parameters caused by varying view-angle and water vapor. The generalized SWT (Wan and Dozier, 1996) is an

optimized view-angle dependent SWT, which separates water vapor, lower boundary temperature, and LST into tractable subranges. The coefficients are selected from look-up table (LUT) using the scan angle and atmosphere. Information from atmospheric sounders are used only to determine the subrange for choosing optimum coefficients. Despite the improved generality of SWTs, LSE (land surface emissivity) remains a critical issue and all SWTs require *a priori* pixel-wise emissivity.

3.3 Multi-angle method

The method is based on a similar principle to SWT, but different absorption is due to different atmospheric path-lengths for different observation angles. The measurements can be made from one satellite or simultaneously from two satellites, *e.g.* Meteosat and TIROS-N (Chedin, Scott, and Berroir, 1982). The first sensor in biangular-mode available was the ATSR onboard ERS-1. ATSR measures at near-nadir (0° - 22°) and at forward view (55°). Assuming that angular variation of LSE is negligible for observations $< 60^\circ$, Prata (1993) derived a dual-angle method for ATSR. Later, an improved procedure was proposed by Sobrino, Li, Stoll, and Becker (1996):

$$B_k(T_s) = B_k(T_n) \frac{a_1}{a_2} - B_k(T_f) \frac{a_0}{a_2} - \left[B_k(T_{a_n}) - B_k(T_{a_f}) \right] \frac{a_0 a_1}{a_2} \quad (13)$$

where n and f denote nadir and forward view respectively, a_0 , a_1 , and a_2 are given by:

$$a_0 = 1 - \tau_n \tau_{53} - \varepsilon_n \tau_n (1 - \tau_{53}) \quad (14)$$

$$a_1 = 1 - \tau_f \tau_{53} - \varepsilon_f \tau_f (1 - \tau_{53}) \quad (15)$$

$$a_2 = \varepsilon_n \tau_n (1 - \tau_f \tau_{53}) - \varepsilon_f \tau_f (1 - \tau_n \tau_{53}) \quad (16)$$

The transmission of diffuse radiation is approximated by the transmission of directed radiation for the same mass of absorbing substance at $\theta \approx 53^\circ$ (Kondratyev, 1969); τ_{53} is used to account for and to simplify the contribution due to reflection. LSTs are more easily validated than radiances and are independent of wavelength. Using Taylor expansion for moderate temperature conditions equation (13) was simplified to:

$$T_s = T_{B_n} + (T_{B_n} - T_{B_f}) \frac{a_0}{a_2} - \left[1 + \frac{a_0 - a_1}{a_2} \right] P_n - (T_{a_n} - T_{a_f}) \frac{a_0 a_1}{a_2} \quad (17)$$

where P_n is a parameter with dimension of temperature and is obtained by adjusting to Planck's function (Price, 1984). Sobrino, Li, Stoll, and Becker (1996) showed that the technique estimates SSTs with an error < 0.23 K. They also concluded that the method is superior to SWT if the spectral as well as angular variation of LSE is known. However, apart from assuming that the atmospheric column is spatially uniform, the technique requires that one of the measurements is made for a significantly longer path; otherwise the algorithm becomes unstable (Prata, 1993). Furthermore, knowledge of the angular variation of the surface emissivity and anisotropy of the surface leaving radiation due to structures is also required, which is not easily fulfilled at satellite spatial resolution.

4 Basis and methods of emissivity estimation

I often say that when you can measure what you are speaking about, and express it in numbers, you know something about it; but when you cannot measure it, when you cannot express it in numbers, your knowledge is of a meagre and unsatisfactory kind; it may be the beginning of knowledge, but you have scarcely, in your thoughts, advanced to the stage of Science, whatever the matter may be.

Lord William Thomson Baron Kelvin (1824 - 1907)

Surface emission depends on surface parameters, *i.e.* surface emissivity and temperature. Unlike for oceans emissivity of land surfaces is significantly non-uniform and varies with vegetation, surface moisture, composition, and roughness (Nerry, Labed, and Stoll, 1988; Salisbury and D' Aria, 1992). As emissivity depends on wavelength, it is referred to as spectral emissivity; it also has a view-angle dependency. However, for the sake of simplicity, the angle dependency is not shown in the following expressions, *e.g.* equation (18). For measurements with passive sensors near to the surface, *e.g.* with a radiometer, channel emissivity can be given by simplifying equation (9):

$$\varepsilon_k = \frac{R_k - L_k^\downarrow}{B_k(T_s) - L_k^\downarrow} \quad (18)$$

where the variables are same as in equation (9).

TOA measurements are affected by LSE (land surface emissivity) in three ways: a) it reduces the surface-emitted radiance in comparison to a black body, b) non-black surfaces reflect downwelling radiance, and c) the anisotropy of reflectivity and emissivity can reduce or increase the total surface-radiance (Prata, 1993). Lack of knowledge of LSE introduces an LST (land surface temperature) error (ΔT), which is defined as the difference of LST retrieved at the actual LSE and for $\varepsilon = 1$. For an LSE of 0.98 and 0 km ground height, the error in the LST retrieved with the single-channel method ranges from 0.2 K to 1.2 K for MLS atmosphere and from 0.8 K to 1.4 K for MLW atmosphere. As emissivity decreases LST error increases, *e.g.* for LSE of 0.93 and ground height of 0.5 km, LST error ranges from 0.8-3.4 K for MLS and from 2.8-4.8 K for MLW (Schaedlich, Göttsche, and Olesen, 2001). Becker (1987) showed that for SWTs (split-window techniques), the effect of LSE on LST error is significant and can be approximated as:

$$\Delta T \approx 50 \frac{1 - \varepsilon_{avg}}{\varepsilon_{avg}} - 300 \frac{\Delta \varepsilon}{\varepsilon_{avg}} \quad (19)$$

where $\Delta \varepsilon$ is the difference between the two channel emissivities and (ε_{avg}) is the average of the two emissivities.

4.1 Channel emissivity for SEVIRI and AVHRR

Similar to channel radiance, channel emissivity (ε_k) can be defined by convolving spectral emissivity with the normalized channel response function (ε_k). Ideally, the convolution should also include the temperature dependency via the (B_k). However, in a terrestrial temperature range, LSE is almost independent of LST (Becker and Li, 1990a), *e.g.* AVHRR channel 3 emissivity for coarse sand changes only by 0.004 over the range of 240-320 K (Wan and Dozier, 1996). Therefore, (ε_k) can be derived from:

$$\epsilon_k = \frac{\int_{\lambda=\lambda_1}^{\lambda_2} f_k \epsilon(\lambda) \partial\lambda}{\int_{\lambda=\lambda_1}^{\lambda_2} f_k \partial\lambda} \quad (20)$$

where λ denotes wavelength, $\epsilon(\lambda)$ is spectral emissivity, and f_k is normalized channel response function. Spectral emissivity $\epsilon(\lambda)$ for various surfaces can be obtained by field or laboratory measurements, e.g. the ASTER spectral reflectivity library (<http://speclib.jpl.nasa.gov>). For Earth's surface, the pixels of satellite sensors consist usually of mixed rather than pure substances. However, for method validation and simulation sensor-specific channel emissivities are required as input. Hence, a set of ϵ_k values for a number of surface types was generated using equation (20), the ASTER spectral library, and the (f_k) for MSG SEVIRI channels (5, 10, and 11) and NOAA (12-16) AVHRR channels (3, 4, and 5). Table 1 and Table 2 give SEVIRI and AVHRR channel emissivities, respectively.

Series	Surface type		SEVIRI channel emissivity		
			Channel-5 (3.8 μ m)	Channel-10 (10.8 μ m)	Channel-11 (12.0 μ m)
MSG-1	Vegetation	Coniferous	0.988	0.989	0.991
		Deciduous	0.982	0.974	0.973
		Grass	0.983	0.982	0.989
		Dry grass	0.815	0.911	0.912
	Soils	Black loam	0.912	0.974	0.979
		Brown silty loam	0.846	0.973	0.980
		Dark brown sand	0.820	0.964	0.978
		Yellow loamy sand	0.674	0.959	0.970
	Manmade	Construction concrete	0.878	0.951	0.968
		Slate stone Shingle	0.835	0.891	0.945
		White marble	0.960	0.934	0.940
	Water	Sea water	0.976	0.990	0.987
		Sea foam	0.969	0.990	0.987

Table 1: MSG-1 SEVIRI channels (5, 10, and 11) emissivity for various surfaces at nadir view. The $\epsilon(\lambda)$ are reproduced from the ASTER spectral reflectivity library available courtesy of Jet Propulsion Laboratory, California Institute of Technology, Pasadena, Copyright ©1999. The measurements were made from the vertical and emissivities are derived from respective reflectivity values using Kirchoff's law. The channel emissivities ϵ_k are obtained by convolving $\epsilon(\lambda)$ with channel response functions [equation (20)].

Series	Surface type		AVHRR channel emissivity		
			Ch-3 (3b) (3.8 μ m)	Ch-4 (10.8 μ m)	Ch-5 (11.9 μ m)
NOAA-12	Vegetation	Coniferous	0.988	0.989	0.991
		Deciduous	0.983	0.973	0.973
		Grass	0.983	0.983	0.989
		Dry grass	0.841	0.909	0.913
	Soils	Black loam	0.892	0.974	0.979
		Brown silty loam	0.852	0.973	0.980
		Dark brown sand	0.825	0.965	0.978
		Yellow loamy sand	0.679	0.960	0.970
	Manmade	Construction concrete	0.882	0.953	0.968
		Slate stone Shingle	0.840	0.899	0.946
		White marble	0.959	0.931	0.942
	Water	Sea water	0.975	0.990	0.986
Sea foam		0.967	0.990	0.987	
NOAA-14	Vegetation	Coniferous	0.988	0.989	0.991
		Deciduous	0.983	0.974	0.973
		Grass	0.983	0.982	0.989
		Dry grass	0.843	0.911	0.914
	Soils	Black loam	0.891	0.974	0.979
		Brown silty loam	0.854	0.972	0.980
		Dark brown sand	0.826	0.964	0.978
		Yellow loamy sand	0.681	0.959	0.971
	Manmade	Construction concrete	0.883	0.950	0.968
		Slate stone Shingle	0.841	0.891	0.946
		White marble	0.959	0.934	0.942
	Water	Sea water	0.975	0.990	0.986
Sea foam		0.967	0.990	0.987	
NOAA-15	Vegetation	Coniferous	0.988	0.989	0.991
		Deciduous	0.983	0.973	0.973
		Grass	0.984	0.982	0.988
		Dry grass	0.854	0.910	0.912
	Soils	Black loam	0.884	0.974	0.978
		Brown silty loam	0.860	0.973	0.980
		Dark brown sand	0.832	0.965	0.979
		Yellow loamy sand	0.687	0.960	0.967
	Manmade	Construction concrete	0.881	0.952	0.968
		Slate stone Shingle	0.844	0.895	0.946
		White marble	0.956	0.934	0.940
	Water	Sea water	0.974	0.990	0.987
Sea foam		0.967	0.990	0.987	
NOAA-16	Vegetation	Coniferous	0.988	0.989	0.991
		Deciduous	0.983	0.973	0.973
		Grass	0.984	0.983	0.987
		Dry grass	0.855	0.909	0.913
	Soils	Black loam	0.883	0.974	0.979
		Brown silty loam	0.861	0.974	0.980
		Dark brown sand	0.832	0.966	0.977
		Yellow loamy sand	0.689	0.961	0.970
	Manmade	Construction concrete	0.881	0.953	0.968
		Slate stone Shingle	0.844	0.900	0.946
		White marble	0.956	0.927	0.943
	Water	Sea water	0.974	0.990	0.986
Sea foam		0.967	0.990	0.987	

Table 2: NOAA (12-16) AVHRR channels (3, 4, and 5) emissivity for various surfaces. $\epsilon(\lambda)$ are reproduced from the ASTER spectral reflectivity library available courtesy of Jet Propulsion Laboratory, California Institute of Technology, Pasadena, Copyright ©1999. The channel emissivities ϵ_k are obtained by convolving $\epsilon(\lambda)$ with channel response functions [equation (20)].

4.2 Methods of emissivity estimation from passive IR and visible data

Several methods to estimate channel emissivity from satellite sensor data exist, which are applicable in the MIR and TIR range, the visible range, or which utilize a combination of IR and visible data. Examples of such methods are: reference channel method by Kahle, Madura, and Soha (1980), normalized emissivity method (NEM) of Gillespie (1985), spectral-ratio method (Watson, 1992), alpha residuals (Kealy and Gabell, 1990; Kealy and Hook, 1993), thermal-infrared spectral indices (Becker and Li, 1990a), temperature emissivity separation (TES) using maximum-minimum difference of emissivity (Gillespie, Rokugawa, Hook, Matsunaga, and Kahle, 1996; Gillespie, Rokugawa, Matsunaga, Cothorn, Hook, and Kahle, 1998), using NDVI (van de Griend and Owe, 1993; Valor and Caselles, 1996), or classification-based emissivity method using bi-directional reflection distribution function (BRDF) models (Snyder, Wan, Zhang, and Feng, 1998a; Snyder and Wan, 1998b). The different LSE estimation methods result from the different assumptions made for the regularization of the underdetermined problem. The methods either estimate relative or absolute emissivity. The “relative” methods estimate the spectral shape or ratio of emissivities, while the “absolute” methods estimate absolute directional emissivity and are based on critical assumptions (problem of underdetermination).

Some of the LSE methods either initially assume a constant LSE, *e.g.* NEM, or constant temperature, *e.g.* the spectral-ratio method, and then the unknown variable is calculated and the assumed constant variable is subsequently recalculated. A few methods neglect the surface-reflection term or require *a priori* surface-information. NDVI based methods are useful if the LSE of bare ground and vegetation as well as the vegetation structure and distribution is known. The classification based emissivity method requires information about cover type and the amount of vegetation. Algorithms developed for multispectral data show promising results, *e.g.* the TES method combines the advantages of several methods but it can be applied only if a sufficient number of channels (4-5) are available in the TIR. The TISI is a robust method for estimating relative emissivity. However, assuming that LSE ratios for day and night data do not vary, the method can also be used to calculate absolute directional emissivity. The method is applicable to any number of channels (two or more). As the method is based on physical knowledge, *i.e.* it does not use an empirical relationship, it is capable of capturing the whole emissivity dynamics and it is not limited to vegetated areas. It also does not require surface type information or BRDF models, at least for view angles $< 40\text{-}50^\circ$. However, for extreme off-nadir measurements the BRDF characterization is necessary.

Performance of these methods is generally evaluated by inter-comparison studies (Hook, Gabell, Green, and Kealy, 1992; Li, Becker, Stoll, and Wan, 1999). The errors associated with the different methods are due to method simplification, instrumental noise and calibration error, uncertainties in the downwelling irradiance, and incorrect atmospheric information. A comprehensive description of the various methods of LSE estimation from passive sensor data is given by Dash, Göttsche, Olesen, and Fischer (2002a). In the present research, the TISI method is chosen for LSE estimation based on the criteria of the availability of IR data and the need to process long time-series of data on a continental scale. The method is used with AVHRR data and has been tuned for MSG SEVIRI data; LSEs and LSTs are derived for a part of central Europe.

5 Thermal infrared spectral indices (TISI) method

Science has found that nothing can disappear without a trace. Nature does not know extinction. All it knows is transformation! Think about that for a moment. Once you do, your thoughts about life will never be the same... If God applied this fundamental principle to the most minute and insignificant parts of His universe, doesn't it make sense to assume that He applies it also to the Masterpiece of His creation--the human soul? I think it does. And everything science has taught me--and continues to teach me--strengthens my belief in the continuity of our spiritual existence after death. Nothing disappears without a trace.

Wernher von Braun (1912-1977)

The temperature-independent TISI method (Becker and Li, 1990a) calculates radiance ratios, which are independent of LST (land surface temperature) and related to LSE (land surface emissivity) ratios. Because the TISI (ratio of radiances) is independent of the unknown LST, it is possible to relate it solely to a ratio of the other unknown, *i.e.* LSE. The method does not use specific spectral information and is applicable to surfaces with wide emissivity-ranges. It is based on the power-law approximation of Planck's function (Slater, 1980):

$$B_k(T_s) = \alpha_k(T_0) T^{n_k(T_0)} \quad (21)$$

where α_k and n_k are channel-specific constants for modest temperature variations around a reference temperature T_0 ; at T_0 equation (21) and its first derivative with respect to T are exact and can be solved for α_k and n_k :

$$n_k(T_0) = \frac{c_2}{\lambda_k T_0} \left[1 + \frac{1}{\exp(c_2 / \lambda_k T_0) - 1} \right] \quad (22)$$

$$\alpha_k(T_0) = \frac{B_k(T_0)}{T_0^{n_k(T_0)}} \quad (23)$$

For a given wavelength and reference temperature, α_k and n_k (at T_0) can be determined from equation (22) and equation (23). However, for narrow-band channels and for a range of reasonable terrestrial LSTs (*e.g.* 270-320 K) α_k and n_k are obtained by linear regression (see section 5.1.1). Inserting equation (21) with channel-specific constants into equation (9) yields:

$$R_k = \alpha_k T_{B_k}^{sf c^{n_k}} = \varepsilon_k \alpha_k T_s^{n_k} C_k \quad (24)$$

where C_k is a pixel-wise atmosphere, and channel specific variable and is given by

$$C_k = 1 + [(1 - \varepsilon_k) L_k^\downarrow] / [\varepsilon_k B_k(T_s)].$$

TISI can be derived for any number of channels (two or more) and any of the channels (i, j, r). In order to obtain TISI for channels i and j , radiances for the two channels R_i and R_j given by equation (24) are ratioed with powers a_i and a_j :

$$\frac{R_i^{a_i}}{R_j^{a_j}} = \frac{\varepsilon_i^{a_i} \alpha_i^{a_i} T_s^{n_i a_i} C_i^{a_i}}{\varepsilon_j^{a_j} \alpha_j^{a_j} T_s^{n_j a_j} C_j^{a_j}} \quad (25)$$

At this point, it is required to assign reasonable values to a_i and a_j so as to make the above ratio independent of T_s , *i.e.* $n_i a_i - n_j a_j = 0$. The most obvious choice is $a_i = 1/n_i$ and $a_j = 1/n_j$.

However, in order to avoid complicated powers of emissivity and set one of the emissivities to the power of 1, Becker and Li (1990a) proposed $a_i = 1$ and $a_j = n_i/n_j$. In the present work,

$a_i = 1/n_i$ and $a_j = 1/n_j$; accordingly the TISI are also given as (Petitcolin, Nerry, and Stoll, 2002b):

$$\text{TISI}_{i,j} = \left[\frac{R_i}{\alpha_i} \right]^{\frac{1}{n_i}} \left[\frac{R_j}{\alpha_j} \right]^{\frac{-1}{n_j}} = \frac{\varepsilon_i^{\frac{1}{n_i}} C_i^{\frac{1}{n_i}}}{\varepsilon_j^{\frac{1}{n_j}} C_j^{\frac{1}{n_j}}} \quad (26)$$

The C -ratios depend on LSE, LST, and the atmosphere (section 5.1.2). Strictly, only for $T_s \rightarrow \infty$ or $\varepsilon_i = \varepsilon_j = 1$ the C -ratios equal 1. But for a wide range of LST and LSE, C -ratio = 1 holds approximately, at least in the $W2$ range, *i.e.* 8-13 μm (not in the $W1$ range). Rewriting equation (26) with the ε -ratio on one side, the TISI for emissivity (TISIE) is given by:

$$\text{TISIE}_{i,j} = \left[\frac{R_i}{\alpha_i C_i} \right]^{\frac{1}{n_i}} \left[\frac{R_j}{\alpha_j C_j} \right]^{\frac{-1}{n_j}} = \frac{\varepsilon_i^{\frac{1}{n_i}}}{\varepsilon_j^{\frac{1}{n_j}}} \quad (27)$$

The TISI method is a “relative” method and enables to calculate LSE-ratios. However assuming that LSE-ratios are constant for day and night, the TISI can be utilized to obtain absolute directional emissivities via the hemispherical surface reflectivity. The surface reflectivity can be inferred from the reflection of solar spectral irradiance in a channel r in $W1$. Then TISI-ratios are formed between channel r and channel i to calculate LSE in channel r . The TISIE can then be used to derive emissivities in other channels (i, j). The following sub-section deals with the derivation of absolute directional emissivity using the TISI method.

5.1 Obtaining directional emissivity from day-night data in 2 channels

Assuming that day and night LSE-ratios do not vary, equation (25) can be employed to estimate absolute angular LSE in $W1$ -channel, using a combination of day and night data. By rearranging equation (10), $\rho_r(\theta, \theta_{\text{Sun}}, \phi)$ is given by:

$$\rho_r(\theta, \theta_{\text{Sun}}, \phi) = \frac{R_{r,TOTAL}^D - R_r^D(T_s)}{E_{\text{Sun}}} \quad (28)$$

Hemispherical surface reflectivity is given as:

$$\rho_{hr}(\theta) = [\pi \rho_r(\theta, \theta_{\text{Sun}}, \phi)] / [F_r(\theta, \theta_{\text{Sun}}, \phi)] \quad (29)$$

where $F_r(\theta, \theta_{\text{Sun}}, \phi)$ is the angular form factor of the surface for channel r . A series of observations for different view-angles enables the retrieval of the angular dependence of reflectivity. Angular integration of ρ_r over the hemisphere yields hemispherical reflectivity:

$$\rho_{hr}(\theta) = \int_0^{2\pi} \int_0^{\pi/2} \rho_r(\theta, \theta_{\text{Sun}}, \phi) \cos(\theta) \sin(\theta) \partial\theta \partial\phi \quad (30)$$

If ρ_{hr} and ρ_r are known, BRDF can be characterized by rearranging equation (29) and LSE for non-Lambertian surface can be estimated from space (Nerry, Petitcolin, and Stoll, 1998). Despite the possibility to characterize non-Lambertian behavior of the Earth's surface, it is not common practice as the access to various concurrent angular observations for the same area is not prevalent with the current satellite systems. In the present work, the Lambertian assumption is made, *i.e.* $F_r(\theta, \theta_{\text{Sun}}, \phi) \approx 1$ in equation (29). For near-nadir measurements (view-angles up to 30–40°), this assumption holds with an error of 5% or less (Goïta and Royer, 1997; Sobrino and Cuenca, 1999). But for off-nadir views this assumption might lead to large errors up to 18%

(Nerry, Petitcolin, and Stoll, 1998). For geostationary observations, *e.g.* from MSG SEVIRI (Dash, Göttsche, and Olesen, 2002b) this drawback is not relevant. But for data from polar-orbiting satellites, *e.g.* NOAA AVHRR, considerable error is introduced for pixels with high view-angles. Additionally, for sea surfaces the assumption of Lambertian behavior does not hold due to high specular characteristic of water surface, hence, the sea-surface emissivities are set to channel-specific values (Table 2).

For utilizing equation (28), $R_{r,TOTAL}^D$ can be obtained from daytime measurements (*e.g.* in AVHRR channel 3 or SEVIRI channel 5) and E_{Sun} can be calculated (section 5.1.3). However, $R_r^D(T_s)$ has to be separately derived, because the available radiance $R_{r,TOTAL}^D$ is the sum of the emitted (terrestrial) and the reflected (solar) contributions. Here, applying the TISI approach to two channels (one in $W1$ and the other in $W2$), $R_r^D(T_s)$ can be deduced. Employing equation (25), temperature independent ratios $R_r^{\frac{1}{n_r}}/R_i^{\frac{1}{n_i}}$ for daytime and for night-time are constructed. Assuming that emissivity ratios do not vary between day and night and raising both left-hand side (LHS) and right-hand side (RHS) to the power of n_r , the two ratios can be solved for $R_r^D(T_s)$:

$$R_r^D(T_s) = R_r^N \left(\frac{R_i^D}{R_i^N} \right)^{\frac{n_r}{n_i}} \frac{C_r^D}{C_r^N} \left(\frac{C_i^N}{C_i^D} \right)^{\frac{n_r}{n_i}} \frac{\alpha_r^D}{\alpha_r^N} \left(\frac{\alpha_i^N}{\alpha_i^D} \right)^{\frac{n_r}{n_i}} \quad (31)$$

where N denotes night, D denotes day, and $\alpha_k^D = \alpha_k^N$ only for the same sensor (section 5.1.1).

For most materials and in absence of strong magnetic fields, the reciprocity of hemispherical surface reflectivity and the directional form of Kirchhoff's law holds (Snyder, Wan, and Li, 1998c). Inserting equation (31) and equation (28) into equation (29) yields $\rho_{hr}(\theta)$ and applying Kirchhoff's law gives:

$$\varepsilon_r(\theta) = 1 - \frac{R_{r,TOTAL}^D - R_r^N \left(\frac{R_i^D}{R_i^N} \right)^{\frac{n_r}{n_i}} \frac{C_r^D}{C_r^N} \left(\frac{C_i^N}{C_i^D} \right)^{\frac{n_r}{n_i}} \frac{\alpha_r^D}{\alpha_r^N} \left(\frac{\alpha_i^N}{\alpha_i^D} \right)^{\frac{n_r}{n_i}}}{\frac{1}{\pi} F(\theta, \theta_{Sun}, \phi) E_{sun}} \quad (32)$$

If the day and night radiances are taken from the same sensor, then the α -coefficients in equation (32) cancel out for same channels, *i.e.* α for a given channel is same for day and night. If radiances are taken from different sensors, *e.g.* day data from NOAA-14 AVHRR and night data from NOAA-12 AVHRR, then the individual α_k^D and α_k^N must be used. However, it is worth mentioning that LSE for a given surface and channel also varies with the sensor (Table 2) and the view angle, which is due to different response functions and angular behavior. Using data from different sensors is only due to data unavailability. In contrast, data from geostationary satellites are consistent, *i.e.* they have constant α_k and n_k and similar observation angles, *e.g.* data from MSG SEVIRI (Dash, Göttsche, and Olesen, 2002b).

From $\varepsilon_r(\theta)$ and surface radiances in channel i and j , $\varepsilon_i(\theta)$ and $\varepsilon_j(\theta)$ can be obtained either directly or by using TISIE ratios. As the TISIE ratios are more stable than single channel radiances in terms of accuracy, they are utilized to obtain the emissivities for the other channels (i, j). Using equation (27) for TISIE $_{r,i}$ at night-time, $\varepsilon_i(\theta)$ ($i = 4$ or 5 for AVHRR) is given by:

$$\varepsilon_i(\theta) = \text{TISIE}_{r,i}^{-n_i} \varepsilon_r(\theta)^{\frac{n_i}{n_r}} = \left[\frac{R_r}{\alpha_r C_r} \right]^{\frac{-n_i}{n_r}} \left[\frac{R_i}{\alpha_i C_i} \right] \varepsilon_r(\theta)^{\frac{n_i}{n_r}} \quad (33)$$

The channel radiances in equation (32) are obtained from TOA (top-of-the-atmosphere) measurements after atmospheric corrections (section 2.4). The derivation of the other coefficients and variables is given below.

5.1.1 Coefficients of TISI method for SEVIRI and AVHRR

The coefficients α_k and n_k are constants of channel k for a given temperature range. They are usually calculated for a sampled temperature range (e.g. 270-310 K with 0.05 K increment). For each temperature, Planck's function for channel radiance B_k is calculated. Taking natural logarithms of equation (21) yields:

$$\ln(B_k(T)) = \ln(\alpha_k) + n_k \ln(T) \quad (34)$$

The coefficients α_k and n_k are given by the intercept and slope (Figure 9) of the linear regression with equation (34).

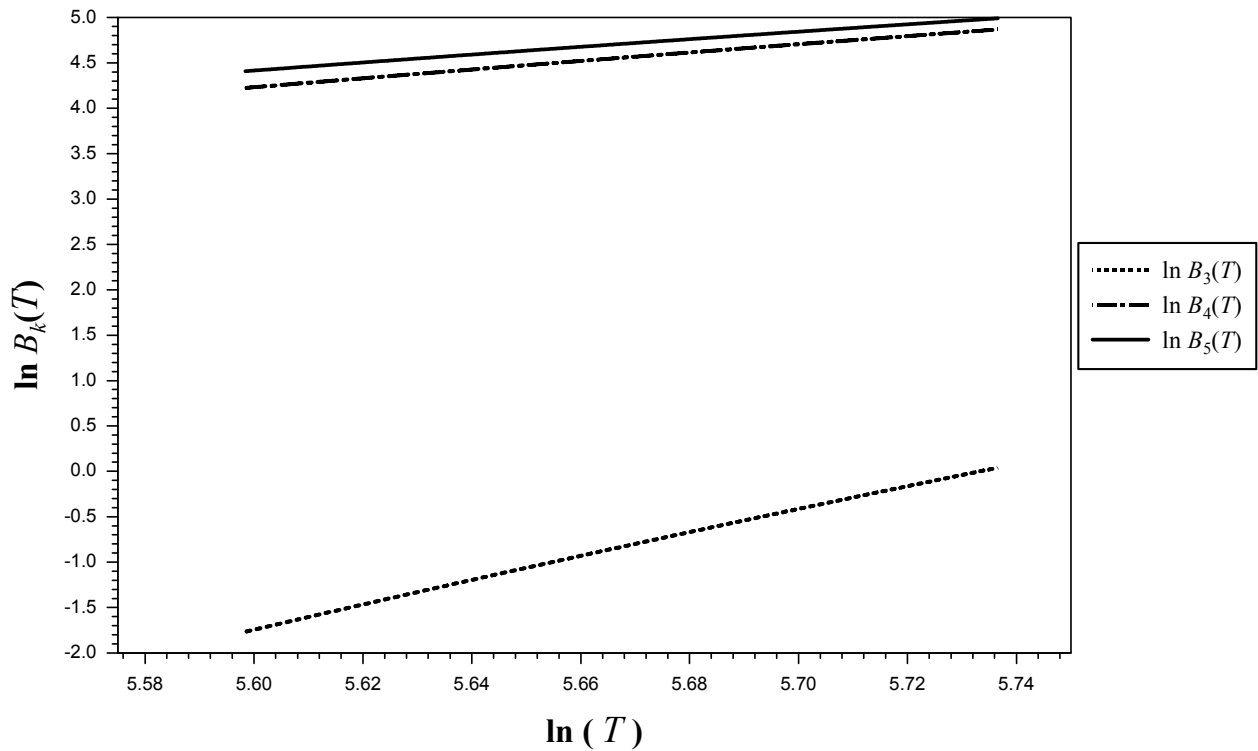


Figure 9: Regression line for power-law approximation of Planck's law of channel radiance. Equation (34) is employed for NOAA-14 AVHRR channels 3, 4, and 5, for a sampled temperature range of 270-320 K increment. Then n_k is obtained from the slope and α_k is derived from the exponent of the intercept for each of the channels.

For a temperature range of 270-310 K, Table 3 gives the values of α_k and n_k for the window channels of MSG-1 SEVIRI (Dash, Göttsche, and Olesen, 2002b) and gives the coefficients for the window channels of AVHRR, of NOAA 09-16.

Channel (μm)	NEAT (K)	α_k (270-310 K) $\left[\frac{\text{mW}}{\text{m}^2 \text{sr cm K}} \right]$	n_k (270-310 K)	RMS error in $T(\text{K})$ due to power-law	Max. error in $T(\text{K})$ due to power-law	MSG Series
5 (IR 3.8)	0.11	$1.247 \cdot 10^{-31}$	12.479	0.20	0.46	MSG-1
8 (IR 8.7)	0.07	$4.813 \cdot 10^{-13}$	5.726	0.20	0.45	
10 (IR 10.8)	0.07	$3.334 \cdot 10^{-10}$	4.654	0.20	0.44	
11 (IR 12.0)	0.11	$4.278 \cdot 10^{-9}$	4.230	0.19	0.45	

Table 3: The window channels of MSG-1 SEVIRI, their noise-equivalent temperature differences (NEAT), and channel-specific coefficients for the power-law approximation of Planck's law obtained by linear regression.

Channel (μm)	NEAT (K)	α_k (270-310K) $\left[\frac{\text{mW}}{\text{m}^2 \text{sr cm K}} \right]$	n_k (270-310 K)	RMS error in $T(\text{K})$ due to power-law	Max. error in $T(\text{K})$ due to power-law	NOAA Series
3B (IR 3.71)	< 0.12	$1.062 \cdot 10^{-33}$	13.223	0.20	0.46	NOAA-16
4 (IR 10.89)		$4.650 \cdot 10^{-10}$	4.599	0.20	0.46	
5 (IR 11.96)		$4.683 \cdot 10^{-09}$	4.214	0.19	0.42	
3B (IR 3.71)		$8.740 \cdot 10^{-34}$	13.256	0.20	0.47	NOAA-15
4 (IR 10.80)		$3.676 \cdot 10^{-10}$	4.638	0.20	0.46	
5 (IR 11.91)		$4.190 \cdot 10^{-09}$	4.233	0.19	0.45	
3 (IR 3.78)		$3.201 \cdot 10^{-33}$	13.053	0.20	0.47	NOAA-14
4 (IR 10.76)		$3.350 \cdot 10^{-10}$	4.653	0.20	0.44	
5 (IR 11.97)		$4.820 \cdot 10^{-09}$	4.210	0.19	0.43	
3 (IR 3.79)		$3.800 \cdot 10^{-33}$	13.027	0.20	0.47	NOAA-12
4 (IR 10.86)		$4.240 \cdot 10^{-10}$	4.614	0.20	0.44	
5 (IR 11.95)		$4.490 \cdot 10^{-09}$	4.221	0.19	0.42	
3 (IR 3.79)		$1.351 \cdot 10^{-33}$	13.188	0.20	0.47	NOAA-11
4 (IR 10.86)		$3.446 \cdot 10^{-10}$	4.648	0.20	0.46	
5 (IR 11.95)		$3.921 \cdot 10^{-09}$	4.244	0.19	0.43	
3 (IR 3.79)		$9.494 \cdot 10^{-34}$	13.242	0.20	0.47	NOAA-09
4 (IR 10.86)		$3.154 \cdot 10^{-10}$	4.663	0.20	0.46	
5 (IR 11.95)		$3.500 \cdot 10^{-09}$	4.263	0.19	0.43	

Table 4: The window channels of NOAA AVHRR, their noise-equivalent temperature differences (NEAT), and channel-specific coefficients for the power-law approximation of Planck's law obtained by linear regression.

5.1.2 Estimation of a pixel-wise atmosphere and channel specific variable

Inserting equation (18) into equation (24), the C_k can be reformulated as:

$$C_k = \frac{1 - \frac{L_k^\downarrow}{B_k(T_s)}}{1 - \frac{L_k^\downarrow}{R_k(T_s)}} \quad (35)$$

where the variables on the RHS (right-hand side) are the same as for equation (9). L_k^\downarrow is obtained from meteorological data (atmospheric temperature and moisture profile) and RTCs (radiative

transfer calculations). L_k^\downarrow is the hemispherical irradiance divided by π , but the RTMs (radiative transfer models), e.g. MODTRAN-3, calculate in one direction from-source-to-target (not integrated over the hemisphere). Hence, for computational simplifications the diffusive approximation is assumed and L_k^\downarrow is calculated as downwelling radiance for a zenith angle of 53° (Coll, Caselles, Rubiuo, Sospedra, and Valor, 2000). The assumption is that the hemispherical downwelling atmospheric irradiance is π times $L_k^\downarrow(53^\circ)$ (Kondratyev, 1969). As L_k^\downarrow is not directly used for atmospheric correction in equation (8) but only to derive C_k (which are also used as ratios), this assumption is uncritical. However, recent updates of RTMs, e.g. MODTRAN-4 (Berk *et al.*, 2000), have reportedly improved the calculations (Richter and Coll, 2002). $R_k(T_s)$ is obtained using equation (8), except for daytime $W1$ data, i.e. $R_r(T_s)$. Assuming $C_{ri} \approx 1$ ($C_{ri} = C_r / C_i^{n_{ri}}$) in equation (31), gives a first approximation of $R_r(T_s)$, which is used in equation (35) to estimate C_r (Nerry, Petitcolin, and Stoll, 1998). The only unknown in equation (35) is $B_k(T_s)$, which is estimated from equation (9):

$$B_k(T_s) = \frac{R_k - (1 - \epsilon_k)L_k^\downarrow}{\epsilon_k} \quad (36)$$

The natural variation of LSE is less for $11.5\text{-}12.5 \mu\text{m}$ (e.g. AVHRR channel-5) than for $10.5\text{-}11.5 \mu\text{m}$ (e.g. AVHRR channel-4). Hence for AVHRR, $B_5(T_s)$ is obtained using an initial assumed emissivity of 0.98. The T_s obtained from the inverse of $B_5(T_s)$ is then used to calculate the $B_k(T_s)$ in other channels and subsequently C_k using equation (35). For faster calculations, the estimated T_s is used to pick up the $B_k(T_s)$ in the other channels from LUTs pre-calculated with a temperature interval of 0.05 K.

The TISI method in its basic form does not require *a priori* emissivity, and yields only channel LSE ratios. To obtain absolute angular LSE using TISI, an initial emissivity has to be used in order to estimate C_k . However, this initial emissivity is only used in C_k , which also is used only in the form of a ratio [equations (32) and (33)]; hence, its impact is small. For AVHRR data and using three-channel TISI Nerry, Petitcolin, and Stoll, (1998) showed that the error in LSE due to this approximation does not exceed 0.14%. In the present study, an analysis was performed for AVHRR data over central Europe; for an assumed emissivity ranging from 0.94 to 0.99, the variation of final LSEs was only of order of 0.0001-0.001. As this error is much less than the final errors (achievable accuracy), the assumption is uncritical. An initially envisaged idea was to: a) reduce the error by successive iterations once initial LSEs were obtained (using them to recalculate C_k), or b) supply realistic LSE values from other easier methods (NDVI-based) to calculate C_k . However, as the assumption turned out to be uncritical, the idea was not implemented.

5.1.3 Determination of solar spectral irradiance at ground level

Spectral irradiance (E) is the spectral radiant flux per unit area ($\text{W}/(\text{m}^2\mu\text{m})$). The TOA solar spectral irradiance (E_{Sun}^{TOA}) for channel r is:

$$E_{Sun}^{TOA} = B_r(T_{Sun}) \frac{\pi R_{Sun}^2}{D^2} \quad (37)$$

where $B_r(T_{Sun})$ is solar radiance in channel r for Sun's surface temperature, T_{Sun} is effective blackbody temperature at Sun's surface ≈ 5820 K, $R_{Sun} \approx 6.950 \cdot 10^8$ m is the mean radius of Sun, and $D_{mean} \approx 1.487 \cdot 10^{11}$ m is Sun-Earth distance.

The variation of D leads to a variation in E_{Sun}^{TOA} of $\pm 3.5\%$ (Howard, 1991). This variation can be accounted for by a rectification factor d in equation (37) (Spencer, 1971):

$$E_{Sun}^{TOA} = B_r(T_{Sun}) \frac{\pi R_{Sun}^2 d}{D_{mean}^2} \quad (38)$$

where $d = 1.00011 + 0.034221 \cos(\varphi) + 0.00128 \sin(\varphi) + 0.000719 \cos(2\varphi) + 0.000077 \sin(2\varphi)$, φ is day angle in radians $= 2\pi(\text{DOY} - 1)/365$; (DOY = Julian day of the year).

The solar spectral irradiance at ground E_{Sun} can be estimated as:

$$E_{Sun} = \tau_r(\theta_{Sun}) E_{Sun}^{TOA} \cos(\theta_{Sun}) \quad (39)$$

where $\tau_r(\theta_{Sun})$ is the spectral transmittance along the path of sunlight.

The solar channel irradiance E_{Sun}^{TOA} also depends on the channel response function. Therefore it has to be calculated individually for each sensor. The surface E_{Sun} for a given date (position of the Sun), location, and atmosphere can also be directly obtained by employing the RTMs, e.g. MODTRAN. This approach is preferred and is performed in the present study. Figure 10 shows the TOA solar irradiance in AVHRR channel 3 for NOAA 12-16.

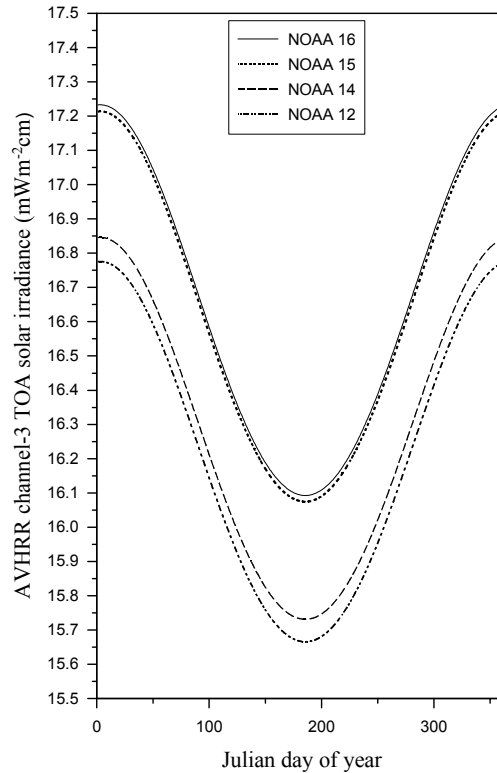


Figure 10: Annual variation of TOA solar irradiance in AVHRR channel-3 for NOAA12, 14, 15, 16

5.2 Optimizing the two-channel TISI for AVHRR and SEVIRI

For employing equation (32), two channels ($W1$ and $W2$) are required. AVHRR and SEVIRI have one channel each in $W1$ range (3-4 μm), but two channels in $W2$ range (8-13 μm), *e.g.* AVHRR channels-4, 5, and SEVIRI channels-10, 11. Among the principal absorbers in $W2$, *i.e.* H_2O , CO_2 , HNO_3 , CF_2Cl_2 , and O_3 (absorption at $\sim 9.6 \mu\text{m}$), H_2O (water vapor) is responsible for the fast variation of atmospheric effects. It is evident from the absorption spectra that the channel around 11 μm (*i.e.* SEVIRI channel-10, AVHRR channel-4) is less affected due to H_2O absorption than the channel around 12 μm (*i.e.* SEVIRI channel-11, AVHRR channel-5). CO_2 shows a reverse effect (absorption at 10.4 μm). However, as CO_2 is a well mixed gas with very slow variation in time (over years) of low concentration, its effect is smaller and is well quantified. Hence, in $W1$ and $W2$ attenuation is mainly due to H_2O and the channel around 11 μm is less affected than the channel around 12 μm (Figure 6). Consequently, in the present study the channel around 11 μm is used for TISI and for estimating LSE in $W1$ -channel.

Inserting MSG-1 coefficients (Table 3) into equation (32), and using channel-5 and channel-10 radiances (Dash, Göttsche, and Olesen, 2002b, 2003), channel-5 SEVIRI LSE is:

$$\varepsilon_5(\theta) = 1 - \frac{R_{5,TOTAL}^D - R_5^N \left(\frac{R_{10}^D}{R_{10}^N} \right)^{2.682} \frac{C_5^D}{C_5^N} \left(\frac{C_{10}^N}{C_{10}^D} \right)^{2.682}}{\frac{1}{\pi} E_{Sun}} \quad (40)$$

Similarly, inserting NOAA-14 coefficients (Table 4) into equation (32), and using channel-3 and channel-4 radiances, AVHRR channel-3 LSE is given by:

$$\varepsilon_3(\theta) = 1 - \frac{R_{3,TOTAL}^D - R_3^N \left(\frac{R_4^D}{R_4^N} \right)^{2.806} \frac{C_3^D}{C_3^N} \left(\frac{C_4^N}{C_4^D} \right)^{2.806}}{\frac{1}{\pi} E_{Sun}} \quad (41)$$

5.3 Method validation using simulated surface radiances

Numerical simulations using RTMs provide a first-hand access to algorithm validation. Field-measurements are necessary for ultimate validation; however, many variables, *e.g.* LSE and LST, cannot be easily measured in the field at the spatial scale of the sensor. Consequently, it is not always feasible to determine the accuracy of LSE and LST methods from field data. In the present study the method is first validated using synthetic data.

For method validation a set of channel-specific emissivities was generated (Table 1 and Table 2). For a set of surface types and for day and night representative LSTs, surface NOAA-14 AVHRR channel radiances (R_k) were calculated using MODTRAN-3.7 for tropical, MLS, MLW, SAS, SAW, and 1976 US standard model atmospheres. Subsequently emissivities were retrieved using equation (41). Once channel-3 emissivity is known, emissivities in the other channels can be easily derived either using equation (33) or directly. Figure 11 shows input LSE versus estimated LSE for several surfaces in channels 3, 4, and 5 of NOAA-14 AVHRR.

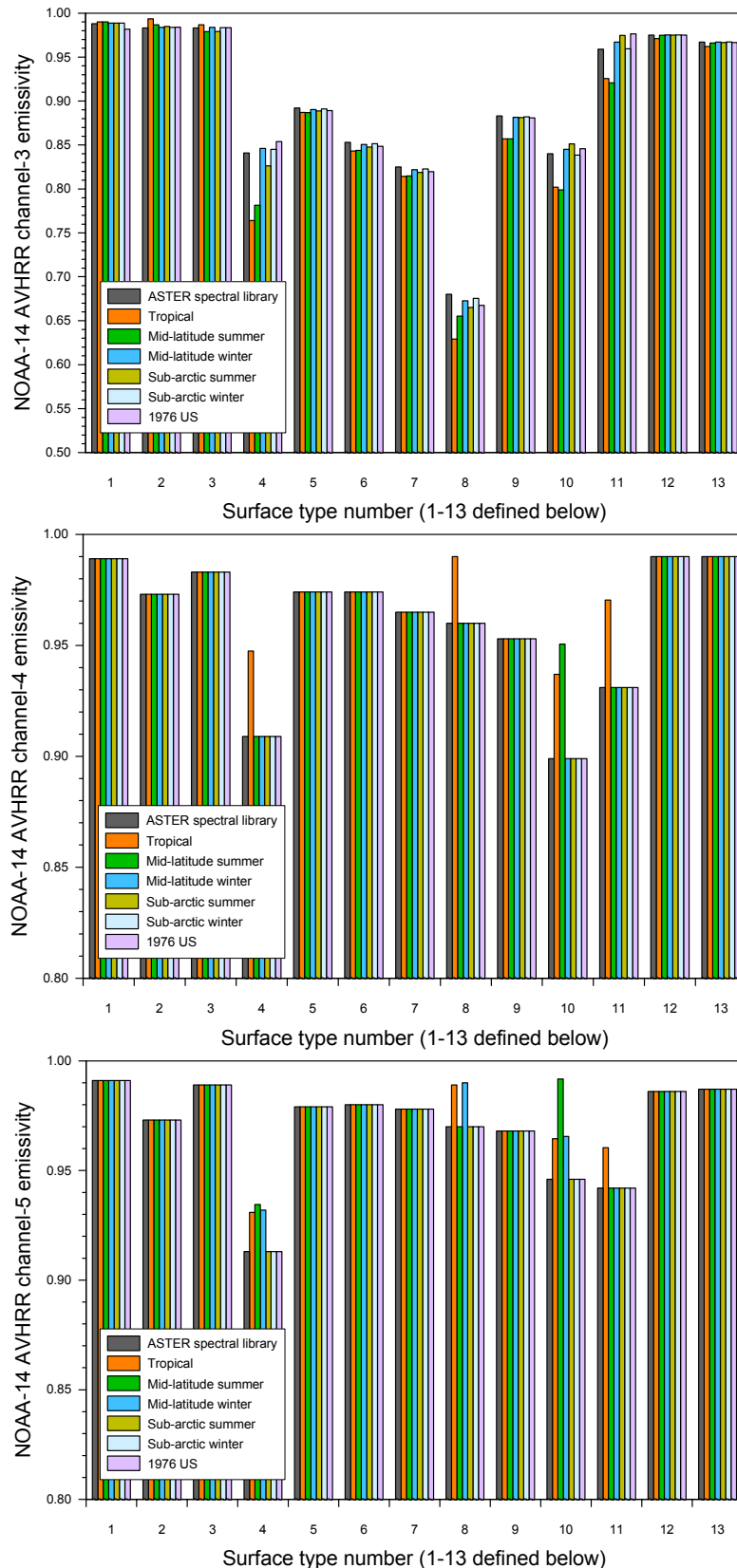


Figure 11: NOAA-14 AVHRR input channel emissivities (derived by convolution of ASTER spectral library emissivities with corresponding channel response functions) versus estimated emissivities using the two-channel TISI scheme. Upper panel shows channel-3 emissivity, middle panel shows channel-4 emissivity, and lower panel shows channel-5 emissivity. Surface radiances were simulated for model atmospheres with emissivities of various surface types: (1) coniferous tree, (2) deciduous tree, (3) grass, (4) dry grass, (5) black loam soil, (6) brown silty loam soil, (7) dark brown sand, (8) yellow loamy sand, (9) construction concrete, (10) slate stone shingle (11) white marble, (12) sea water (13) sea foam.

The *RMS* error of the emissivities derived using the two-channel TISI is 0.016 for channel-3, 0.009 for channel-4, and 0.005 for channel-5. It was assumed that the atmospheric information was accurate, and that the checkerboard surfaces follow Lambertian behavior. The errors were maximum for tropical atmosphere (extreme) and surfaces such as dry grass, yellow loamy sand, slate stone shingle, and white marble. Dash, Göttsche, and Olesen (2002b) performed a similar validation study for MSG SEVIRI which resulted in an error of 0.031 for channel-5, 0.016 for channel-10, and 0.009 for channel-11 emissivities. The method was validated for MSG SEVIRI using MLS, MLW, and tropical atmospheres and was later applied to NOAA-14 AVHRR data (Dash, Göttsche, and Olesen, 2003).

The errors given above are primarily due to the power-law approximation and the assumed emissivity for estimating C_k and B_k . The magnitude of the error is in agreement with previous work using three-channel TISI (Nerry, Petitcolin, and Stoll, 1998), which reported that the error due to approximation and the instrumental-error do not exceed 1% (in W_2 range) and are negligible. However, atmospheric corrections are critical; an uncertainty of $\pm 0.5 \text{ g}\cdot\text{cm}^{-2}$ in atmospheric water vapor will result in an error of 2.5% in emissivity and 2.5 K in LST (Goita and Royer, 1997). The effect of the angular form factor has also to be considered, *i.e.* either it is supplied from external database or only near-nadir measurements are used.

5.4 Error reduction and performance enhancement

The errors result from method simplification, improper atmospheric information, and measurement errors due to the instrument. The atmospheric corrections can only be as good as the input information. In the present study, European Centre for Medium-Range Weather Forecasts (ECMWF) model analysis data is used. The available atmospheric information cannot be further improved and it is assumed it to be accurate. The error due to the instrument cannot be eliminated either, except if there is a bias. However, with improved sensors noise is negligible, *e.g.* NEAT for AVHRR $< 0.12 \text{ K}$; NEAT for SEVIRI $< 0.11 \text{ K}$ in channel- 5,11 and < 0.07 in channel 10. From a scientific point of view, the primary interest lies in reducing the error due to method simplification (approximations and assumptions), and improving the performance, *e.g.* the speed of calculations.

5.4.1 Normalization of estimated emissivities

Due to errors from various sources, *i.e.* $F_r(\theta, \theta_{Sun}, \phi)$, E_{Sun} , misregistration of day and night scenes, as well as varying zenith angles and imperfections in atmospheric models, the occurrence of emissivities with values larger than one is possible (Li and Becker, 1993). In order to remove these physically impossible emissivities, they are normalized by the highest observed value. Unlike as by Li and Becker (1993), not all pixels but only the defective emissivities (if any) are normalized with respect to some highest permitted value, as the artifact could be systematic or random. This is performed for channel-5 (AVHRR) emissivities, because they vary the least, and then LST is calculated from channel-5 LSE.

5.4.2 One-step iterative approach for error reduction

To reduce the errors induced by the assumptions, the initially calculated channel-3 reflectivities are used in rearranged equation (10) to recalculate $R_r(T_s)$, and $B_r(T_s)$ is recalculated employing

equation (36). Using recalculated $R_r(T_s)$, and $B_r(T_s)$ values, day C_r values are recalculated and the subsequent procedures are repeated once.

5.4.3 Use of temperature-to-radiance conversion look-up tables

In order to use the LSE algorithm surface radiances are required, but usually TOA BTs (brightness temperatures) are provided. The BTs are converted to radiances using equation (3). After first estimation of $B_5(T_s)$ (assuming an initial emissivity) it is also required to calculate $B_k(T_s)$ for the other channels. This process is unsuitable in an operational environment. Hence, pre-calculated LUTs (temperature-radiance for each channel) are used, which were designed at 0.05 K interval. The accuracy of the temperature-to-radiance conversion or *vice versa* is high due to the small T interval and the access time for the LUTs is small due the use of an efficient binary search algorithm. For a scene of 1536 x 1450 pixels and for 3 channels, the time for conversion is less than 30 seconds on a SUN Ultra-Sparc with 450 MHz processor. Once surface radiance and LSE are known, the emitted part is separated from the total radiance and converted to LST using the procedure described above.

6 Description of the present work and data

Wisdom is not communicable. The wisdom which a wise man tries to communicate always sounds foolish. Knowledge can be communicated, but not wisdom. One can find it, live it, be fortified by it, do wonders through it, but one cannot communicate and teach it.

Hermann Hesse (1877- 1962)

In *Siddhartha*

The TISI method requires surface radiances. Hence, atmospheric correction of NOAA-14 AVHRR data was performed employing equation (8). Atmospheric information for the study area was derived from global ECMWF re-analyses (ERA-15) profiles for the corresponding date at the 4 main synoptic times: 00, 06, 12, and 18 hours Coordinated Universal Time or *Universel Temps Coordonné* (UTC). In the present study, 12 and 00 hours UTC ERA-15 are temporally closest to the acquisition time: the data from NOAA AVHRR over the study area are acquired about two hours later. Here, it is assumed that the atmosphere does not substantially change in two hours - partly because the assumption holds for most cases except under extreme weather conditions, and partly due to the unavailability of concurrent information. The data from MSG SEVIRI can be used to match the ECMWF times and avoid this temporal mismatch. The ECMWF profiles provided atmospheric information as input to MODTRAN-3.7 for calculating upwelling and downwelling atmospheric transmittances and radiances, and solar radiances at the surface in $W1$ range (3-4 μm). The results were then interpolated to AVHRR spatial resolution (see section 6.3). From surface radiances LSEs (land surface emissivities) for channel-3 were calculated using equation (32) and subsequently LSEs for the other channels were derived from equation (33). Finally, temperatures were extracted from channel-5 surface radiances and known LSEs. Figure 12 shows a schematic diagram of the two-channel TISI procedure.

Zenith angle and elevation determine the path-length between source and target. Hence, calculations were performed for the given zenith angles and a range of elevations (actual height and 3 heights around it). MODTRAN is used in 3 different modes of calculation:

- a) upward path radiance,
- b) approximate downwelling radiance, and
- c) solar radiance for given location and solar geometry.

The results of the radiative transfer calculations were transformed from spectral to channel-specific values using response functions. MODTRAN uses response functions which are normalized to unit area (not to 1 as in section 2.1.1). Hence, response functions (normalized to 1) were transformed to functions normalized over the area (<http://imk-msa.fzk.de/msa-public/Explanations/Explanations.htm>).

6.1 Study area

The study area includes a large part of the land surface of Europe; the area is a part of the so-called ‘Italy window’, as defined in the ‘Remote Sensing of the Mediterranean Desertification and Environmental Stability’ (RESMEDES) project. The upper-left and lower-right geographical co-ordinates of the whole window are $55^\circ \text{ N}-5^\circ \text{ E}$ and $40^\circ 30' 11.6'' \text{ N}-20^\circ 21' 09.4'' \text{ E}$, respectively. The land surface types in this area are representative for most of southern and central Europe. For comparison purposes with various other data, smaller parts of this large area are analyzed.

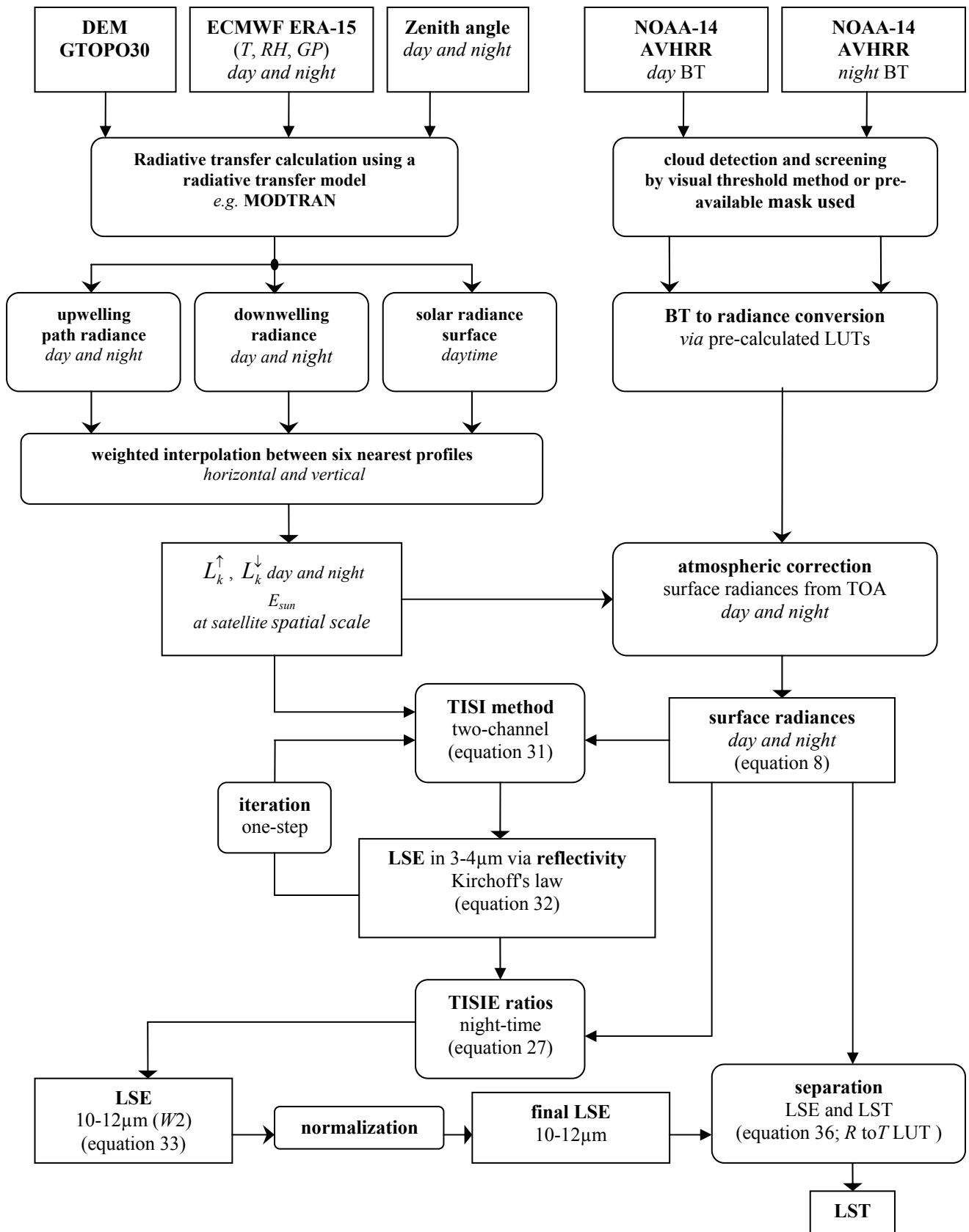


Figure 12: The two-channel TISI method for LSE and LST estimation.

In the following sections, the study area, the data sets used, and the program and software employed, are briefly described.

6.2 Data description

In the present work, NOAA-14 AVHRR spatial data (re-projected data from the Institute of Meteorology, FU Berlin), ERA-15 (from ECMWF), United States Geological Survey (USGS) Global 30 arc second elevation data (GTOPO30), and other auxiliary data sets were used, *e.g.* solar zenith angle, University of Maryland 1 km global land cover type, and World Data Bank (WDB) coastlines and international boundaries vector data. Furthermore, emissivity values were derived from ASTER spectral library for simulation purposes.

6.2.1 AVHRR data from NOAA satellites

In this study, TOA (top-of-the-atmosphere) measurements made by the AVHRR sensors onboard NOAA's Polar Orbiting Environmental Satellites (POES) are used. The AVHRR is a broad-band scanner, sensing in the visible, near-infrared (NIR), and terrestrial-infrared (TIR) portions of the electromagnetic spectrum (Kidwell, 1998). It is carried on NOAA's POES, beginning with TIROS N in 1978: TIROS N, NOAA 6-12, 14, 15, 16, and 17. The AVHRR provides global (pole to pole) on-board collection of data. Each pass of the satellite has a 2399 km wide swath and the satellite orbits the Earth about 14.1 times per day (orbital period of 102 min) at an altitude of about 850 ± 30 km. Since the number of orbits per day is not an integer, the sub orbital tracks are not repeated on a daily basis; however, the local solar time of each satellite track is essentially unchanged for each latitude. An ascending node implies a northbound equatorial crossing and a descending node implies a southbound equatorial crossing. Until NOAA 14 the AVHRR was flown as a 4-channel (morning passes) or a 5-channel instrument (afternoon passes); in the case of the "morning satellites" one of the IR channels was switched off. Starting with NOAA 15 or the first satellite of the KLM-series an additional channel is available, which is used alternately with channel 3; these are together referred to as channel 3a and 3b (Goodrum, Kidwell, and Winston, 2000). In future, the polar satellite system will be maintained together by NOAA POES (NOAA-N and -N') and the EUMETSAT polar system (EPS) satellite series Metop 1, 2, and 3, of which the first is due for launch in 2005. EPS Metop will provide the "morning satellites" and NOAA POES the "afternoon satellites"; both will carry a set of identical instruments to ensure data continuity. The instruments include AVHRR, high resolution IR radiation sounder (HIRS), advanced microwave sounding unit AMSU-A, and microwave humidity sounder (MHS). In addition to these core instruments, both satellites will carry additional specific instruments: NOAA POES will carry the latest solar backscatter ultraviolet instrument (SBUV), and Metop will carry the infrared atmospheric sounding interferometer (IASI), the global ozone monitoring experiment (GOME) instrument, the global navigation satellite system (GNSS) receiver for atmospheric sounding (GRAS), and the advanced scatterometer (ASCAT). Figure 13 shows Metop with its instruments.

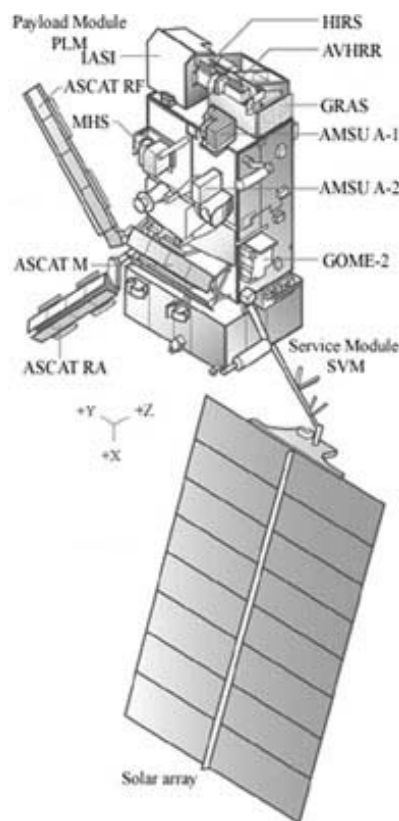


Figure 13: Metop spacecraft configuration with instruments (source: <http://www.eumetsat.de>).

AVHRR data are acquired in 2 formats: a) local area coverage (LAC), and b) global area coverage (GAC). The average instantaneous field-of-view (IFOV) of 1.4 milliradians results in a LAC ground resolution of about 1.1 km at the nadir. The GAC data are derived from on-board sampling: taking 4 out of 5 pixel averages cross track and every third line from full AVHRR resolution result in 4 km resolution at nadir.

In the present study, pre-processed AVHRR-data were obtained from the Institute of Meteorology, Free University of Berlin (<http://www.met.fu-berlin.de>). The digital numbers (DN) in the IR channels were calibrated (conversion to BTs using calibration coefficients) and digitized in $1/100^{\circ}\text{C}$. Data were projected in a platform-independent lat/lon grid with 0.01 degree resolution (about 1 km spatial resolution).

The methods developed and implemented in this work are also designed to process data from SEVIRI onboard the geostationary MSG satellite. SEVIRI (Figure 2) has IR channels very similar to those of AVHRR (Figure 1) and will provide data with an unprecedented combination of spatial, temporal, and spectral resolutions with an improved potential for LSE and LST estimation (Dash, Göttsche, and Olesen, 2002b). MSG SEVIRI data will also be received with a HRUS (1028 Kbit/s) installed at the MSA research group.

6.2.2 ECMWF Re-Analyses (ERA) atmospheric profiles

The ECMWF global re-analyses are available for the 4 main synoptic hours (00, 06, 12, and 18 hours UTC; ECMWF User guide, 1995). Information about the state of the atmosphere for a given date and for the closest time is obtained from ERA-15. These operational deterministic model data provide profiles of temperature (T), relative humidity (RH), and geo-potential (GP)

with 106 wavenumbers spectral resolution, yielding a 1.1° latitude/longitude spatial grid resolution. The data for the study area were transformed from spectral grid into spatial data and T, RH, and GP profiles with 14 pressure levels were extracted. An advantage of using ERA-15 is their availability on a global scale irrespective of cloud cover or acquisition problems which enables processing of long time-series of data. Studies have shown that ECMWF re-analyses yield atmospheric corrections comparable to those from radiosonde or TOVS data (Schroedter, Olesen, and Fischer, 2003).

6.2.3 Digital elevation data

The most important topographic effect is due to elevation, as the atmospheric path-length directly influences TOA radiances. Hence, USGS GTOPO30 DEM was used to determine the path-length for atmospheric corrections. Figure 14 shows the DEM data over the study area.

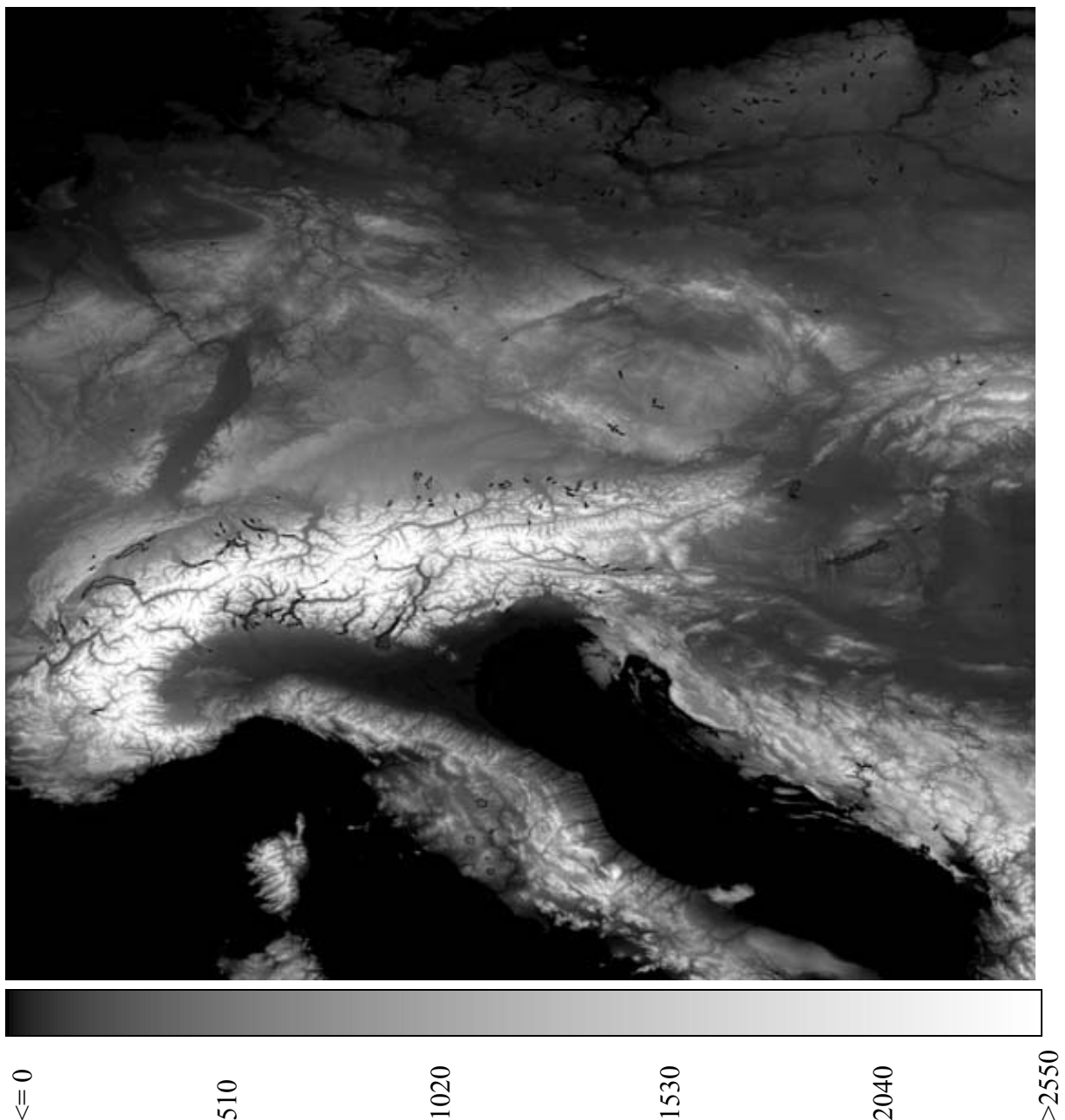


Figure 14: USGS GTOPO30 DEM data over the study area. The black pixels represent the sea-surface and elevation is given in mts. [upper-left: 55° N- 5° E lower-right: $40^\circ 30' 11.6''$ N- $20^\circ 21' 09.4''$ E]

These DEM data are available at <http://edcdaac.usgs.gov/gtopo30/gtopo30.html>. These are spaced at 30 arc seconds in 16 bit signed integer format. The 30 arc second grid spacing corresponds to about 1 km, but pixel-size decreases in the direction of the poles as latitude increases. Hence the elevation data is projected from geographic coordinates to an equal area representation.

6.2.4 University of Maryland (UMD) 1 km global land cover data set

The land cover types for the study area are derived from the “University of Maryland (UMD) 1 km Global Land Cover Data Set”, which is based on NOAA AVHRR data (Hansen, DeFries, Townshed, and Sohlberg, 2000). Exploiting the seasonality of vegetation, the UMD land cover data classifies Earth's surface into 14 cover types. This information is used in the present work for qualitative comparisons of LSEs with surface types. Figure 15 shows the histogram of land cover type distribution, which gives a broad idea about the variability of land surface over the area of study. Figure 16 shows the surface type map.

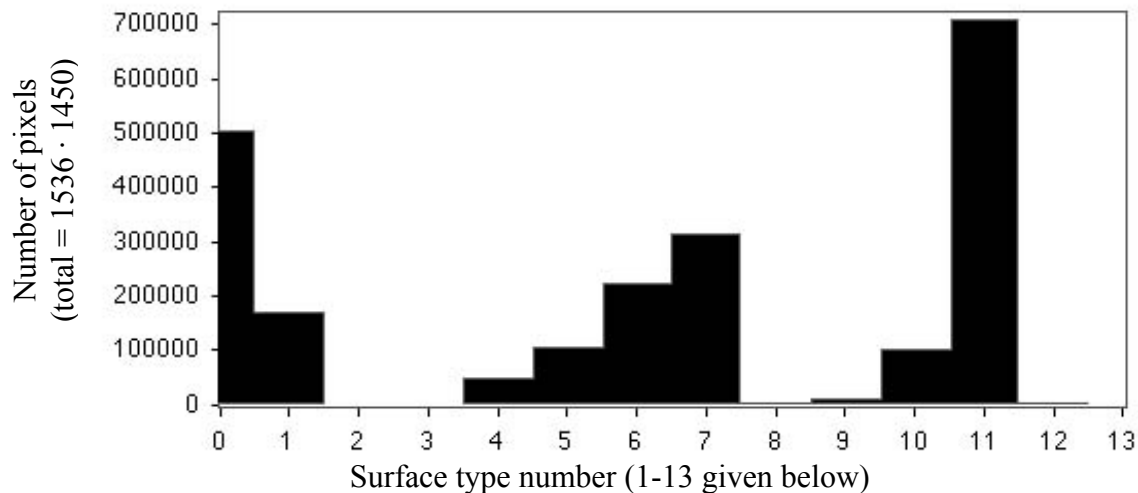


Figure 15: Frequency of distribution of land cover type over the study area.

Surface types: 0. Water 1. Evergreen needle forest 2. Evergreen broadleaf forest 3. Deciduous needleleaf forest 4. Deciduous broadleaf forest 5. Mixed forest 6. Woodland 7. Wooded grassland 8. Closed shrubland 9. Open shrubland 10. Grassland 11. Cropland 12. Bareground 13. Urban and built-up

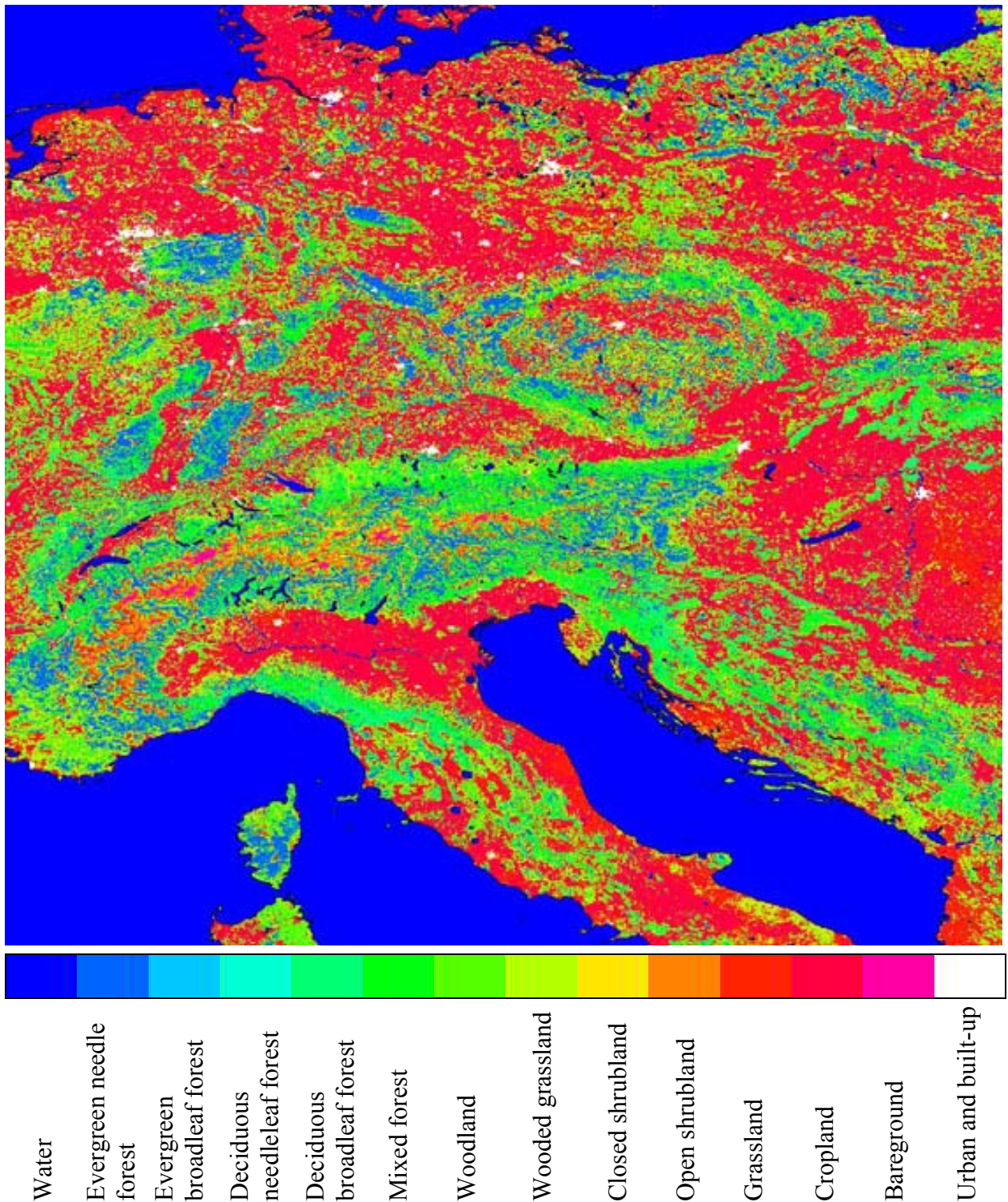


Figure 16: University of Maryland land cover types for the study area. The land cover map is based on the seasonality of vegetation and classifies the surface of the globe into 14 cover types. The area is a part (upper-left: 55° N–5° E lower-right: 40°30'11.6" N–20°21'09.4" E) of the so-called Italy-window and the data is at the spatial resolution of re-sampled 1 km AVHRR data provided by Institute of Meteorology, FU Berlin.

6.3 Spatial interpolation of atmospheric information

Atmospheric profile data are usually either sparse in space and time (*e.g.* radiosonde) or have much coarser spatial resolution than satellite data (*e.g.* ERA-15 of ~ 100 km spatial resolution). RTMs (radiative transfer models) yield results only for the locations of the atmospheric profiles. For pixels, which are not co-located with a profile, the results have to be interpolated in an effective way, which also must be able to handle irregularly spaced data of different horizontal resolution and varying elevation. For this purpose, the procedure of Schroedter, Olesen, and Fischer (2003), which is based on the method of Shepard (1968), was chosen. It uses the distance between the currently processed pixel and the six (or any suitable number) nearest atmospheric profiles. The original method was designed to interpolate atmospheric corrections (*i.e.* TOA BT - LST). In the present study, the method is modified to directly interpolate the atmospheric variables, *e.g.* L_k^\uparrow , L_k^\downarrow , and E_{Sun} . The RTCs (radiative transfer calculations) were performed for the exact scan angle at the locations of the profiles and for 4 different heights. For the ECMWF locations, the corresponding zenith angles and elevations were extracted from AVHRR zenith angles and USGS GTOPO30 DEM, respectively. The scan-angle influences the path-length, but the variation of the scan-angle is very small within a radius of approximately 100 AVHRR pixels. Hence, only the exact scan angle was used. However, elevation varies substantially and randomly. Therefore, 4 different heights were used to cover a reasonable variation of height. The overall interpolation is a 2-step process: a) the weight of each of the 6 nearest atmospheric profiles is based on its distance from the pixel under consideration, and b) an interpolation between the RTCs for elevation variation to the exact pixel elevation. The inclusion of only 6 points is a trade-off between computational speed with desired accuracy and smoothness of the interpolated atmospheric variables.

6.4 Cloud detection and screening

Daytime cloudy pixels are discarded by using cloudmasks available courtesy of Institute of Meteorology, FU Berlin. For night-time a simple threshold was applied to remove the affected pixels. In the final LSE maps, all cloudy pixels (day and night) are discarded because the LSEs are derived from a combination of day and night data. The cloud-detection could be improved using more elaborate techniques; however, this was not the primary focus of the present work. But, it is worth mentioning that a more rigorous scheme, *e.g.* AVHRR Processing scheme Over cLOUDs, Land and Ocean (APOLLO) could be applied to the final LSE maps in order to increase reliability. Figure 17 shows a cloudmask over the study area for a given date.

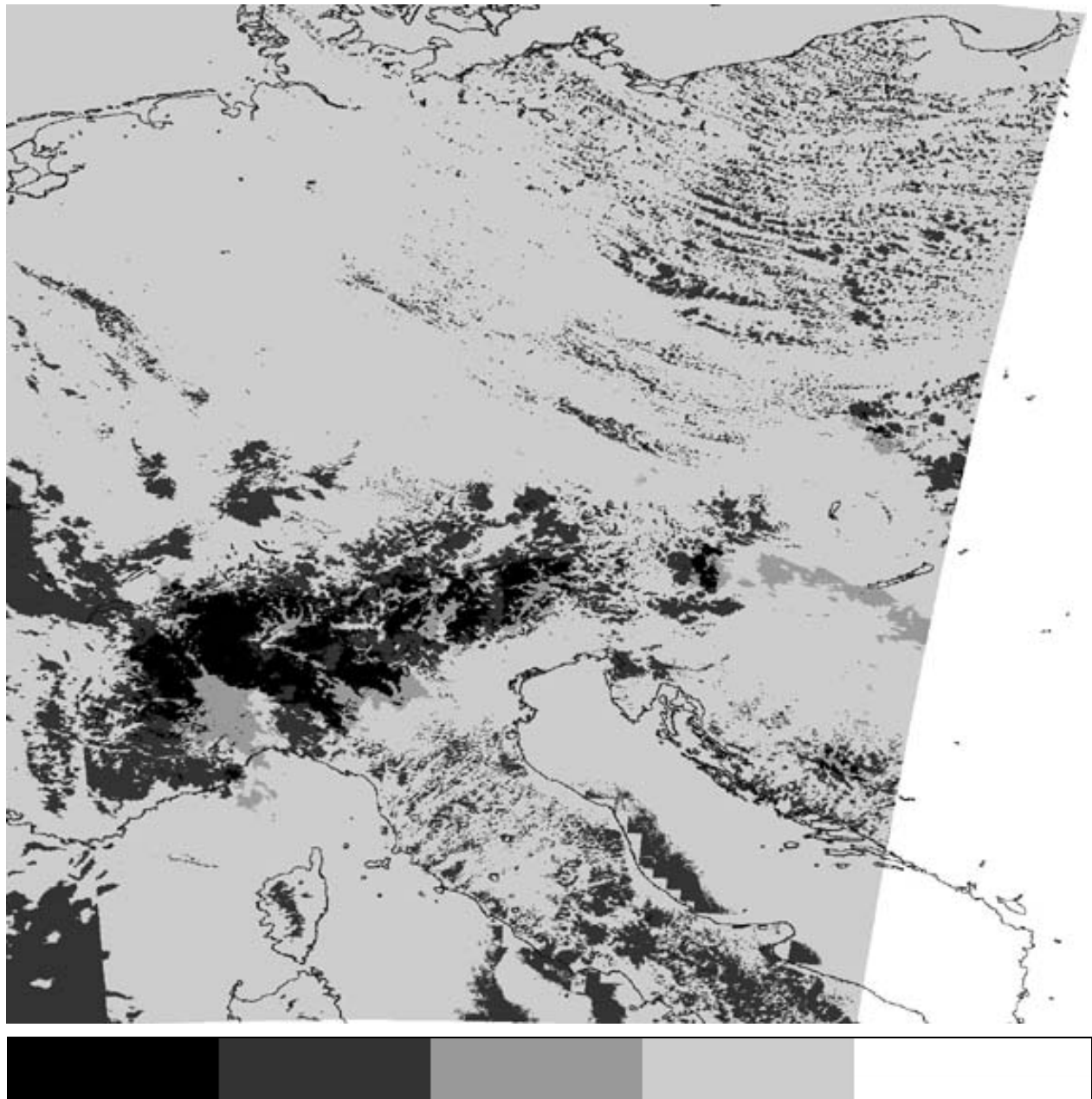


Figure 17: Cloudmask over the study area for 20.08.1996. The daytime cloudmask is provided by Institute of Meteorology, FU Berlin, and the night-time cloud detection is based on a visual threshold approach.

6.5 Software and programs used

PCI EASI/PACE version 7.0.0 was used for the visualization of all digital image data, *e.g.* satellite data, LSEs, LSTs *etc.* For the calculation of the parameters of the power law approximation of Planck's function and the construction of temperature to radiance conversion LUTs, 'C' programs were developed. Atmospheric corrections and radiative transfer calculations were performed with MODTRAN 3.7; the job-cards, which serve as an input to MODTRAN, were produced interactively with a locally developed program in 'FORTRAN'. FORTRAN

codes were also developed for the binary search on LUTs, the extraction of zenith angles from AVHRR zenith angle files for corresponding ECMWF locations, the conversion of BT (brightness temperature) images to radiance images, for the 2-channel TISI used in calculation of LSEs in $W1$ range (3-4 μm), the calculation of LSEs in $W2$ range (10-12 μm) using TISIEs, and the LST extraction. The programs were designed to fit into an operational environment for the processing of long-term data sets. Programs in 'EASI script' were used to create images in JPEG (Joint Photographic Experts Group) format (also called as JPG format). The derivation of the LSTs and LSEs for a single day requires about 100 executions of about 20 different programs. All these codes are operated and controlled by parameter files: UNIX scripts were designed, which create the corresponding parameter files and invoke the programs for the given range of day, or month, or year. The whole system is semi-automatic to automatic; it can be controlled and executed interactively or the executions can be performed automatically for a chosen time-period, provided that the input data files are at the correct locations and conform to the naming system.

6.6 Application to the area of interest

Efforts are made to process the archived data from 1996-present; as an example, a relatively cloud-free day was selected from the so-called golden-days (19-21 August) in 1996, and the TISIE procedures shown in Figure 12 were employed. Figure 18, Figure 19, and Figure 20 show absolute angular LSE for channel-3, 4, and 5 respectively and Figure 21 and Figure 22 give LST at 0200 hrs UTC and 1400 hrs UTC over the study area at the 20. August 1996. Being determined from space radiometry, LSE and LST are dependent on satellite zenith angles for day and for night, and on solar zenith angles; these are shown in Figure 23, Figure 24, and Figure 25 respectively.

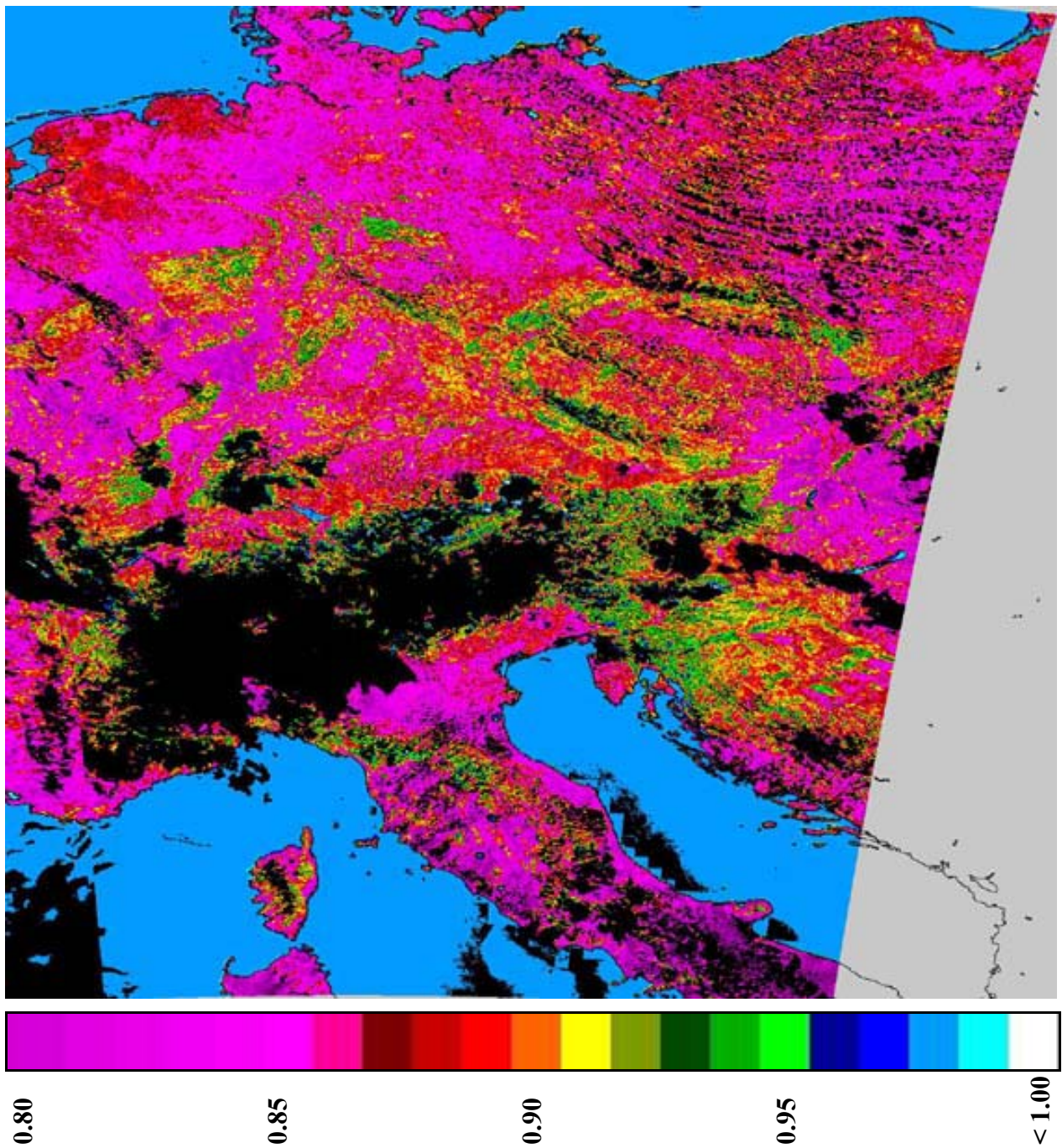


Figure 18: AVHRR channel 3 land surface emissivities over Europe (20.08.1996). The black pixels in the image represent areas covered by clouds. The gray area on the right hand side of the image are missing data. The emissivity of the sea surface was set to 0.975 (NOAA-14 AVHRR channel 3 emissivity value from Table 2). [upper-left: 55° N-5° E lower-right: 40°30'11.6" N-20°21'09.4" E]

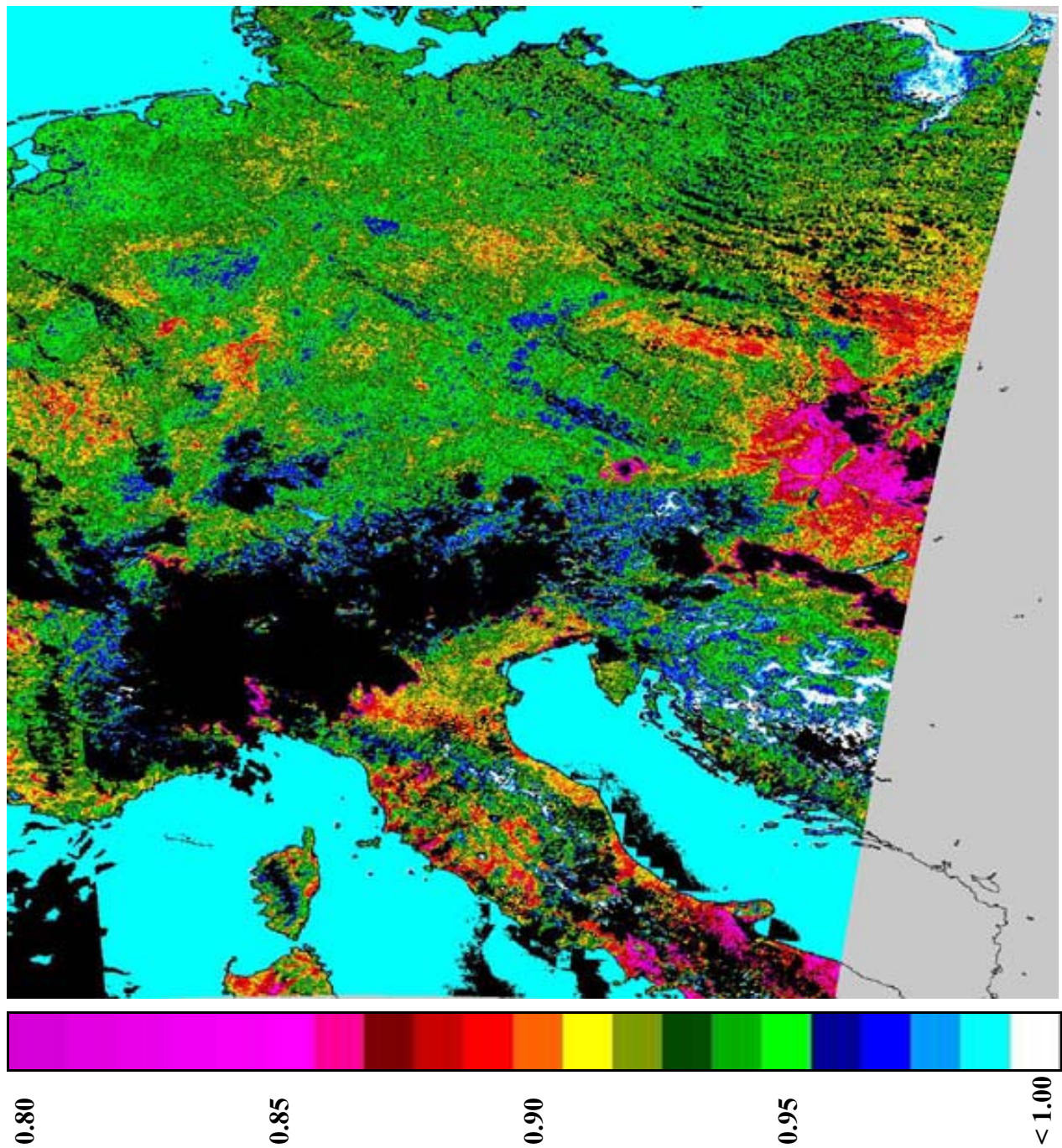


Figure 19: AVHRR channel 4 land surface emissivities over Europe (20.08.1996). The black pixels in the image represent areas covered by clouds. The gray area on the right hand side of the images are missing data. The emissivity of the sea surface was set to 0.990 (NOAA-14 AVHRR channel 4 emissivity value from Table 2). [upper-left: 55° N-5° E lower-right: 40°30'11.6" N-20°21'09.4" E]

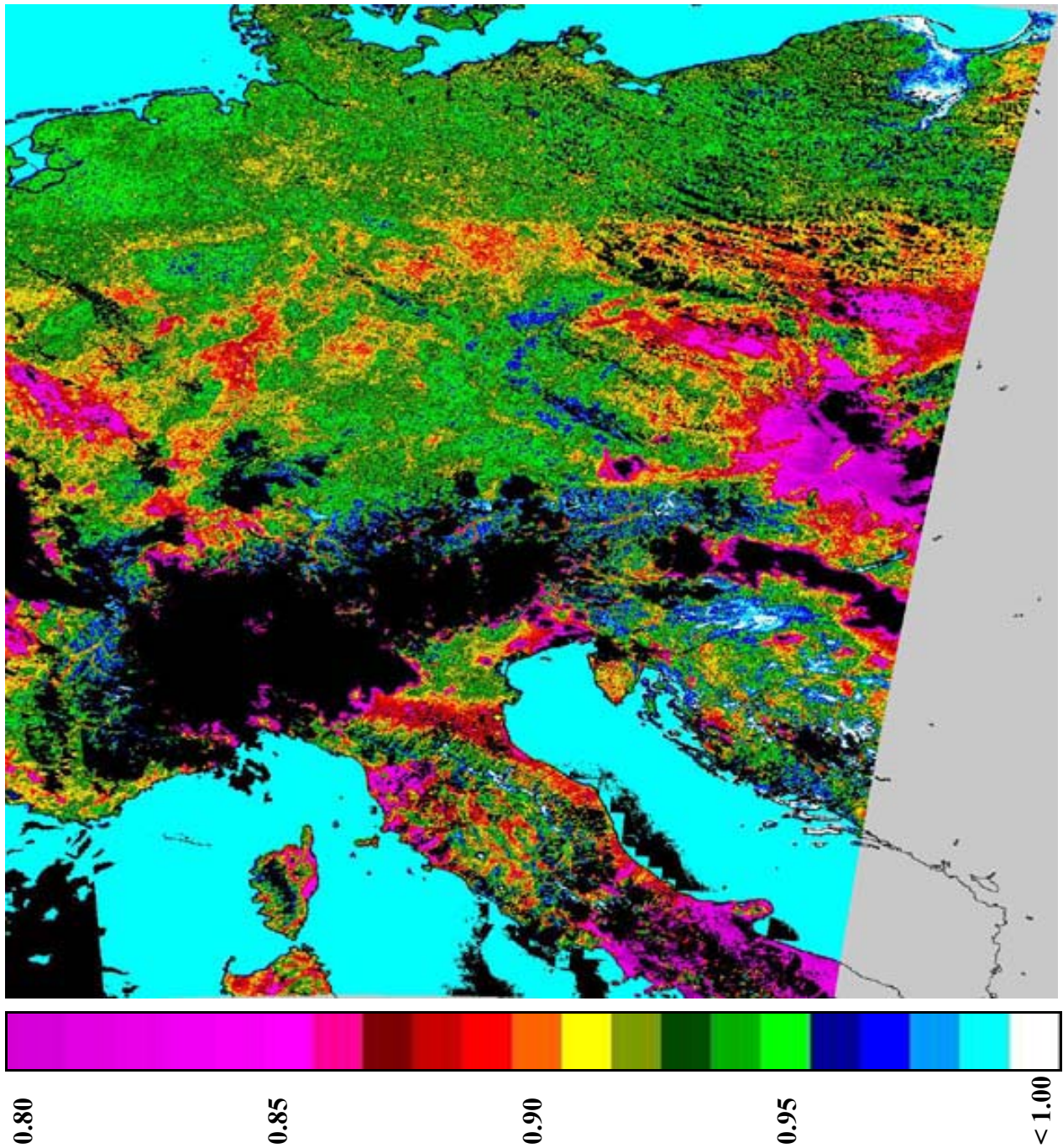


Figure 20: AVHRR channel 5 land surface emissivities over Europe (20.08.1996). The black pixels in the image represent areas covered by clouds. The gray areas on the right hand side of the image are missing data. The emissivity of the sea surface was set to 0.986 (NOAA-14 AVHRR channel 5 emissivity value from Table 2). [upper-left: 55° N-5° E lower-right: 40°30'11.6" N-20°21'09.4" E]

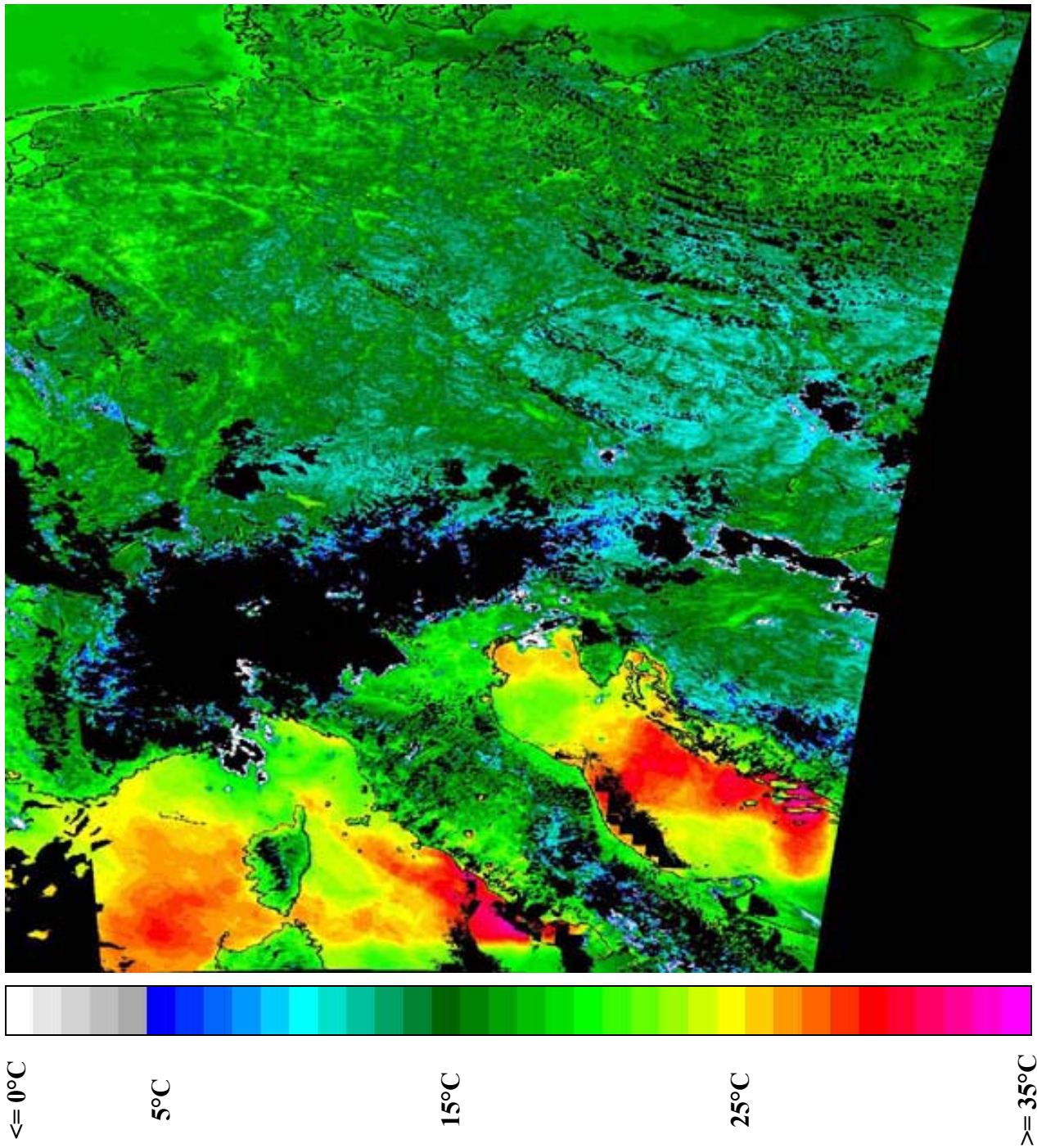
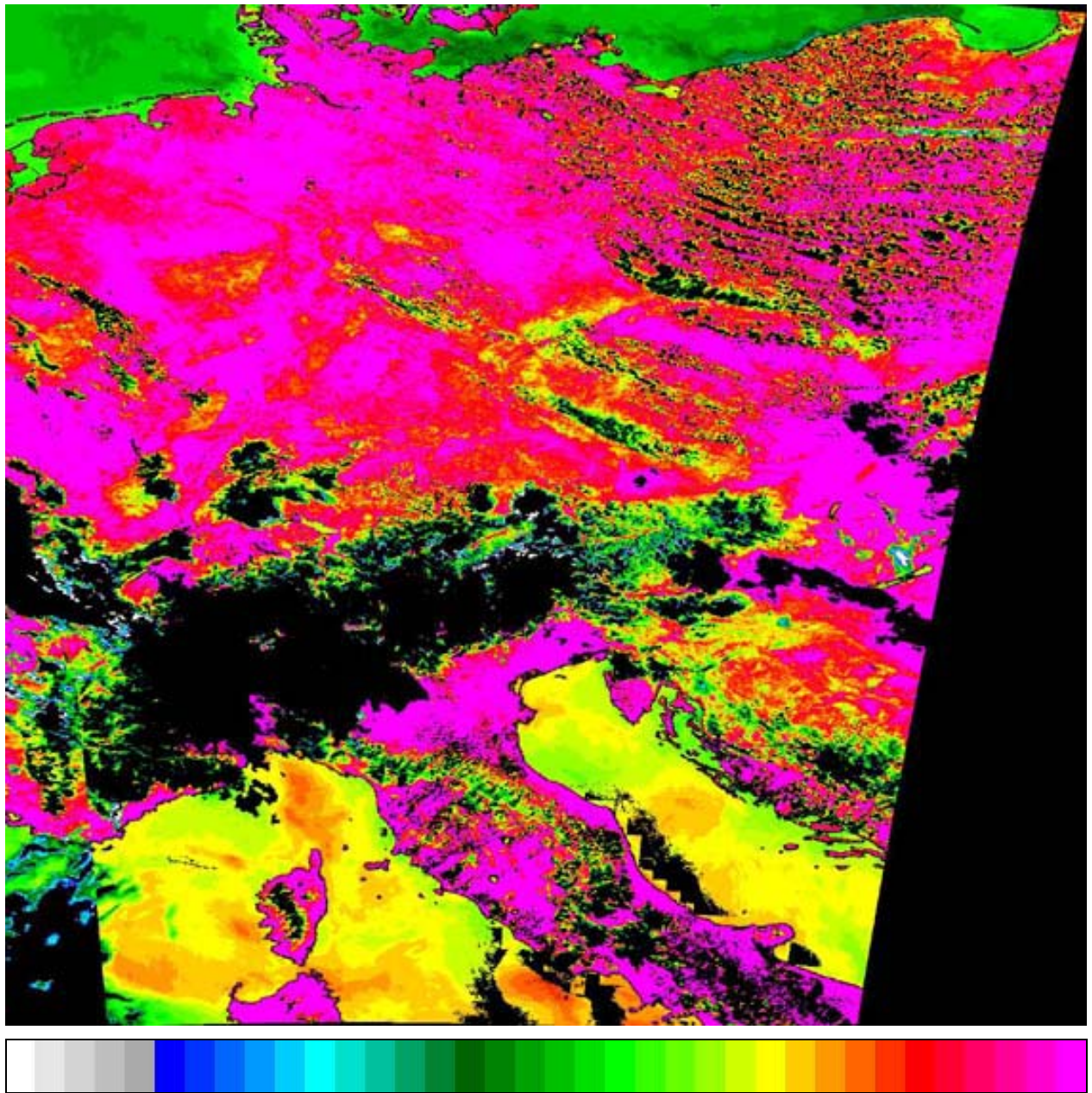


Figure 21: LST map over the study area for 0200 hrs UTC (20.08.1996). The black pixels in the image represent areas covered by clouds or missing data data. [upper-left: 55° N-5° E lower-right: 40°30'11.6" N-20°21'09.4" E]



$\leq 0^{\circ}\text{C}$

5°C

15°C

25°C

$\geq 35^{\circ}\text{C}$

Figure 22: LST map over the study area for 1400 hrs UTC (20.08.1996). The black pixels in the image represent areas covered by clouds or missing data. [upper-left: 55°N - 5°E lower-right: $40^{\circ}30'11.6''\text{N}$ - $20^{\circ}21'09.4''\text{E}$]

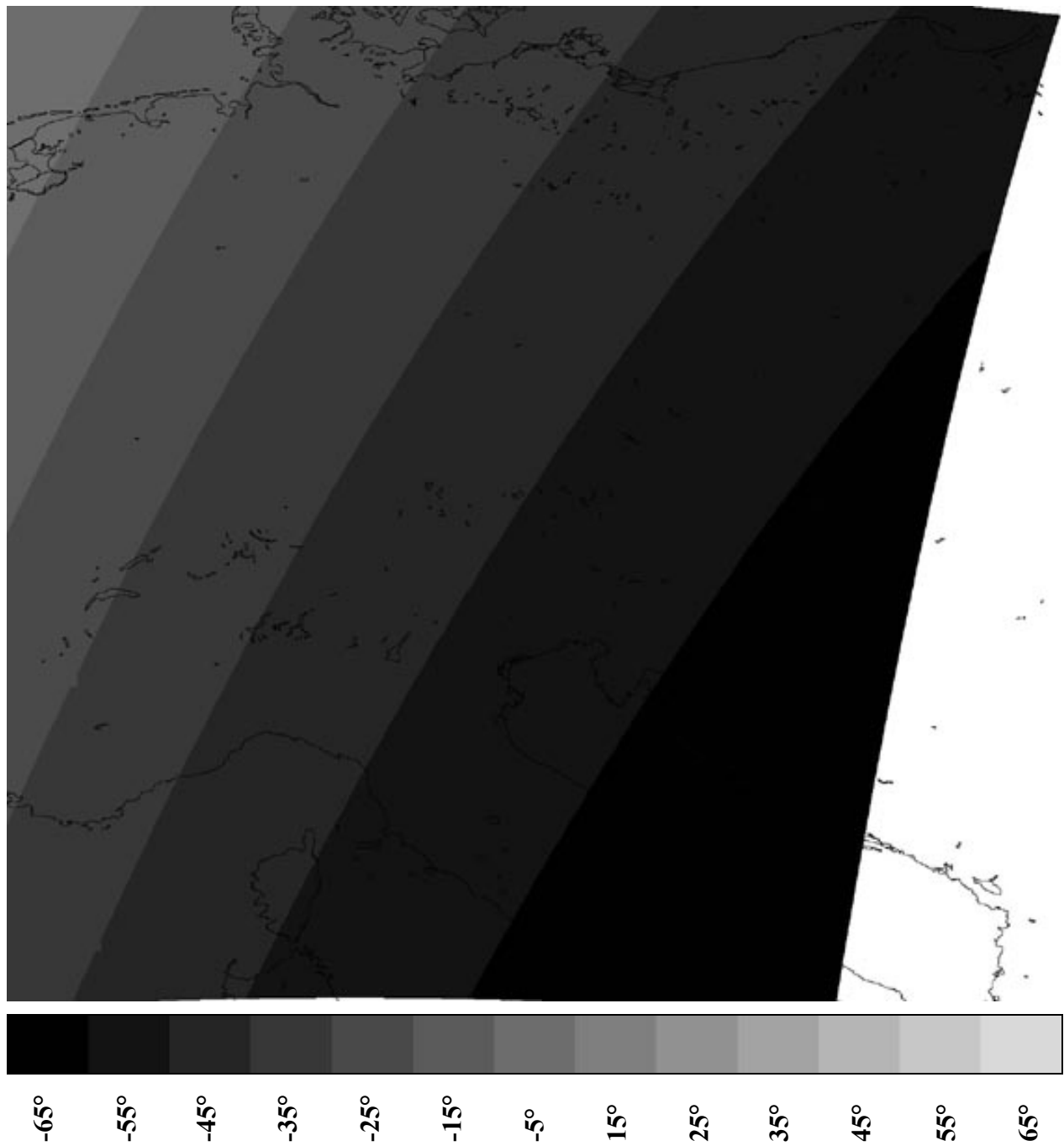


Figure 23: NOAA-14 satellite zenith angles (in degrees) over the study area for 0200 hrs UTC (20.08.1996). The white pixels on the right hand side of the image are areas of no coverage. [upper-left: 55° N–5° E lower-right: 40°30'11.6" N–20°21'09.4" E]

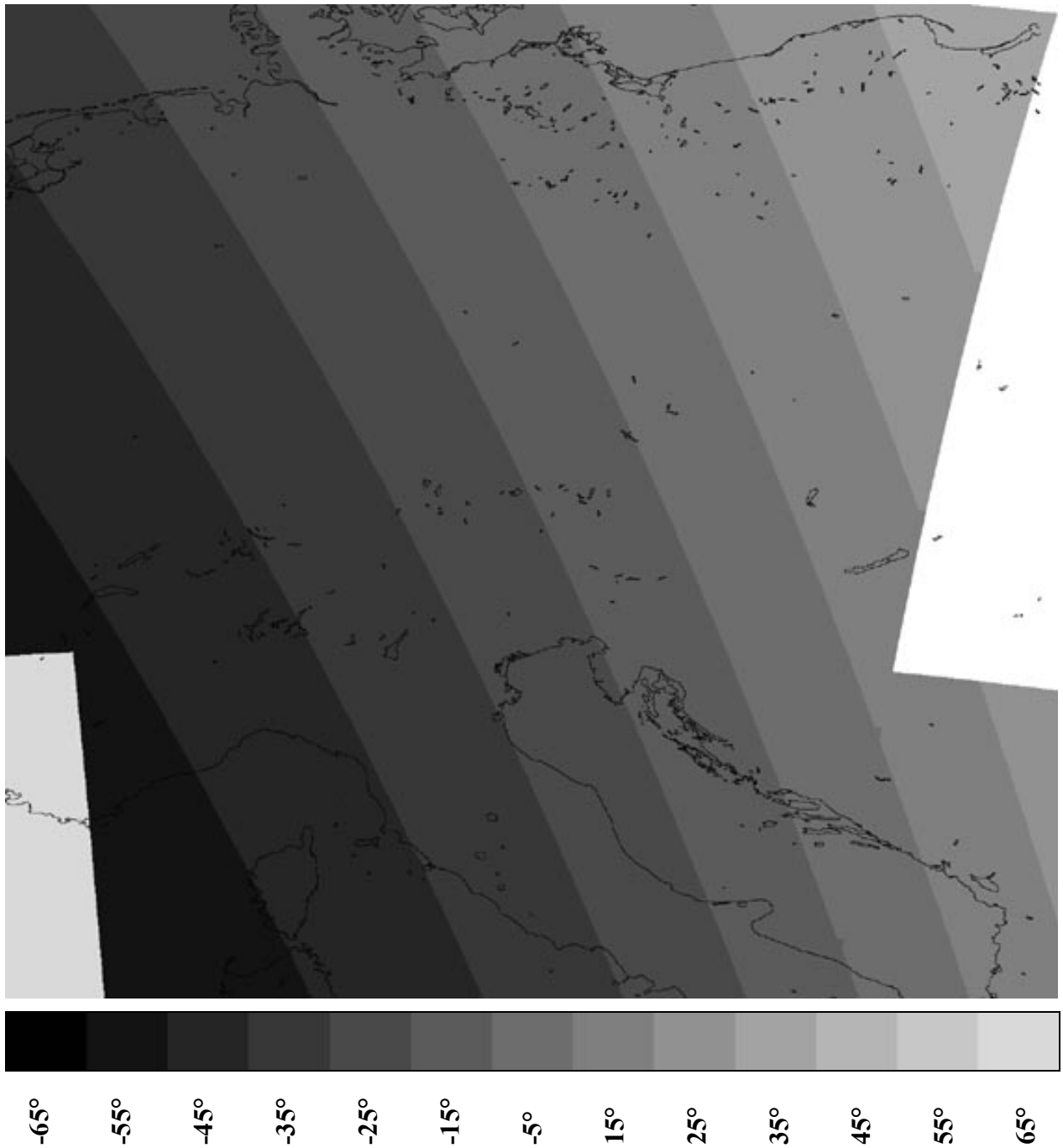


Figure 24: NOAA-14 satellite zenith angles (in degrees) over the study area for 1400 hrs UTC (20.08.1996). The white pixels on the right hand side of the image are areas of no coverage. [upper-left: 55° N-5° E lower-right: 40°30'11.6" N-20°21'09.4" E]

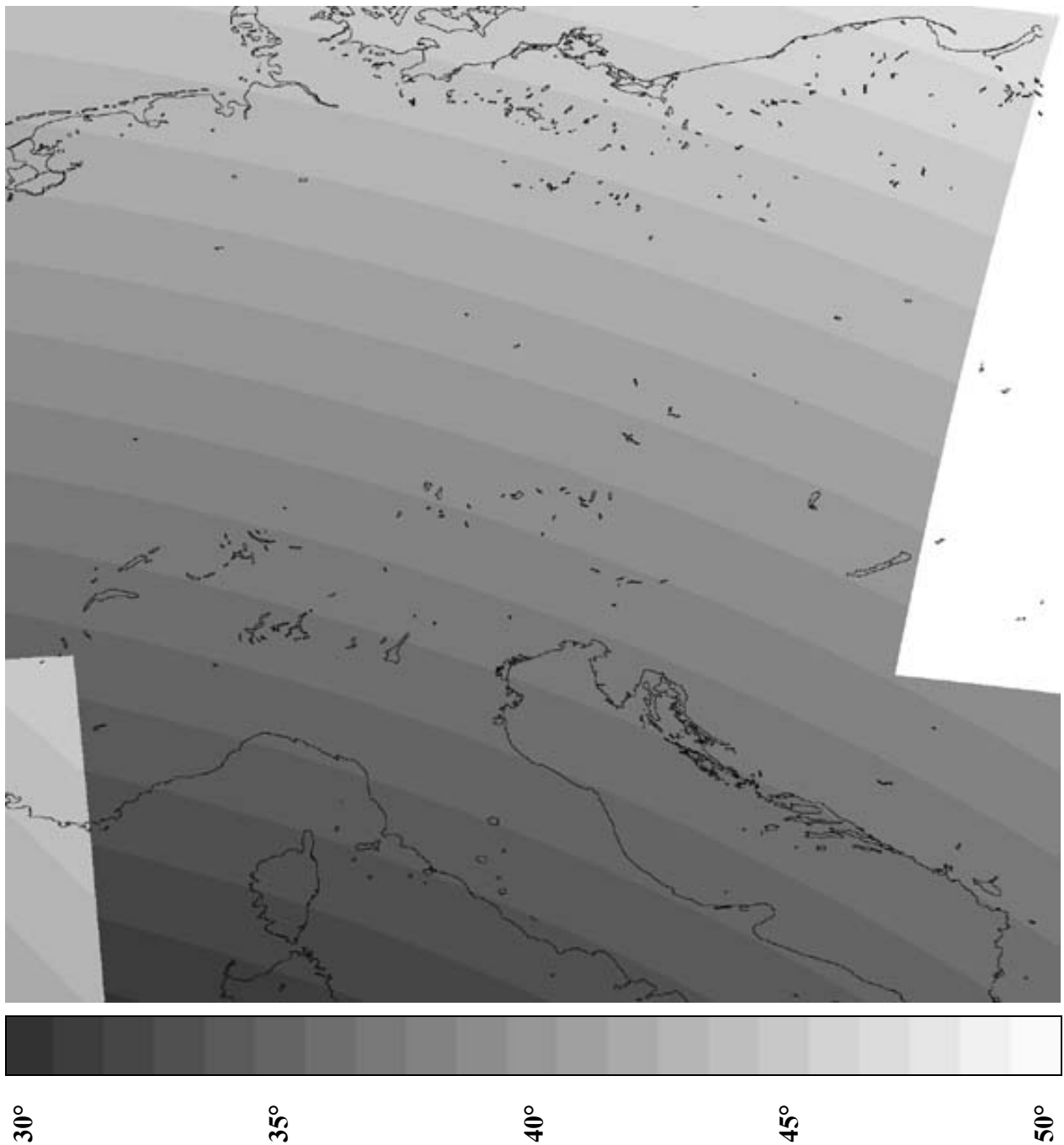


Figure 25: Sun zenith angles (in degrees) over the study area for 1400 hrs UTC (20.08.1996). The white pixels on the right hand side of the image are areas of no coverage. [upper-left: 55° N–5° E lower-right: 40°30'11.6" N–20°21'09.4" E]

For comparison purposes, LSTs for daytime were also derived from channel-5 radiances at surface level using an assumed emissivity of 0.975. Figure 26 shows the LST-differences between LST obtained with LSE from TISIE and LST obtained with the assumed LSE (land surface emissivity).

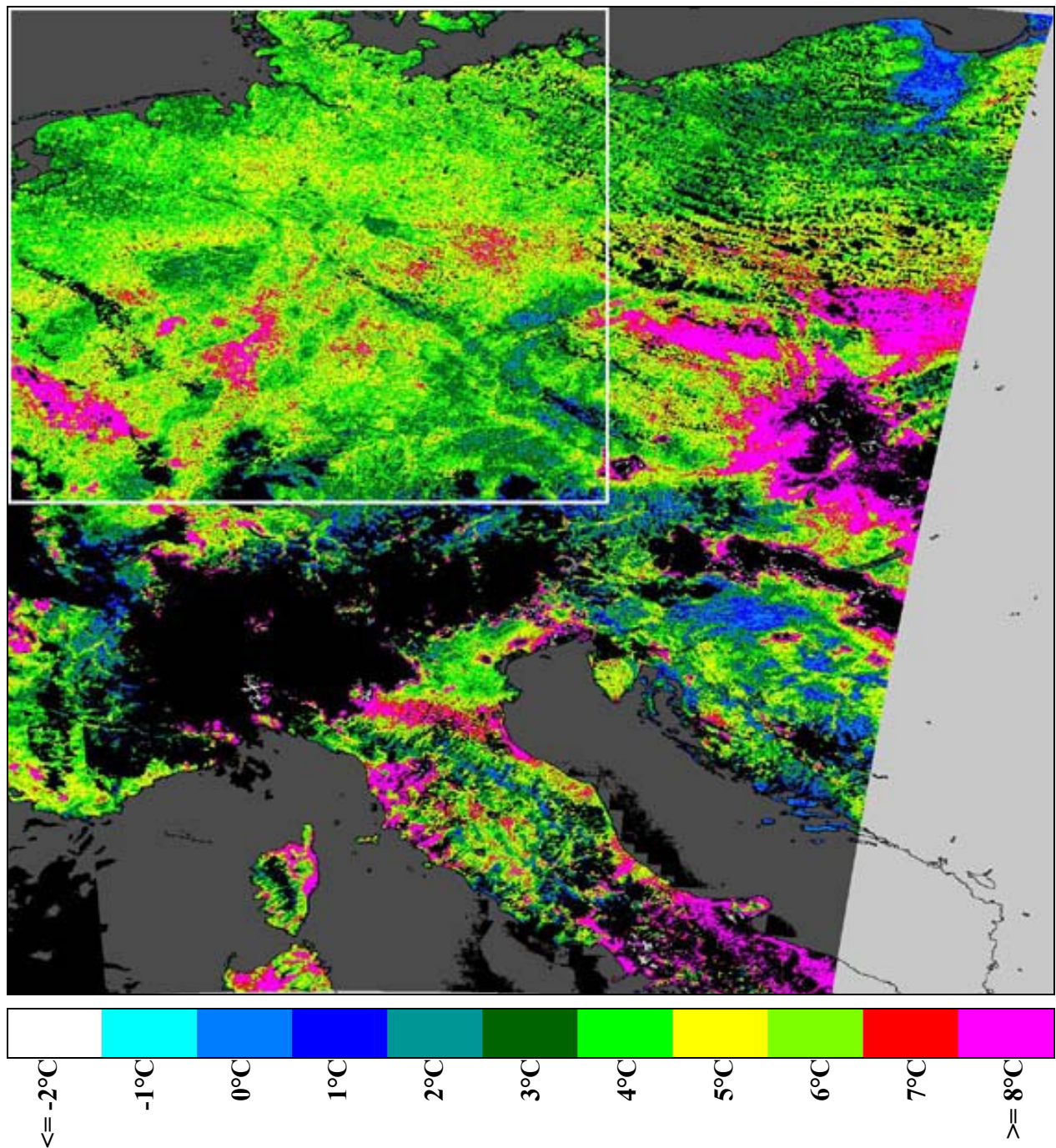


Figure 26: LST difference map for 1400 hrs UTC (20.08.1996). The black pixels represent areas covered by clouds, the light-gray color represents missing data, and the dark-gray pixels represent sea surface and other water bodies. [upper-left: 55°N – 5°E lower-right: $40^{\circ}30'11.6''\text{N}$ – $20^{\circ}21'09.4''\text{E}$]

Surface emissivity in channel 3 has a wide range with values from 0.7 to 0.97 with a histogram peak at around 0.88. Channel-4 LSEs range from 0.88 to 0.99 with a histogram peak at about 0.94. Channel-5 LSEs show a similar trend to channel-4 and range from 0.86 to 0.99 with the histogram maximum at about 0.938. Channel-3 LSEs are essentially daytime emissivities, which are assumed to be the same (constant) at night-time. LSE decreases with increasing zenith angles, except for highly vegetated areas, where angular dependency is smaller. However, for sensors onboard polar-orbiters, zenith angles substantially vary between day and night (Figure 23 and Figure 24) and channel-3 angular (θ_{day}) LSE is used to obtain angular emissivities (θ_{night}) for the other channels using night-time ratios. Despite the relative stability of the TISIE used in equation (33) this causes a discrepancy and is pronounced for stronger variations of zenith angle. The effect is severe over water, where surface emissivity varies by about 3.3% between nadir and 55° angular observations (Sobrino and Cuenca, 1999). Additionally, the water surface has a stronger specular behavior than land surfaces. Hence, sea surface emissivities are set to sensor-specific values (Table 2). When assuming that the form factor $F_r(\theta, \theta_{sun}, \phi)$ equals 1, the absolute value of zenith angles should ideally be less than 30-40°. Moreover, path-radiance increases with path-length (higher nadir angles) where as total TOA radiance decreases (Figure 7 and Figure 8); channel-5 is more affected by this than channel-4, *i.e.* the effect on LSE will be higher for channel-5 than for channel-4 (characteristics in $W2$). LSE is estimated using a relation involving radiances in the form of TISIE. Figure 24 (daytime zenith angle over the study area) shows a variation of about -50° to 34° (bottom-left to top-right). The night-time zenith angle over the study area (Figure 23) varies from about 3° to -65° (top-left to bottom-right).

For the higher zenith angles the error in emissivity increases; this is related to the error made by assuming a form factor of 1. This problem can be overcome by modelling the form factor using a time series of LSE data for different view angles (Petitcolin, Nerry, and Stoll, 2002a). However, over this time period it should be ensured that LSE does not change except for changing view angles, *i.e.* LSE should not change due to micro-meteorological conditions, which is difficult to ensure. Additionally, the clouds at different dates will cover different areas. Therefore, form factor characterization, even though in principle achievable, is often not suitable; this was also the case in the present study. Another possibility would be to use data with only near-nadir measurements, *e.g.* from geo-stationary satellite sensors like MSG SEVIRI (Dash, Göttsche, and Olesen, 2002b; 2003).

In general, the forest covered areas (Figure 16) have high LSEs: channel-3 from 0.91 to 0.97, channel-4 from 0.95 to 0.98, and channel-5 has values similar to those of channel-4. The woodlands, wooded grasslands, and shrublands have lower LSEs than the forest covered areas: channel-3 from 0.89 to 0.94, and channel-4 and channel-5 from 0.91 to 0.96. The croplands and grasslands have similar values ranging from 0.89 to 0.93 for channel-3, and 0.90 to 0.96 for channels 4, with LSEs in channel 5 being generally slightly higher than for channel-4. The urban areas have LSEs from 0.89 to 0.93 for channel 4, 0.90-0.93 for channel 5, and 0.85 to less than 0.80 for channel 3. Even though a field validation is required to check the accuracy and reliability of the method, the preliminary results are in good agreement with the UMD land cover type map, with the largest differences occurring for agricultural areas, which are subject to cultivation and harvesting.

Surface temperature mostly shows an inverse relation with emissivity, *i.e.* for areas with high emissivities, surface temperatures are relatively low. For extracting LST from surface radiances, channel 5 LSE is used. For the sea surface, temperatures are derived using a fixed emissivity of 0.986 in channel 5; however, complete atmospheric correction was performed, *i.e.* the upwelling radiance was removed and surface radiances were decoupled in order to remove the effect of reflected downwelling radiance. LST shows a strong variability from about 5°C (for some areas during night) to more than 35°C (for some areas during day), while SST covers a range between 15°C and 28°C, where the Mediterranean Sea remains warmer than the North Sea and the Baltics. The sea surface is usually slightly warmer in day than night except for few areas, *e.g.*

coasts in the Adriatic Sea and the Mediterranean about 100 km west of "Strait of Bonifacio" in the south of Corsica islands. However, there is only little diurnal variation of SST (usually around 2°C to 3°C and less than 5°C near the coast towards west of the Appennines). In contrast, LST generally varies by about 10°C to 20°C. High mountains show low temperatures during day and night and are usually influenced by clouds; hence, these data are discarded. The LST difference map (Figure 26) shows the difference in LST obtained with TISIE derived emissivity and with an assumed LSE of 0.975. The difference is mostly about 3°C to 4°C, but reaches up to 8°C for areas with very low LSEs, *i.e.* area towards the right in Figure 26. For the sea surface, no differences are shown because the same emissivity was assumed. The figure gives an estimate of the error that is introduced by assuming a fixed emissivity; however, it should be noted that the error directly depends on the assumed emissivity and the actual emissivity of a pixel.

For a closer comparison, the part of the data indicated by the white line in Figure 26), which roughly covers Germany, was selected. The data in that area has an acceptable range of zenith angles (0°-40°), except for a small section at the bottom-left, where zenith angles for the daypass are up to 40°. Figure 27, Figure 28, and Figure 29 show AVHRR channels 3, 4, and 5 LSEs, respectively. In the selected area there is a variety of land cover types including vegetated forests, urban areas, croplands, sand, and marshy lands. In order to allow comparisons with some other surface parameters, Figure 30 shows the NDVI (normalized difference vegetation index) and Figure 31 shows the land cover type.

LST for 0200 hrs UTC and 1400 hrs UTC is shown in Figure 32 and Figure 33, respectively (20.08.1996). As the zenith angle and the elevation have a significant influence on LSE, satellite and solar zenith angles are also shown (Figure 34, Figure 35, and Figure 36) and elevation is given in Figure 37. For better orientation, some of the better known areas are annotated in Figure 31. The forest-covered mountainous areas are location-1 (Black Forest), location-4 (Vogesen Mountains), location-5 (Schwäbische Alb), and location-12 (Harz Mountains). Further areas covered by vegetation are location-2 (pre-dominantly vineyards), location-3 (Palatinate Forest), locations-6 and 7 (Odenwald or forest), location-10 (Mittelgebirge), location-12 (Thüringer Wald or forest). Location-9 (Kraichgau) is a pre-dominantly agricultural area with smaller patches of forest. Location-8 is the city of Frankfurt am Main, location-14 is the area around Berlin-Brandenburg, and location-15 marks the city of Hamburg. Location-11 is the so-called "Ruhrgebiet" comprising industrial locations and townships like Dortmund, Essen, Duisburg, and Bochum *etc.* Location-16 is a hilly area (Hügelland), whose geomorphology was shaped by glaciers during the last European iceage. Location-17, which closely follows the coastline, consists mainly of marshy areas.

In general, for all three channels the vegetated areas show higher emissivities than for the other land surface types. The forest areas, *e.g.* Palatinate forest, Vogesen Mountains, Odenwald, Harz Mountains as well as the vineyards show LSEs in the range of 0.91-0.96 (channel-3), a minimum of 0.95 with a most frequent value of approximately 0.98 (channel-4), and similar values for channel-5 with a most frequent value of approximately 0.97. Except for the Harz Mountains, the high LSEs in these areas directly correlate with the high NDVI values of 0.6-0.8. This is explained by the fact that the Harz Mountains are mostly covered by needleleaf forests, whereas the other forest areas have significant amounts of broadleaf trees. For the black forest and large parts of the Thüringer Wald and the Schwäbische Alb, and for a small part of the Vogesen Mountains, LSE estimation was hampered by cloud cover for the particular day / night data. These areas are also high altitude (> ~1.5 km) areas (Figure 37). The vineyards also show high emissivities, which are only slightly less than for the dense forest areas, except for some areas towards the bottom-right. The agricultural areas, *e.g.* Kraichgau, have moderate to low emissivities, which is attributed to the harvesting season: 0.85 to maximum 0.91 (channel-3), and 0.90-0.94 in channels 4, and 5. The urban areas (*e.g.* Berlin, Hamburg, Frankfurt am Main, and Ruhrgebiet) have low emissivities ranging from 0.91-0.2 for channels 4, and 5 with slightly higher values for channel-5 and much lower values for channel-3 (< 0.80).

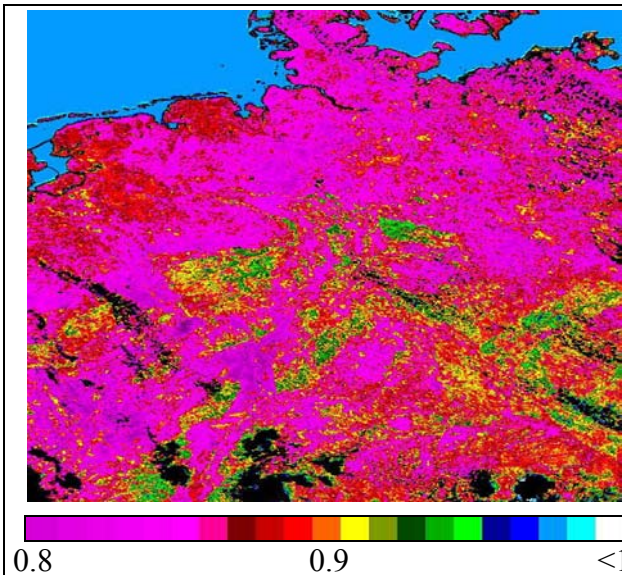


Figure 27: AVHRR channel 3 LSE (20.08.1996).

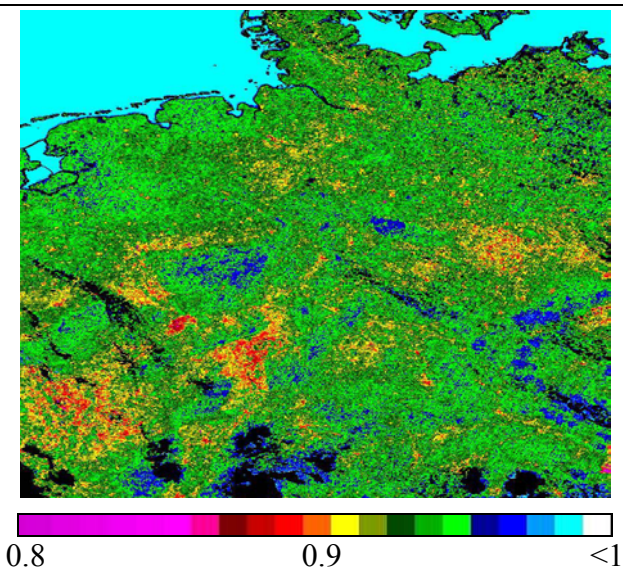


Figure 28: AVHRR channel 4 LSE (20.08.1996).

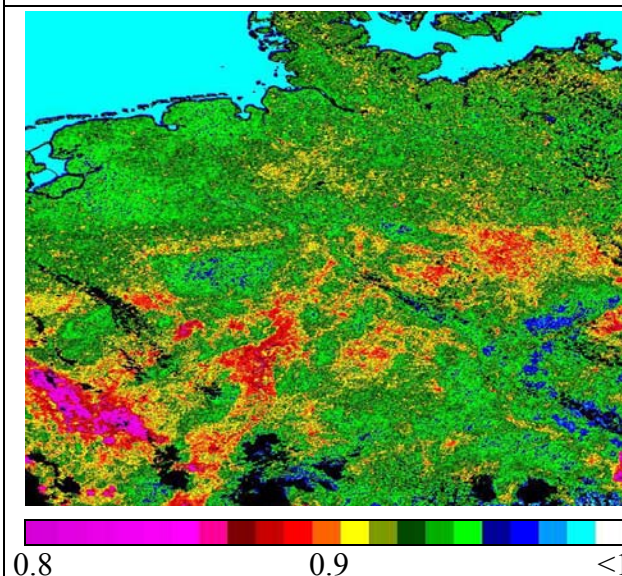


Figure 29: AVHRR channel 5 LSE (20.08.1996).

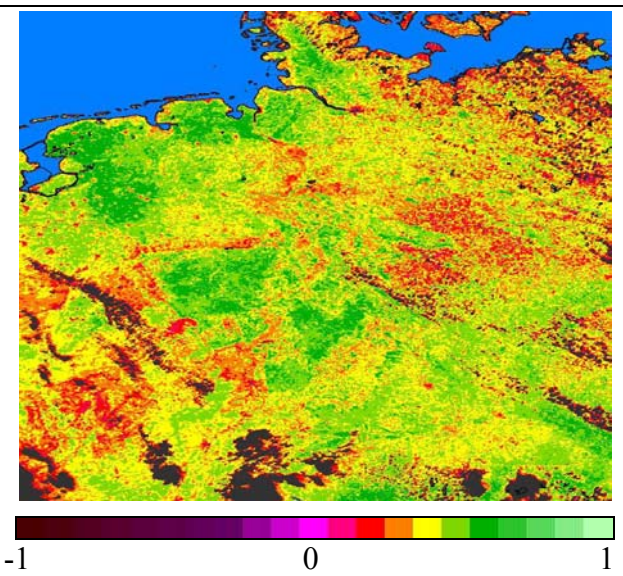


Figure 30: AVHRR NDVI (20.08.1996)

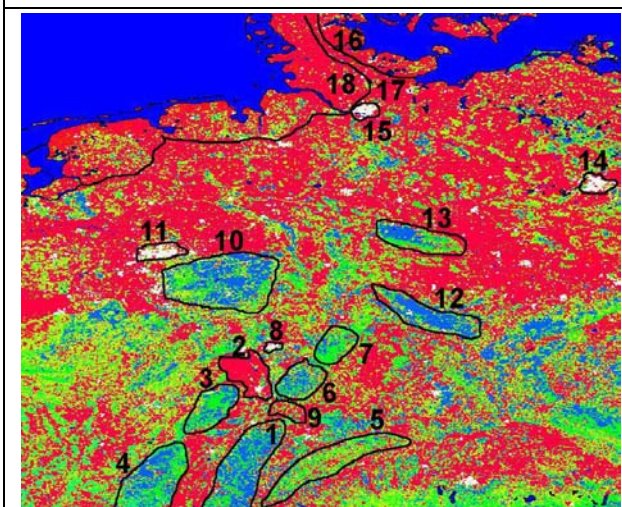


Figure 31: UMD land cover types

<ul style="list-style-type: none"> Water Evergreen needle forest Evergreen broadleaf forest Deciduous needleleaf forest Deciduous broadleaf forest Mixed forest Woodland Wooded grassland Closed shrubland Open shrubland Grassland Cropland Bareground Urban built-up 	<p>Marked areas</p> <ul style="list-style-type: none"> 1. Black forest 2. Vineyard (grapes) 3. Palatinate forest 4. Vogesen Mountains 5. Schwäbische Alb 6. Odenwald (forest) 7. Forest areas 8. Frankfurt main (city) 9. Kraichgau (agriculture) 10. Mittelgebirge 11. Ruhrgebiet (industrial area & cities) 12. Thüringer Wald 13. Harz Mountains 14. Berlin 15. Hamburg 16. Hügelland (by glacier) 17. Sandy areas 18. Marshy areas
--	---



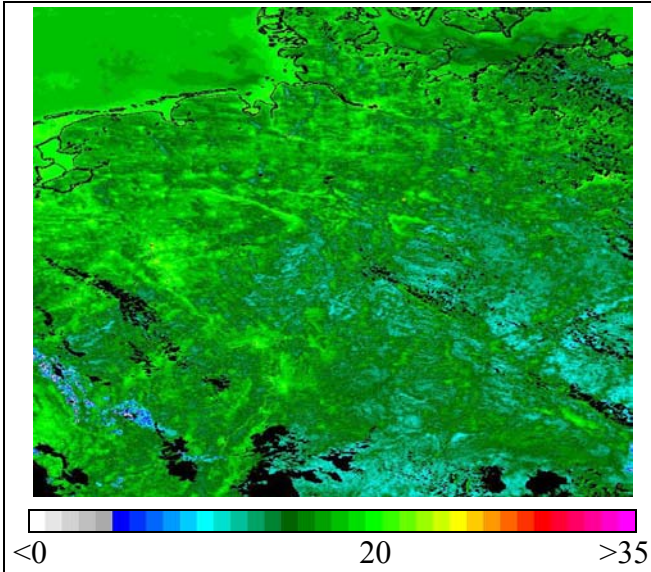


Figure 32: LST in °C for 0200 hrs UTC (20.08.1996).

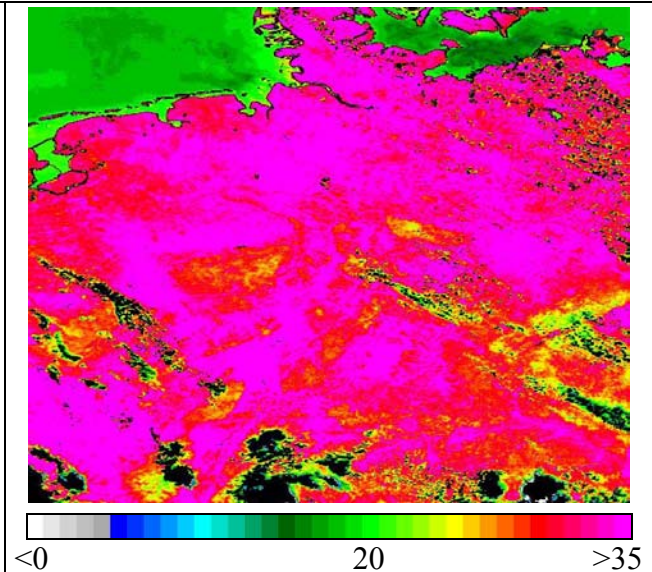


Figure 33: LST in °C for 1400 hrs LST (20.08.1996).

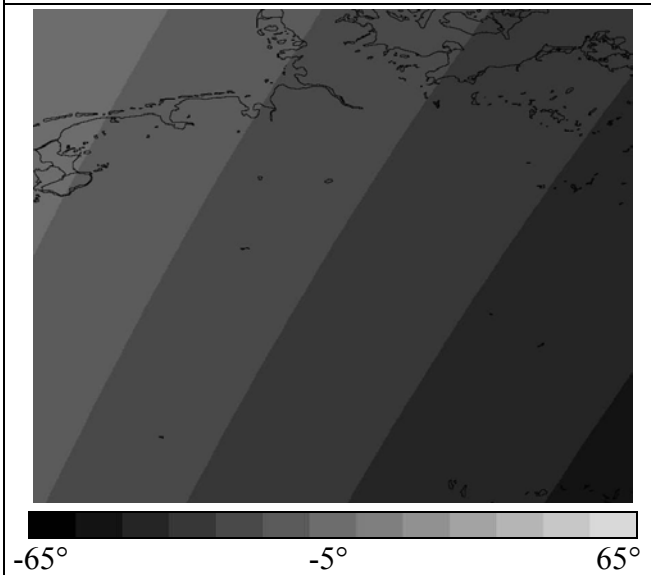


Figure 34: NOAA zenith (20.08.1996 0200 hrs UTC).

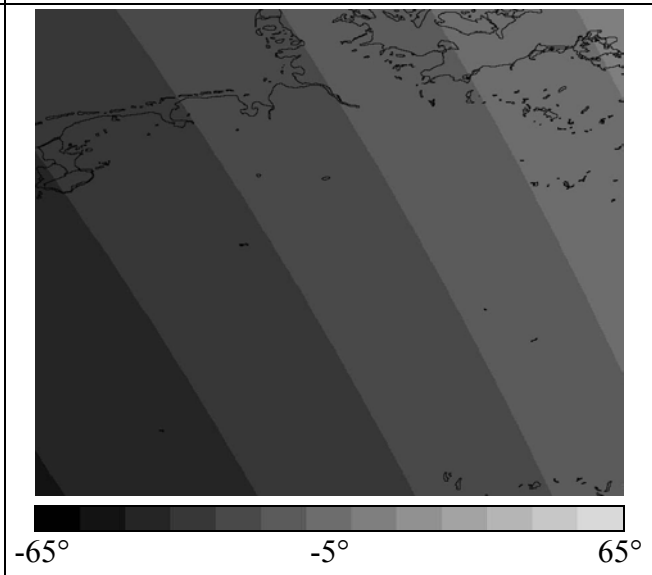


Figure 35: NOAA zenith (20.08.1996 1400 hrs UTC).

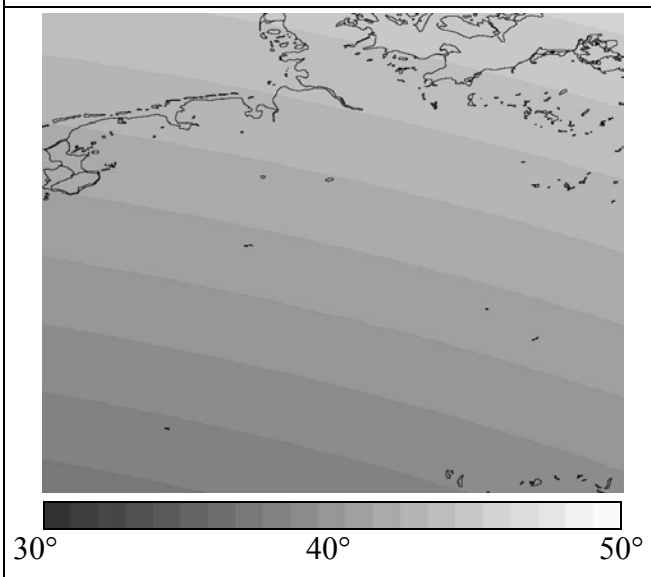


Figure 36: Solar zenith (20.08.1996 1400 hrs UTC).

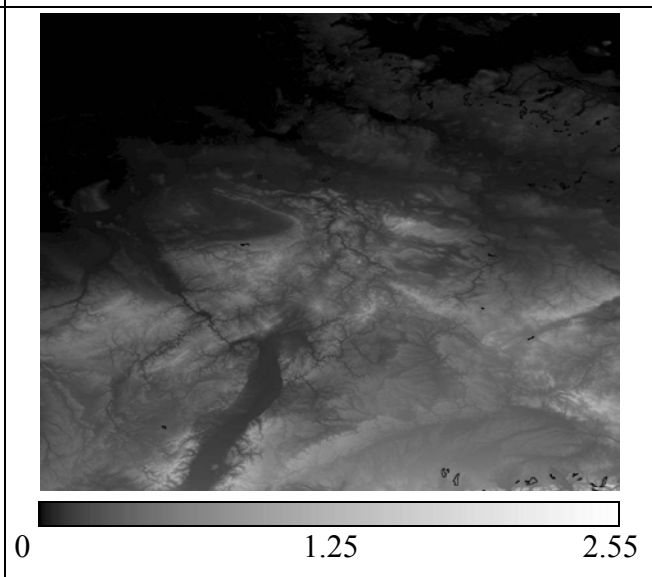


Figure 37: Elevation in km (USGS GTOPO30 DEM).

The sea behaves like a heat-buffer with a nearly constant temperature of about $20\pm 3^{\circ}\text{C}$. Over land, LST varies more (10 - 20°C difference between night and day). LST distribution also depends on altitude, *i.e.* as altitude increases, LST decreases (Figure 37 vs. Figure 32, and Figure 33). During daytime, LST variation is clearly related to NDVI; highly vegetated areas are cooler than surrounding areas with little vegetation. The high-altitude areas have LSTs from 14°C to a maximum of up to 28°C - 30°C , whereas during daytime LSTs for lower areas can reach as high as 42°C with peak of abundance at around 25°C . At night, there is little spatial variation of LST and a direct dependence on elevation can be observed. However, urban areas have a temperature range of 26°C to 28°C , and for other areas (low elevations) LST ranges from 16°C to 21°C at most, with values usually lying around 15°C .

In order to demonstrate the effects due to seasonal changes, data for the 15.04.1996 are shown in Figure 26, which cover the same area. Figure 38, Figure 39, and Figure 40 show the corresponding emissivities for AVHRR channels 3, 4, and 5, respectively (15.04.1996). The black-pixels are areas covered with clouds, which was more for 15.04.1996 in comparison to the data from 20.08.1996. Figure 41 gives the NDVI values over the study area. LST for 0200 hrs UTC and 1400 hrs UTC are given in Figure 42 and Figure 43 respectively.

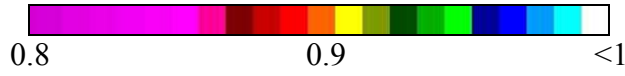
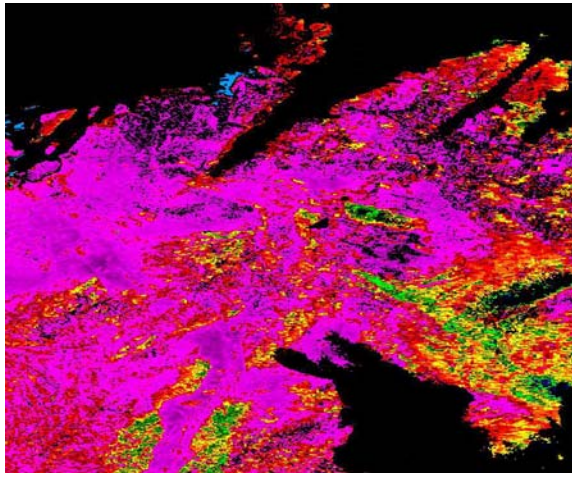


Figure 38: AVHRR channel 3 LSE (15.04.1996).

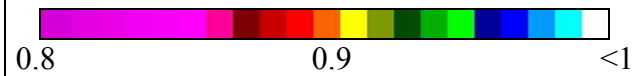
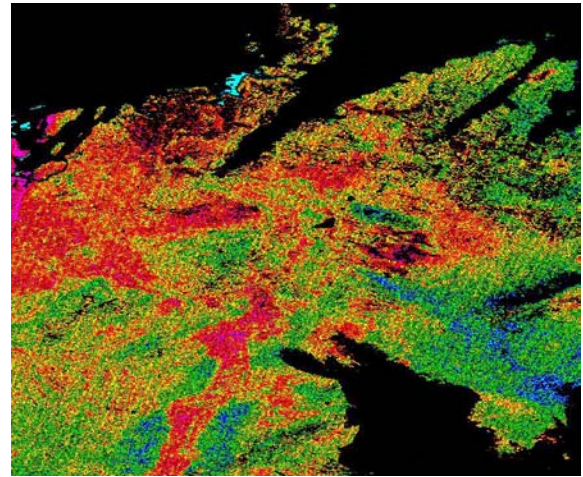


Figure 39: AVHRR channel 4 LSE (15.04.1996).

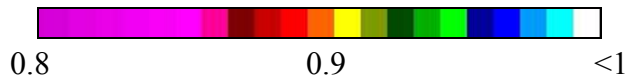
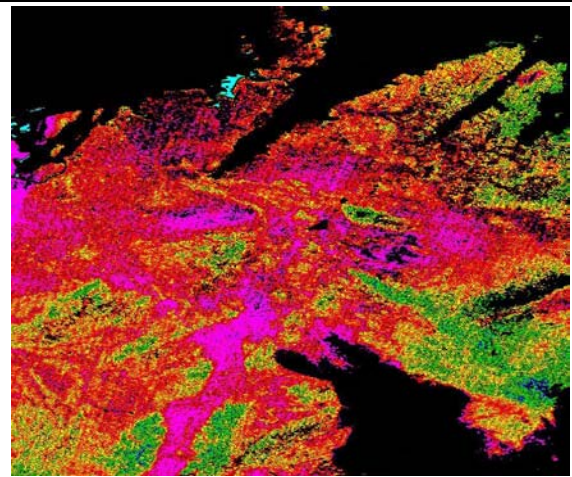


Figure 40: AVHRR channel 5 LSE (15.04.1996).

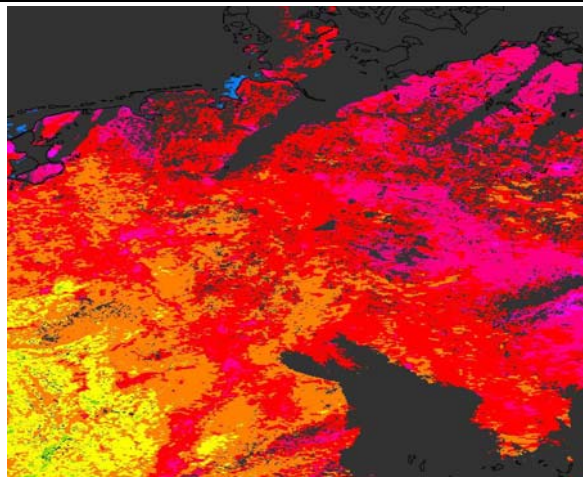


Figure 41: AVHRR NDVI (15.04.1996).

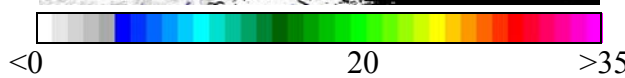
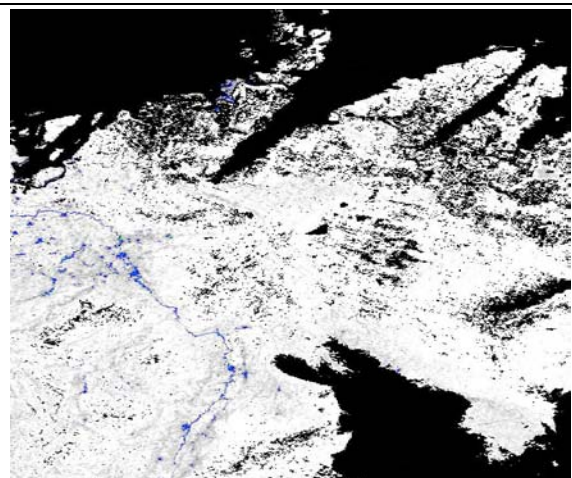


Figure 42: LST in °C for 0200 hrs UTC (15.04.1996).

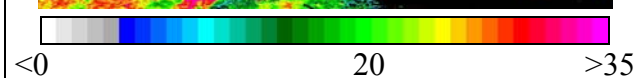
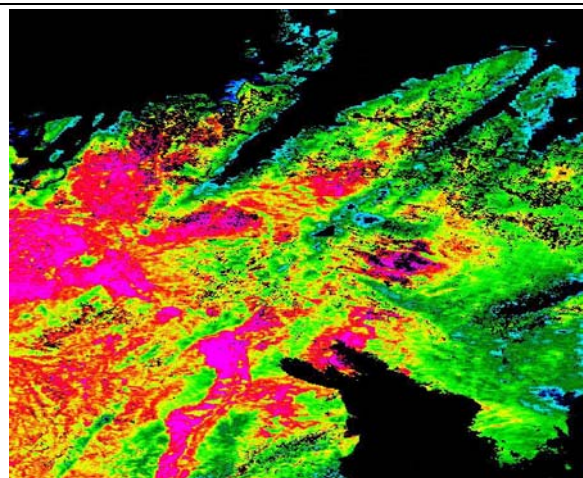


Figure 43: LST in °C for 1400 hrs UTC (15.04.1996).

Over bare-soils and arid areas, measurements made at different times of the year are comparable; however, this is not the case for croplands and vegetated areas, where seasonal changes are more prominent. Following winter, the observed area has less vegetation in April than in August; this is reflected in lower values of NDVI and lower emissivities. For the marshy areas (location-18) and areas just south-west of these, differences in emissivity are quite prominent (considerably lower in April). This also is reflected in the NDVI, which ranges from 0.4 to 0.8 in August and from 0.1 to 0.3 in April. However, for the south-west of the image (covering a part of France), the characteristics are different: this area consists partly of forests and partly of croplands. The forest areas have roughly similar NDVI values for both months, but in contrast to the northern parts, the croplands have higher NDVI values in April than in August. Consequently, the emissivity values are higher in April than in August for this area. This is a result of early cultivation as well as early harvesting and reflects the climatological influence of the Mediterranean on this area, which spreads through the Rhone (river) valley. LST for nighttime (0200 hrs UTC) varies between -4°C and a maximum of $\sim 8^{\circ}\text{C}$, with a most frequent value of $1^{\circ}\text{C} - 0^{\circ}\text{C}$. During daytime (1400 hrs UTC), LST varies between 8°C and 35°C with a most frequent value of approximately 15°C . LST is the skin temperature of the land surface. It is maintained by a balance between the incoming solar and longwave irradiation and the outgoing terrestrial infrared radiation. The daytime air temperature (lowest layer of air temperature from ECMWF profiles corresponding to 2 mts height) was generally low in April (maximum between 18°C and 20°C), however, the LST (at 1400 hrs) was generally be more. This is also reflected by higher TOA brightness temperatures ($22^{\circ}\text{C} - 27^{\circ}\text{C}$ in channel-5) for these locations. The spatial variation of air temperature is relatively small and smooth; in contrast, LST can vary rapidly and doesn't necessarily reflect the distribution of air temperatures: the difference can be higher than 10°C . Figure 44–Figure 49 shows (20.04.1996) channel emissivities (channel 3 and 4), LST (0200 and 1400 hrs UTC), NDVI, and land cover type over a part of Italy.

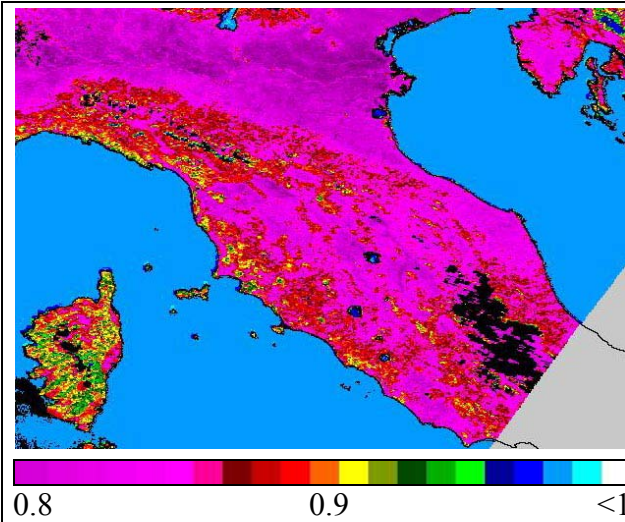


Figure 44: AVHRR channel 3 LSE (20.04.1996).

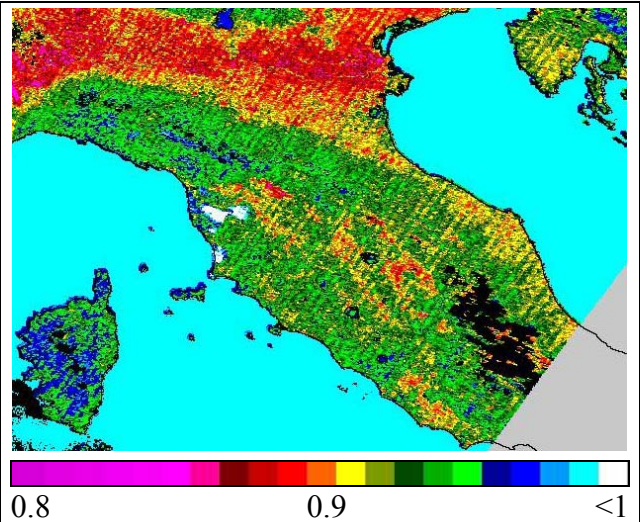


Figure 45: AVHRR channel 4 LSE (20.04.1996).

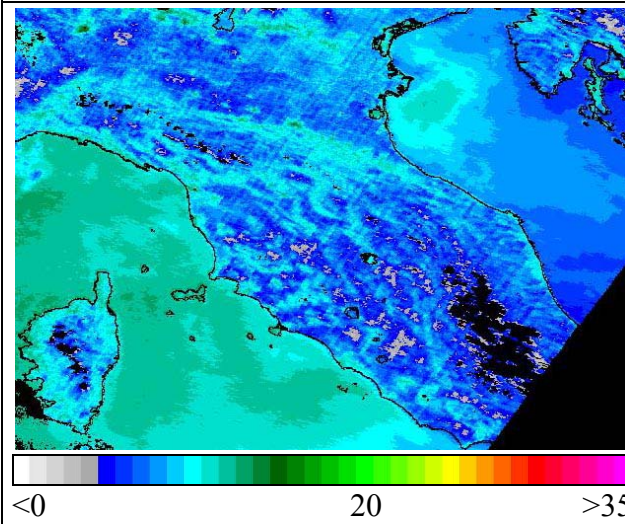


Figure 46: LST in °C for 0200 hrs UTC (20.04.1996).

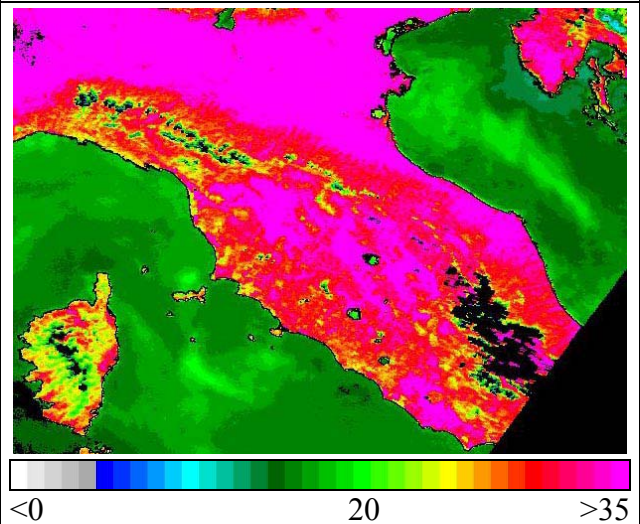


Figure 47: LST in °C for 1400 hrs UTC (20.04.1996).

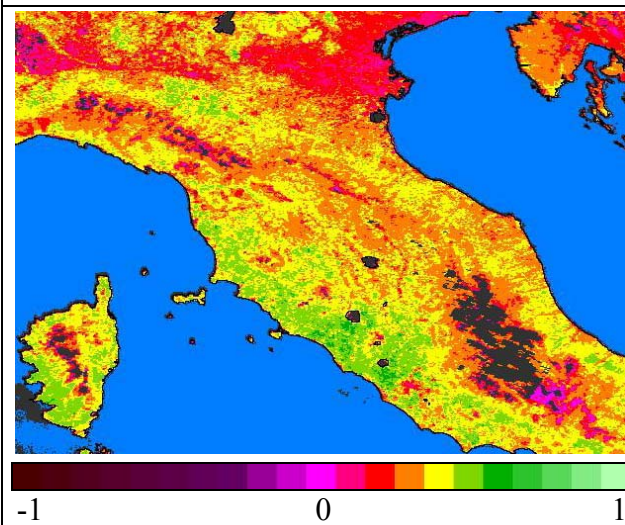
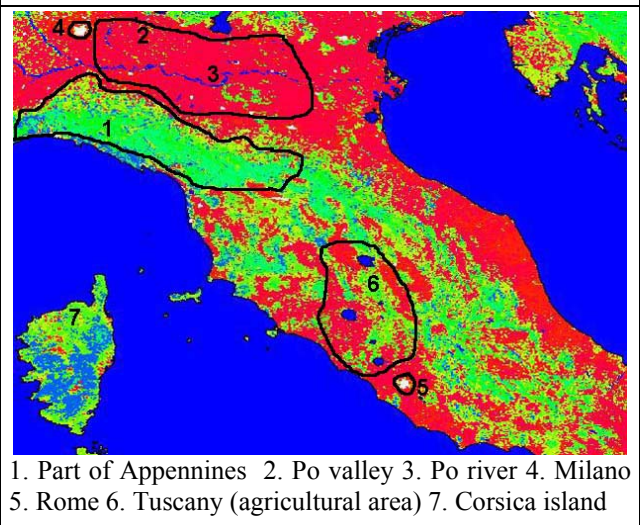


Figure 48: AVHRR NDVI (20.04.1996).



1. Part of Appennines 2. Po valley 3. Po river 4. Milano
5. Rome 6. Tuscany (agricultural area) 7. Corsica island
Figure 49: UMD land cover (index as in figure 31).

The emissivities are low in the Po valley and also for Tuscany croplands (except for some forest cover areas); for channel-3, they range from about 0.75 to a rare maximum of 0.89, and for channel-4 from about 0.88 to 0.94. The Apennines (mountains) are characterized by relatively high emissivities (0.88 to 0.93 in channel-3 and ~0.95 to 0.98 in channel-4), which correspond to the relatively high NDVI values. The Mediterranean Sea surface temperature lies between 7°C and 14°C during nighttime, and between 14°C and 18°C during daytime. LST ranges from 4°C to 14°C during nighttime (maximum at 5-6°C), and from 27°C to about 40°C during daytime (maximum at 30°C). The diurnal variation of air temperature (at 2 mts height) over the area for the same date varies from about 8°C to 26°C.

7 Comparison between spectral and vegetation method

Let's get my incantation right:
"I wish I may, I wish I might"
Give earth another satellite.

Robert Lee Frost (1874- 1963)
In A Wishing Well

Using NDVI (normalized difference vegetation index) based methods, emissivity can be derived with reduced computational effort and less complex atmospheric correction procedures. Advanced NDVI based methods can be used, if the LSE (land surface emissivity) of bare ground and vegetation as well as the vegetation structure and its distribution are known (Valor and Caselles, 1996); with only NDVI information available, simpler NDVI based methods can be used (Sobrino and Raissouni, 2000). For known areas and with limited computational resources, the simple approach is advantageous and can be combined with a SWT (split-window technique) for LST (land surface temperature) estimation (Sun, Göttsche, Olesen, and Fischer, 2002). However, for bare land or wet soil the use of NDVI based methods is inappropriate. Respecting these limitations, a comparative study between a simple NDVI and the TISIE approach for LSE estimation was performed.

7.1 A vegetation index based method for emissivity estimation in 8-13 μm window

Of the various vegetation indices, NDVI is widely used and is defined in terms of channel reflectivities as: $(\text{NIR} - \text{Red})/(\text{NIR} + \text{Red})$, NDVI for AVHRR = $(\text{ch2} - \text{ch1})/(\text{ch2} + \text{ch1})$, where, ch1 ranges from 0.58 - 0.68 μm and ch2 ranges from 0.725 - 1.1 μm . Due to the red-edge effect of the vegetation, which is caused by the specific absorption characteristics of chlorophyll and leaf stomata structure, higher and lower NDVIs indicate a higher and lower vegetation density, respectively. Soils have a near constant reflectance (only little spectral variation) in these channels, which results in NDVIs near zero; for vegetation, NDVI usually ranges from 0.1 to 0.6. Due to atmospheric scattering and absorption, TOA (top-of-the-atmosphere) ch1 values become relatively more than ch2 and, consequently, NDVI is reduced. However, due to the rationing of the channels, NDVI is less effected than the individual radiances. Figure 50 shows the NDVI over the study area. The NDVI-based approach (for LSE) by Sobrino and Raissouni (2000) uses a correlation between NDVI and plant cover fraction (P_V), which has a square root relation with scaled NDVI. The method estimates P_V and bare soil ($1 - P_V$) for a given FOV. For $\text{NDVI}_{\min} = 0.2$ (bare soil) and $\text{NDVI}_{\max} = 0.5$ (full vegetation), P_V is given by (Carlson and Ripley, 1997):

$$P_V = \left(\frac{\text{NDVI} - \text{NDVI}_{\min}}{\text{NDVI}_{\max} - \text{NDVI}_{\min}} \right)^2 = \frac{(\text{NDVI} - 0.2)^2}{0.09} \quad (42)$$

For $0.5 \geq \text{NDVI} \geq 0.2$, Sobrino and Raissouni (2000) utilized an empirical relationship between P_V and the average channel LSE in AVHRR channels 4 and 5:

$$\varepsilon = (\varepsilon_4 + \varepsilon_5)/2 = 0.971 + 0.018P_V \quad (43)$$

$$\Delta\varepsilon = \varepsilon_4 - \varepsilon_5 = 0.006(1 - P_V) \quad (44)$$

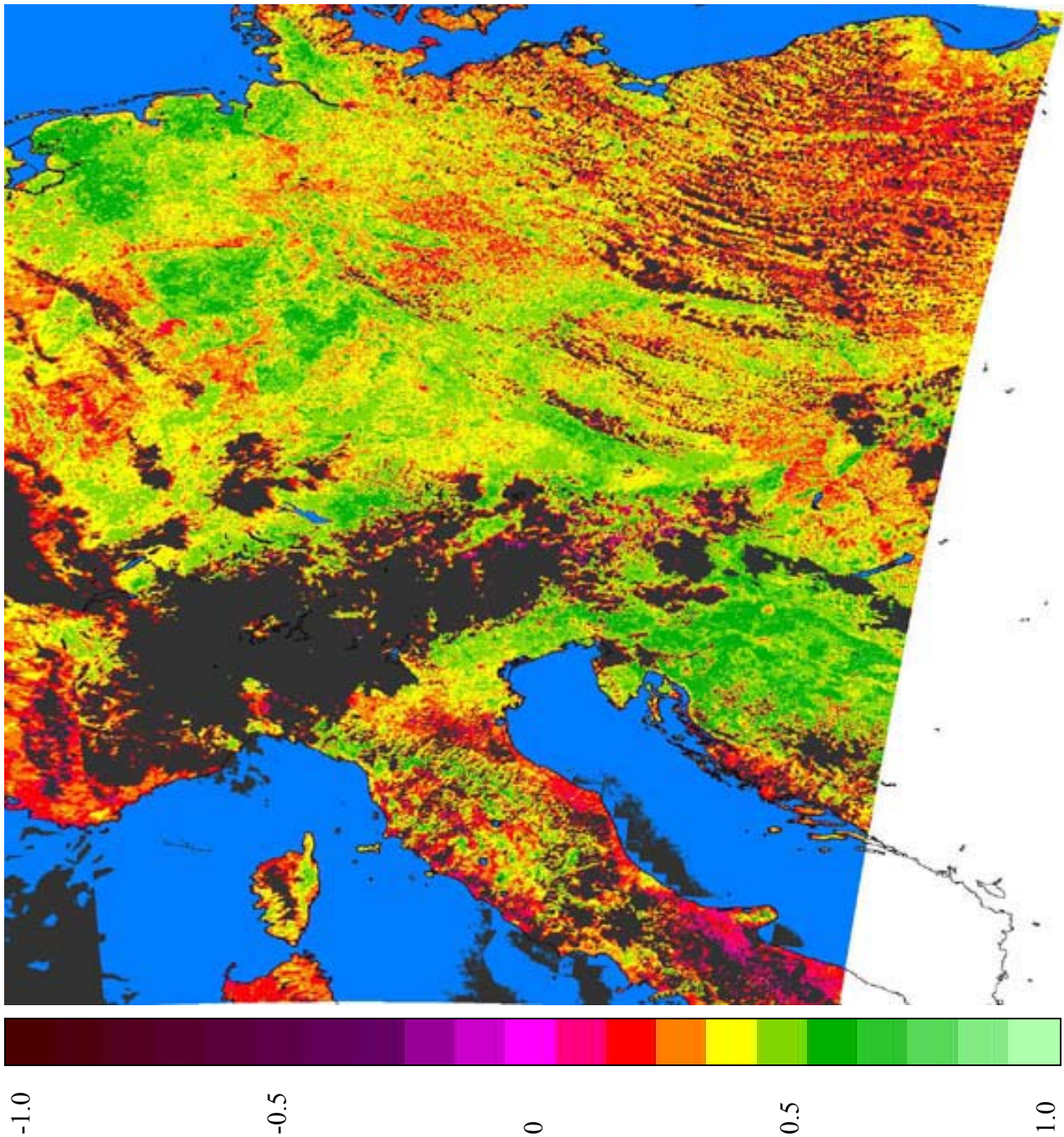


Figure 50: NDVI values over the study area for 20.08.1996. The white-pixels are missing data, the blue-pixels represent the sea surface and other water bodies, and the dark-gray pixels are areas covered by clouds during daytime (1400 hrs UTC). Vegetated areas are shown as green and non-vegetated areas tend towards red. The image gives an overview of the vegetation distribution over a large part of central Europe [upper-left: 55° N–5° E lower-right: 40°30'11.6" N–20°21'09.4" E].

For $NDVI > 0.5$, the pixels were considered to be fully vegetated ($P_v = 1$) and the emissivities for AVHRR channels 4 and 5 were set to 0.990. For $NDVI < 0.2$ the pixels are considered to be bare soil ($P_v = 0$) and an empirical relationship between the average LSE in AVHRR channels 4 and 5 and the reflectance ρ_1 in channel-1 was used:

$$\varepsilon = 0.980 - 0.042\rho_1 \quad (45)$$

$$\Delta\varepsilon = -0.003 - 0.029\rho_1 \quad (46)$$

Sobrino and Raissouni (2000) obtained the coefficients for equations (43), (44), (45), and (46) by using a spectral database and applying a geometric model to four typical vegetation structures (legume, vineyard, orange grove, and forest).. The calculation of P_v depends on the NDVI-thresholds (maximum and minimum), which vary with respect to the area under consideration; the chosen values are preferably set to 0.05 below maximum (Carlson and Ripley, 1997). In the present study, these thresholds were chosen on the basis of image histograms: $NDVI_{min} = 0.15$ (bare soil) and $NDVI_{max} = 0.65$ (full vegetation). With these values, P_v is given by:

$$P_v = \left(\frac{NDVI - NDVI_{min}}{NDVI_{max} - NDVI_{min}} \right)^2 = \frac{(NDVI - 0.15)^2}{0.25} \quad (47)$$

Figure 51 shows the P_v values obtained using equation (47). Additionally, the TISIE-based AVHRR channel-4 and channel-5 LSEs and channel-1 reflectivities were used as input to equations [(43)–(46)], for which the coefficients were derived by linear regression for the present study area and the given date. The regression of TISIE-based LSE and NDVI-based P_v for a selection of pixels (NDVI ranging from 0.15 to 0.65, no clouds, no water) yielded the following coefficients (Figure 52 and Figure 53):

$$\varepsilon = 0.928 + 0.022P_v \quad (48)$$

$$\Delta\varepsilon = 0.012 - 0.0044(1 - P_v) \quad (49)$$

Similarly, for $NDVI < 0.15$ a linear regression (Figure 54 and Figure 55) was performed between average LSEs and differences in LSE for AVHRR channels 4 and 5 and the reflectance ρ_1 in channel 1; the determined relations (for the given date) are:

$$\varepsilon = 0.914 - 0.034\rho_1 \quad (50)$$

$$\Delta\varepsilon = 0.029 - 0.069\rho_1 \quad (51)$$

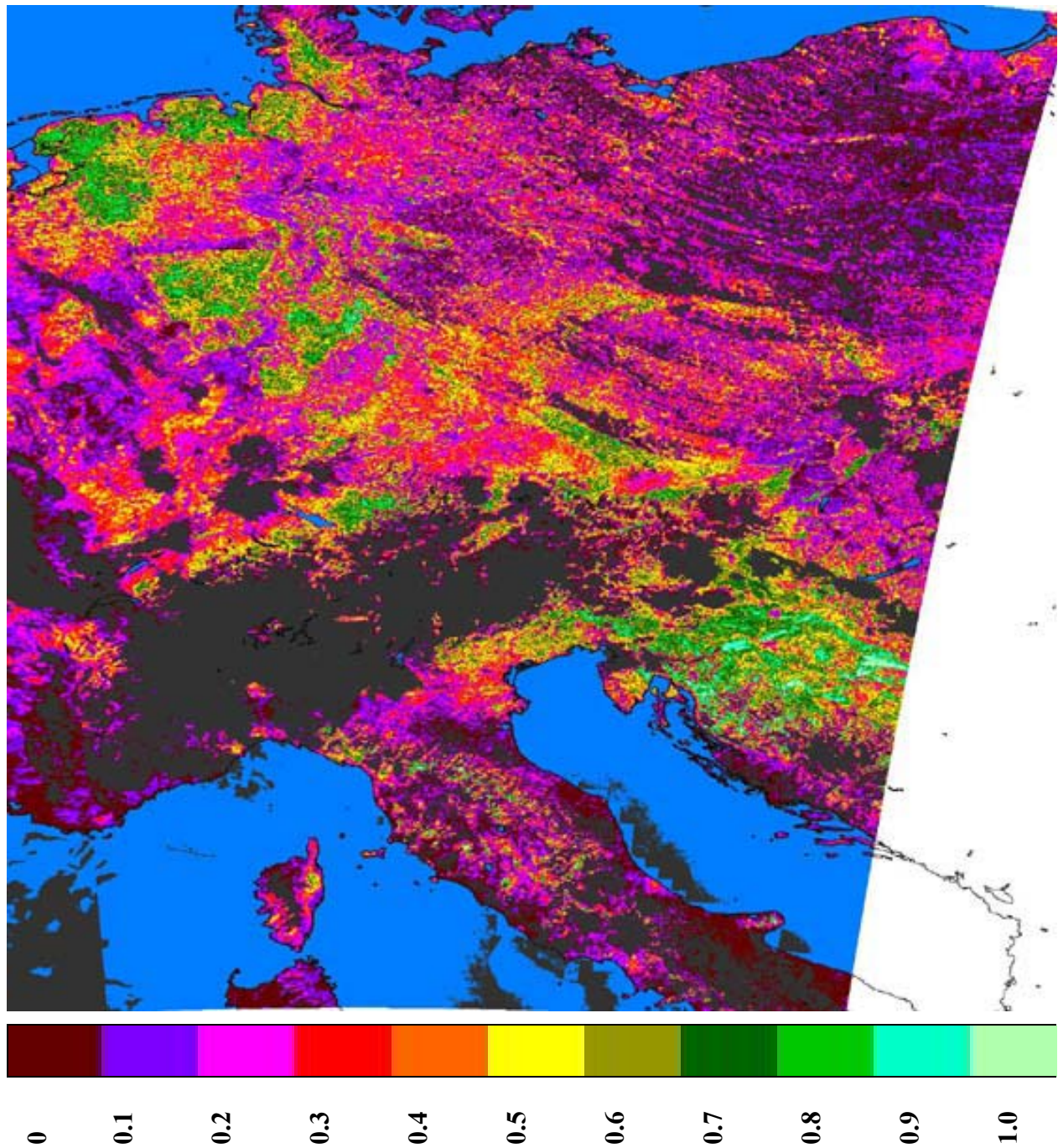


Figure 51: Vegetation fraction (P_v) derived from NDVI over the study area [upper-left: 55° N–5° E lower-right: 40°30'11.6" N–20°21'09.4" E] for 20.08.1996. The white-pixels are missing data, the blue-pixels represent the sea surface and other water bodies, and the dark-gray pixels represent daytime clouds (1400 hrs UTC) [upper-left: 55° N–5° E lower-right: 40°30'11.6" N–20°21'09.4" E].

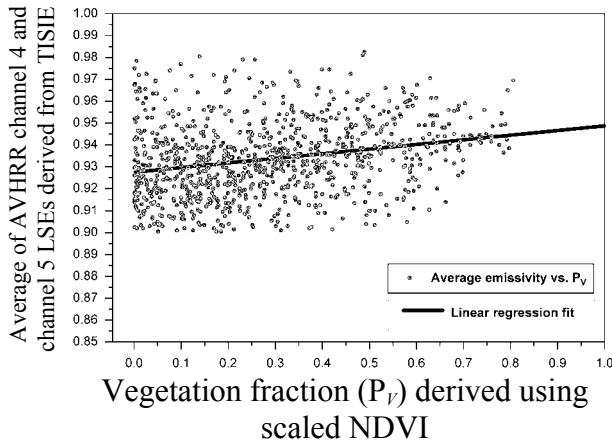


Figure 52: Regression line for P_V and average LSE. P_V is derived NDVI and average-LSEs are obtained from TISIE derived LSEs. (slope = 0.022; intercept = 0.928; correlation coefficient = 0.28)

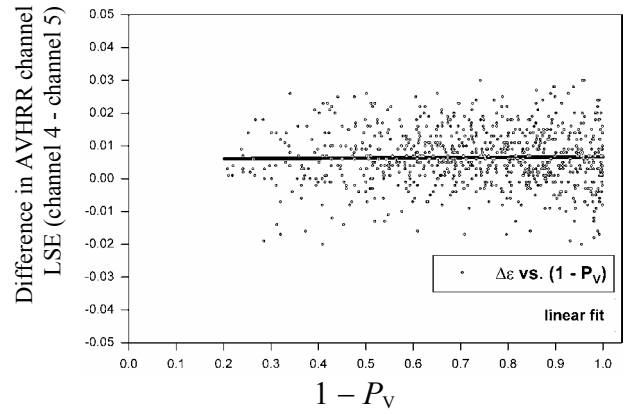


Figure 53: Regression line between $(1 - P_V)$ and difference in emissivities. P_V is derived from NDVI and LSEs are obtained based on TISIE approach. (slope = -0.0044; intercept = 0.012; correlation coefficient = -0.075)

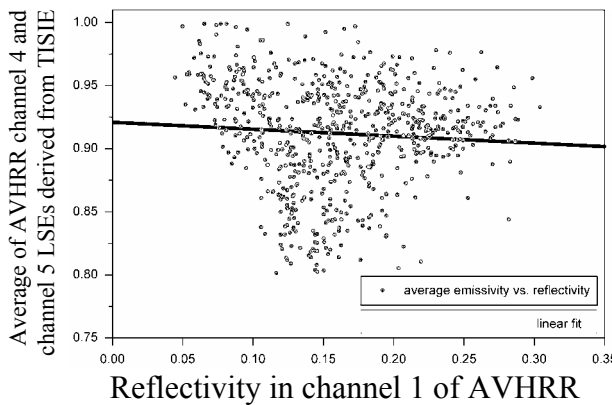


Figure 54: Regression line for AVHRR channel 1 reflectivity and channel 4 and channel 5 average LSE derived using TISIE. Only pixels with NDVI < 0.15 were considered. (slope = -0.034; intercept = 0.914; correlation coefficient = -0.04)

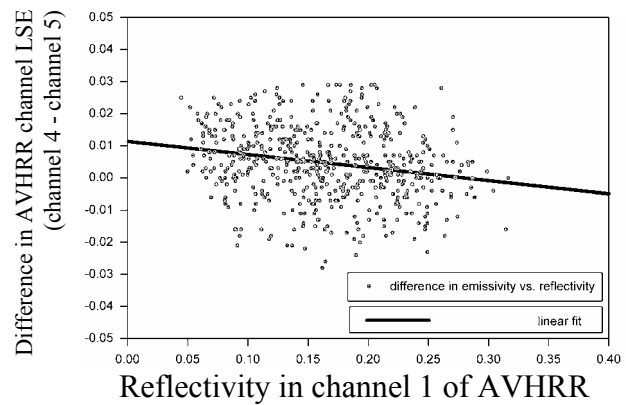


Figure 55: Regression line for AVHRR channel 1 reflectivity and difference between channel 4 and channel 5 LSE (4 - 5). Only pixels with NDVI < 0.15 were considered. (slope = -0.069; intercept = 0.029; correlation coefficient = -0.12)

Once ϵ ($\epsilon_4 + \epsilon_5$) and $\Delta\epsilon$ ($\epsilon_4 - \epsilon_5$) values for each pixel are known, ϵ_4 and ϵ_5 can be directly separated. Figure 56 shows AVHRR channel-4 LSE, which was derived using equations [(47)–(51)].

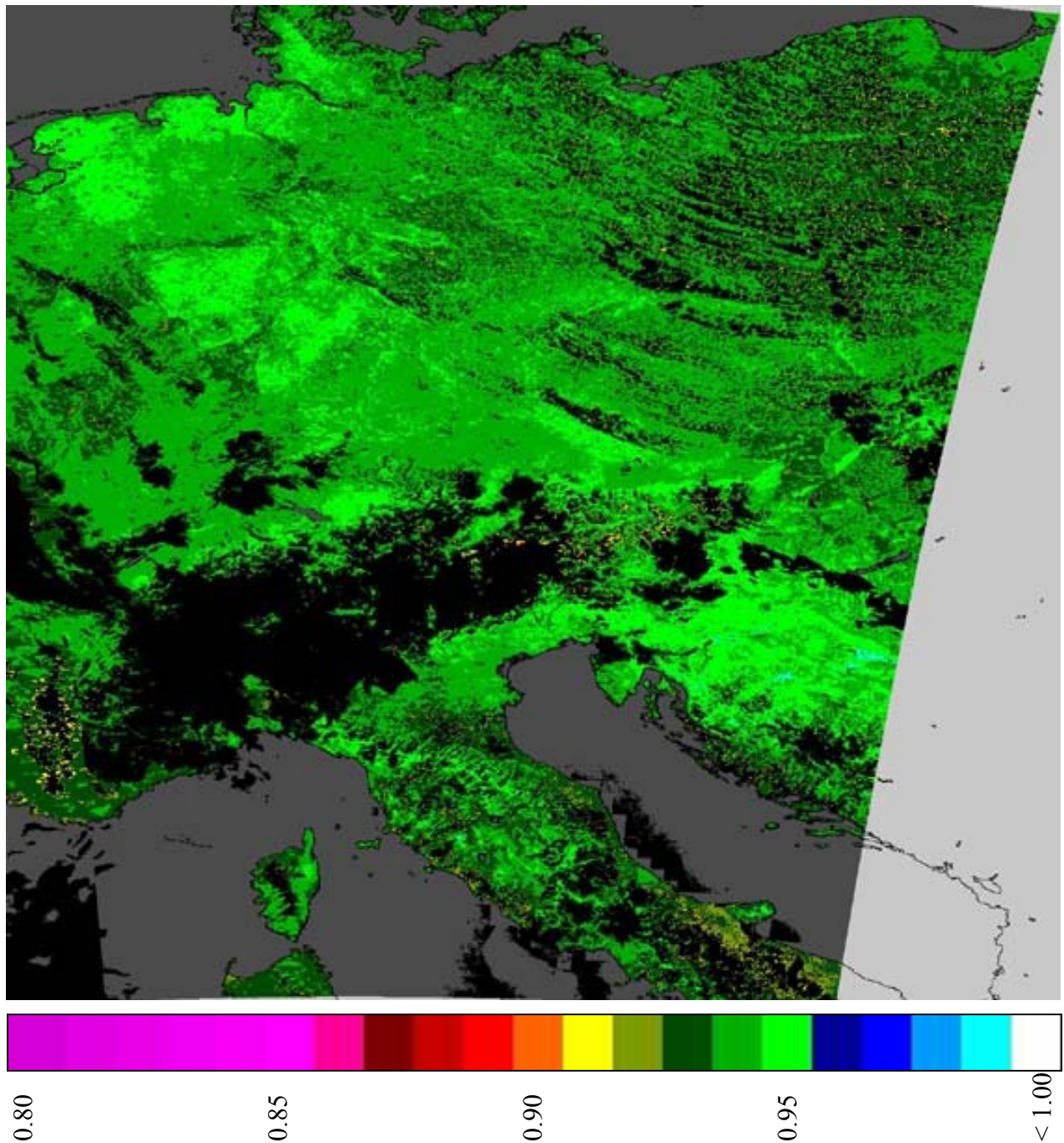


Figure 56: AVHRR channel 4 land surface emissivities over central Europe (for 20.08.1996) derived from a NDVI-based method combined with channel-1 reflectivities. The light-gray pixels are missing data, the dark-gray pixels represent the sea surface and other water bodies, and the black pixels represent daytime clouds (1400 hrs UTC) [upper-left: 55° N–5° E lower-right: 40°30'11.6" N–20°21'09.4" E].

For comparison, the difference between NDVI-based channel-4 LSE and TISIE-based channel-4 LSE was calculated (Figure 57).

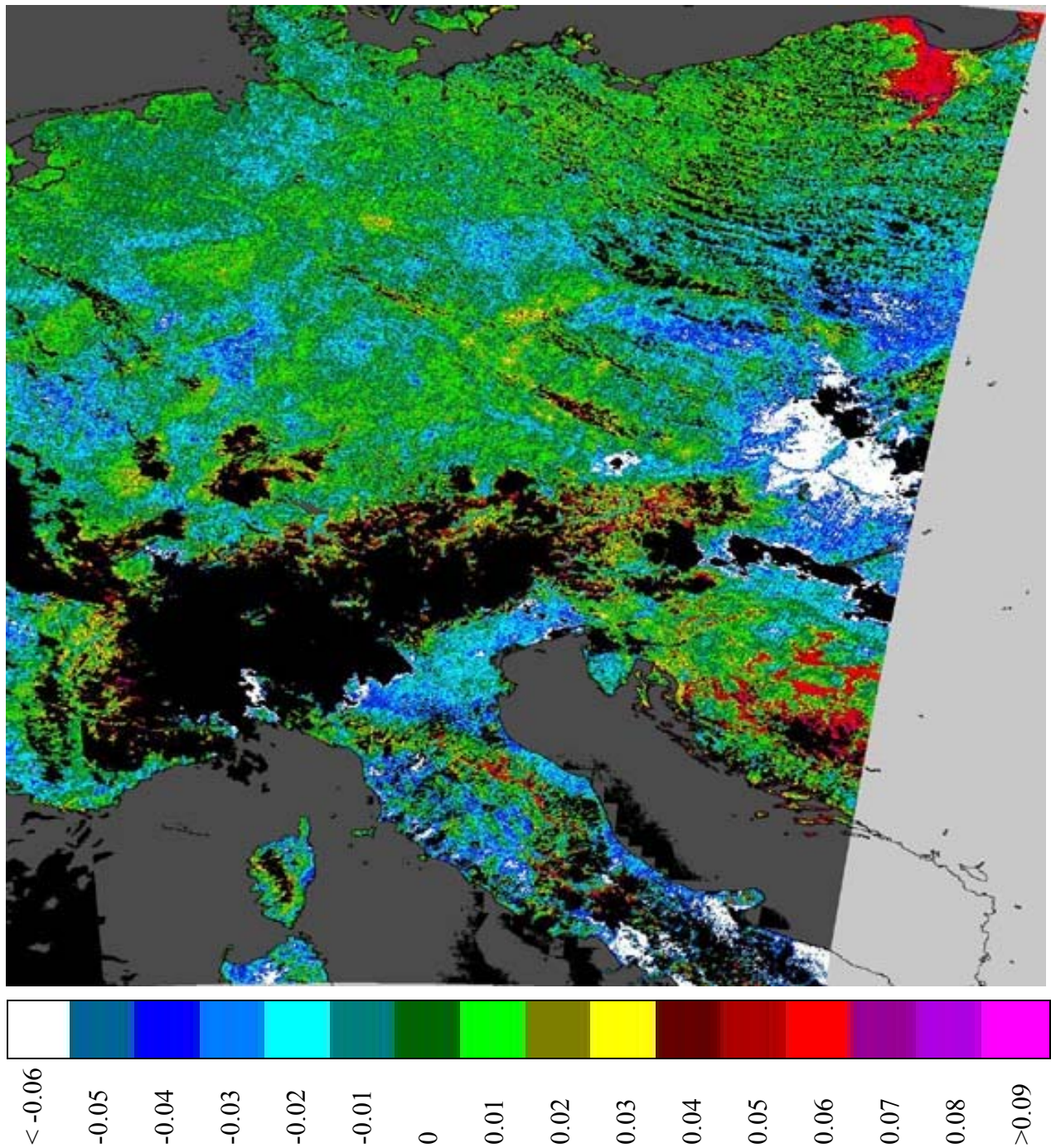


Figure 57: Emissivity difference map for 20.08.1996 derived by subtracting NDVI-based channel-4 emissivities from TISI-based AVHRR channel-4 emissivities. The black pixels represent area covered by clouds during daytime (1400 hrs UTC), the light-gray color represents missing data, and the dark-gray pixels represent the sea surface and other water bodies [upper-left: 55° N-5° E lower-right: 40°30'11.6" N-20°21'09.4" E].

Unlike the channel-4 LSEs derived using the TISIE approach, which range from 0.88 to less than 0.99 (peak at ~ 0.94), the NDVI-based LSEs range from 0.91 to 0.96 and few pixels have LSEs larger than 0.98; however, most of the values are at ~ 0.94 . When using the TISIE approach, the LSEs of the forest covered areas are well distributed between 0.95 and 0.98 in channel-4, but they are mainly around 0.95 for the NDVI-approach. In general, the range of LSE is compressed for the NDVI-based approach, *i.e.* a substantial amount of the dynamics is lost; this is partially controlled by the intercept and slope of the corresponding linear fit. Additionally, it has a very distinct pattern similar to the distribution pattern of the NDVIs. For channel-4 and for the given date and area, the LSE difference between the two methods (TISIE-based LSE – NDVI-based LSE) ranges between -0.06 to 0.06 . The distribution of these differences has a peak between 0.0 and 0.2 (mostly for forests and thickly vegetated areas), a second peak at around -0.02 to -0.04 (wooded grasslands, shrublands, harvested areas), and a third peak at around 0.05 to 0.06 for areas with low emissivities (bare land, urban areas). In summary, the main advantage of the NDVI method is that it is easily implemented and holds well for vegetated areas. However, it clearly has its limitations, *e.g.* no atmospheric correction is performed and the NDVI is for the TOA. Furthermore, for deriving the coefficients, a prior knowledge about LSEs and the vegetation structure is required and the method is not able to capture a wider dynamic range of emissivity.

8 Conclusions and outlook

Do not think lightly of good, that nothing will come of it. A whole water pot will fill up from dripping drops of water.

Lord Buddha
In *Dhammapada* (v 122)

Land surface temperature (LST) is an important indicator of the energy balance at the Earth's surface. Thermodynamic point measurements are of limited use for LST estimation, *i.e.* only satellite measurements are feasible on large scales. The focus of this study was to:

- Select an appropriate method for estimating LST, and, as an *a priori* requirement, for the estimation of land surface emissivity (LSE). In order to capture the emissivity dynamics for various land surface types, the method should be based on physical rather than empirical relations.
- Establish an operational set-up and adapt the method to NOAA AVHRR data (archived by the MSA group) and the recent MSG SEVIRI data (to be received at MSA using a HRUS).

The temperature independent thermal infrared spectral indices (TISI) method was chosen for LSE estimation; subsequently, LST and LSE are de-coupled from surface radiances. NOAA-14 AVHRR TOA (top-of-the-atmosphere) data was available and ECMWF atmospheric profiles were used in MODTRAN to calculate atmospheric attenuation, path-radiance, and reflected irradiance. The LSE in the 3-4 μm range can be calculated via reflectivity, if total radiance, emitted radiance, and solar irradiance, at Earth's surface level, are known. The total-radiance was obtained by applying atmospheric corrections to TOA data and solar-irradiance was calculated. The emitted part of the surface was estimated using combined day-night TISI ratios. TISI can be constructed for any number of channels large than one. In the present study, TISI were derived for two channels, aimed at reducing the cumulative effect of channel errors and the time needed for calculation. Using simulated surface NOAA-14 AVHRR radiances for 6 model atmospheres and 13 surface types, a method validation showed that the *RMS* errors in LSE estimation, when retrieved with the 2-channel TISI, are 0.016 for channel-3, 0.009 for channel-4, and 0.005 for channel-5. For MSG SEVIRI, using 3 atmospheres (MLS, MLW, TROP) and 11 surface types, the method resulted in an *RMS* LSE error of 0.031 for channel-5, 0.016 for channel-10, and 0.009 for channel-11. For near-nadir-measurements ($< 30^\circ$), considering sensor $NEAT$ (< 0.12 K for AVHRR, 0.11 K for SEVIRI), MODTRAN's intrinsic error and the *RMS* error in emissivity introduced by the method, a local version of the scheme was set-up with an estimated accuracy of ± 1.5 to 2 K in LST. However, it is assumed that atmospheric information is correct; the output result will be only as good as the input data. The TISI method does not require *a priori* emissivity, but yields only channel LSE ratios. In order to obtain absolute angular LSE, an initial emissivity has to be used (chapter 5) and surfaces are assumed to be Lambertian. However, since this initial emissivity is only used in a ratio which is consequently further ratioed, its impact is negligible. An investigation performed over central Europe for an assumed range of this initial emissivity of 0.94 to 0.99 shows that the variation of final LSEs is only of the order of 0.0001-0.001, which is considerably less than the achievable accuracy. An initially envisaged idea was to provide realistic LSE from another easier method (NDVI-based). However, as the assumption turned out to be uncritical, *i.e.* variation of LSE is only of the order of 0.0001-0.001, the idea was not implemented.

The method was applied over a large part of central Europe; additionally, data for different times were compared in order to observe seasonal differences (chapter 6). The method captures a large range of emissivities from highly vegetated forest areas to harvested bare grounds and urban set-

ups. However, due to its highly specular characteristics the assumption of Lambertian behavior does not hold for water surfaces. Hence, values from a spectral library (convoluted with response function) were used. Land surface temperature was directly separated from surface radiances and calculated emissivities. LST shows a wide diurnal variation between 5°C and 35°C, while the sea surface varies between 15°C and 28°C (for the particular date). LST is the temperature of the skin of Earth's surface and is determined by the balance between the incoming solar and longwave irradiation, outgoing terrestrial infrared radiation, sensible and latent heat flux, and ground heat flux. LST doesn't necessarily reflect the air temperature and the difference between lowest air temperature (*e.g.* air temperature in ECMWF profiles at 2 mts) and LST could be higher than 10°C. Additionally, the spatial variation of air temperature is relatively smooth and LST varies rapidly within short distances. Using NDVI-based methods, emissivity can be estimated with reduced computational effort and less complex atmospheric correction procedures. An NDVI-based method was employed for comparison purposes and the required coefficients were adjusted to the study area using the emissivities derived with the TISI method. Once the coefficients for the NDVI-based method have been obtained, it can be easily implemented and holds well for vegetated areas. However, in order to derive the coefficients, prior knowledge of LSEs and the vegetation structure is required; the method is also incapable of capturing a wide range of emissivity.

The TISI method is robust and is adapted to sensors with 2 channels (one within 3-4 μm and other in 10-12 μm spectral range). It is independent of land-cover type as long as the surface does not deviate too much from the Lambertian assumption (*e.g.* snow cover, extended water bodies *etc.*). In order to ensure the method's reliability, it should be compared with field measurements; furthermore, its performance can be improved as follows:

- Include BRDF characterization or provide BRDF from external sources: this is not critical for land surface observations and view angles smaller than 30°; however the BRDF is necessary to characterize the angular variation of emissivity.
- Improved calculation of downwelling radiance (hemispherical irradiance divided by π): even though this variable has little impact, it leaves some scope for improvement. In the present work, it is assumed that the hemispherical downwelling atmospheric irradiance equals π times the downwelling radiance at 53° angle. However, recent versions of radiative transfer models, *e.g.* MODTRAN-4, allow more accurate calculations.
- Except for highly vegetated areas, LSE decreases with increasing zenith angles. Channel-3 (AVHRR) LSEs are essentially daytime emissivities and for night-time, invariability of LSE is assumed. For sensors onboard polar-orbiters, zenith angles vary between day and night; channel-3 angular LSE is used to obtain angular emissivities for the other channels using night-time ratios. This causes discrepancies for strong variations of zenith angles. Using similar and near-nadir view angles for both day and night, *e.g.* from MSG SEVIRI, can overcome this limitation.
- Improved cloud detection with dynamic threshold can remove otherwise undetected clouds.
- In order to enhance computational speed, it is desired to use a fast but still accurate method for the calculation of atmospheric variables. In order to speed-up the radiative transfer calculations, a Neural Network (Göttsche and Olesen, 2002) could be considered.

For overcoming the poor data coverage due to clouds, emissivity composites, *e.g.* for 10 days, can be constructed. Additionally, for faster applications without complicated atmospheric correction procedures, coefficients for easier NDVI-based methods can be computed on a seasonal basis using LSE derived with the TISI method. LST is an indicator of the energy dynamics between solar irradiance, the atmosphere, and Earth's surface. The balance of the skin-

temperature depends on the infrared radiation and the transmission properties of water vapor, clouds, and other trace constituents. Hence, continuous estimates of LST on a global scale are required for a better understanding of the radiation balance and to improve the results of global circulation models (GCMs) and numerical weather prediction (NWP) models. It would also be beneficial to compare LST with surface temperatures from vertical sounding data, *e.g.* TOVS, which are synchronous and collateral. The work provides an opportunity to derive a climatological time series of LST based on satellite sensor data alone.

References

- BECKER, F., and Z-L. LI, 1995, Surface temperature and emissivity at different scales: definition, measurement and related problems. *Remote Sensing Reviews*, 12, 225-253.
- BECKER, F., and Z-L. LI, 1990a, Temperature-independent spectral indices in thermal infrared bands. *Remote Sensing of Environment*, 32, 17-33.
- BECKER, F., and Z-L. LI, 1990b, Towards a local split window method over land surface. *International Journal of Remote Sensing*, 11, 369-394.
- BECKER, F., 1987, The impact of spectral emissivity on the measurement of land surface temperature from a satellite. *International Journal of Remote Sensing*, 8, 1509-1522.
- BERK, A., G. P. ANDERSON, P. K. ACHARYA, J. H. CHETWYND, L. S. BERNSTEIN, E. P. SHETTLE, M. W. MATTHEW, and S. M. ADLERR-GOLDEN, 2000, MODTRAN4 User's Manual, *Air Force Research Laboratory*, Hanscom, USA.
- BERTRAND, C., J. P. van YPERSELE, and A. BERGER, 2002, Are natural climate forcings able to counteract the projected anthropogenic global warming?. *Climatic Change*, 4, 413-427.
- CARLSON, T. N., and D. A. RIPLEY, 1997, On the relation between NDVI, fractional vegetation, and leaf area index. *Remote Sensing of Environment*, 62, 241-252.
- CHEDIN, A., N. SCOTT, and A. BERROIR, 1982, A single-channel double viewing method for SST determination from coincident Meteosat and TIROS-N measurements. *Journal of Applied Meteorology*, 21, 613-618.
- COLL, C., V. CASELLES, E. RUBIO, F. SOSPEDRA, and E. VALOR, 2000, Temperature and emissivity separation from calibrated data of the digital airborne imager spectrometer, *Remote Sensing of Environment*, 76, 250-259.
- COLL, C., and V. CASELLES, 1997, A split-window algorithm for land surface temperature from advanced very high resolution radiometer data: Validation and algorithm comparison, *Journal of Geophysical Research*, 102, 16697-16713.
- COLL, C., V. CASELLES, J. A. SOBRINO, and E. VALOR, 1994, On the atmospheric dependence of the split-window equation for land surface temperature. *International Journal of Remote Sensing*, 15, 105-122.
- DASH, P., F.-M. GÖTTSCHE, F.-S. OLESEN, and H. FISCHER, 2002a, Land surface temperature and emissivity estimation from passive sensor data: theory and practice; current trends, *International Journal of Remote Sensing*, 23, 2563-2594.
- DASH, P., F.-M. GÖTTSCHE, and F.-S. OLESEN, 2002b, Potential of MSG for surface temperature and emissivity estimation: considerations for real-time applications, *International Journal of Remote Sensing*, 23, 4511-4518.
- DASH, P., F.-M. GÖTTSCHE, and F.-S. OLESEN, 2003, Emissivity and temperature estimation from MSG SEVIRI data; method validation with simulated and NOAA-14 AVHRR data, *Advances in Space Research*, 32, 2241-2246.
- DASH, P., F.-M. GÖTTSCHE, F.-S. OLESEN, and H. FISCHER, 2001, Retrieval of land surface temperature and emissivity from satellite data: physics, principle limitations and current methods, *Journal of the Indian Society of Remote Sensing*, 29, 23-30.
- DESCHAMPS, P. Y., and T. PHULPIN, 1980, Atmospheric correction of infrared measurements of sea surface temperature using channels at 3.7, 11, and 12 μm . *Boundary Layer Meteorology*, 18, 131-143.

- ECMWF Report, 1995, User guide to ECMWF products, *Meteorological Bulletin* M3.2, ed. 2.1, 31 pp.
- FRANCA, G. B., and A. P. CRACKNELL, 1994, Retrieval of land and sea surface temperature using NOAA-11 AVHRR data in north-eastern Brazil. *International Journal of Remote Sensing*, 15, 1695-1712.
- FRANÇOIS, C., and C. OTTLÉ, 1996, Atmospheric corrections in the thermal infrared: global and water vapor dependent split-window algorithms- applications to ATSR and AVHRR data. *IEEE Transactions on Geoscience and Remote Sensing*, 34, 457-470.
- GILLESPIE, A. R., S. ROKUGAWA, T. MATSUNAGA, J. S. COTHERN, S. J. HOOK, and A. B. KAHLE, 1998, A temperature and emissivity separation algorithm for Advanced Spaceborne Thermal Emission and Reflection Radiometer (ASTER) images. *IEEE Transactions on Geoscience and Remote Sensing*, 36, 1113-1126.
- GILLESPIE, A. R., S. ROKUGAWA, S. J. HOOK, T. MATSUNAGA, and A. B. KAHLE, 1996/1999, Temperature/emissivity separation algorithm theoretical basis document, Version 2.3/2.4., NASA5-31372, NASA/GSFC, Greenbelt, MD, USA.
(http://eosps0.gsfc.nasa.gov/ftp_ATBD/REVIEW/ASTER/ATBD-AST-03/atbd-ast-03.pdf).
- GILLESPIE, A. R., 1985, Lithologic mapping of silicate rocks using TIMS. Proceedings TIMS Data User's Workshop, (JPL Pub. 86-38, Jet Propulsion Laboratory, Pasadena, CA), pp. 29-44.
- GOODRUM, G., K. B. KIDWELL, W. WINSTON, (eds.), 2000, NOAA KLM User's Guide, U.S. Department of Commerce, NOAA, NESDIS, NCDC, Climate Services Division, Satellite Services Branch, Suitland, MD, USA.
- GOÏTA, K., and A. ROYER, 1997, Surface temperature and emissivity separability over land surface from combined TIR and SWIR AVHRR data, *IEEE Transactions on Geoscience and Remote Sensing*, 35, 718-733.
- GÖTTSCHE, F.-M., and F.-S. OLESEN, 2002, Evolution of neural networks for radiative transfer calculations in the terrestrial infrared. *Remote Sensing of Environment*, 80, 157-164.
- GU, D., A. R. GILLESPIE, A. B. KAHLE, and F. D. PALLUCONI, 2000, Autonomous Atmospheric Compensation (AAC) of high resolution hyperspectral thermal infrared remote-sensing imagery. *IEEE Transactions on Geoscience and Remote Sensing*, 38, 2557-2569.
- HANSEN, M. C., R. S. DeFRIES, J. R. G. TOWNSHED, and R. SOHLBERG, 2000, Global land cover classification at 1 km spatial resolution using a classification tree approach, *International Journal of Remote Sensing*, 21, 1331-1364.
- HOOK, S. J., A. R. GABELL, A. A. GREEN, and P. S. KEALY, 1992, A comparison of techniques for extracting emissivity information from thermal infrared data for geologic studies. *Remote Sensing of Environment*, 42, 123-135.
- HUNT, G. R., 1980, Electromagnetic radiation: The communication link in remote sensing. In *Remote Sensing Geology*, edited by B. S. SIEGEL and A. R. GILLESPIE (New York: John Wiley and Sons), pp. 5-45.
- IGNATOV, A. M., and I. L. DERGILEVA, 1994, Angular effect in dual-window AVHRR brightness temperatures over oceans. *International Journal of Remote Sensing*, 15, 3845-3850.
- JONES, P. D., 1994, Hemispheric surface air temperature variations: a reanalysis and an update to 1993, *Journal of Climate* 7, 1794-1802.

- KAHLE, A. B., D. P. MADURA, and J. M. SOHA, 1980, Middle infrared multispectral aircraft scanner data: analysis for geological applications. *Applied Optics*, 19, 2279-2290.
- KAPLAN L. D., 1959, Inference of atmospheric structure from remote radiation measurements, *Journal of the Optical Society of America*, 49, 1004-1007.
- KEALY, P. S., and S. J. HOOK, 1993, Separating temperature and emissivity in thermal infrared multispectral scanner data: Implications for recovering land surface temperatures. *IEEE Transactions on Geoscience and Remote Sensing*, 31, 1155-1164.
- KEALY, P. S., and A. R. GABELL, 1990, Estimation of emissivity and temperature using alpha coefficients. *Proceedings of second TIMS workshop*, (JPL Pub. 90-95, Jet Propulsion Laboratory, Pasadena, CA), pp. 11-15.
- KERR, Y. H., J. P. LAGOUARADE, and J. IMBERNON, 1992, Accurate land surface temperature retrieval from AVHRR data with use of an improved split window algorithm. *Remote Sensing of Environment*, 41, 197-209.
- KIDDER, S. Q., and T. H. VONDER HAAR, 1995, *Satellite Meteorology: an introduction*, 1st edn (London: Academic Press).
- KIDWELL, K. B. (Ed.), 1998, NOAA Polar Orbiter Data Users Guide (TIROS-N, NOAA-6, NOAA-7, NOAA-8, NOAA-9, NOAA-10, NOAA-11, NOAA-12, NOAA-13 and NOAA-14), U.S. Department of Commerce, NOAA, NESDIS, NCDC, Climate Services Division, Satellite Services Branch, Suitland, MD.
- KIMES, D. S., and J. A. KIRCHNER, 1983, Directional radiometric measurements of row-crops temperatures. *International Journal of Remote Sensing*, 4, 299-311.
- KIMES, D. S., S. B. IDSO, P. J. PINTER, R. J. REGINATO, and R. D. JACKSON, 1980, View angle effects in the radiometric measurement of plant canopy temperature. *Remote Sensing of Environment*, 10, 273-284.
- KING, J. I. F., 1956, Scientific use of Earth satellites -'the radiative heat transfer of planet earth', pp.133-136, *University of Michigan Press*, Ann Arbor, Michigan.
- KNEIZYS, F. X., D. C. ROBERTSON, L. W. ABREU, P. ACHARYA, G. P. ANDERSON, L. S. ROTHMAN, J. H. CHETWYND, J. E. A. SELBY, E. P. SHETTLE, W. O. GALLERY, A. BERG, S. A. CLOUGH, and L. S. BERNSTEIN, Edited by: L. W. ABREU, and G. P. ANDERSON, 11. Jan. 1996, The MODTRAN 2/3 Report and LOWTRAN 7 MODEL. *Phillipps Laboratory*, Hanscom, USA.
- KONDRATYEV, K. Y., 1969, Radiation in the atmosphere, International Geophysics Series Vol. 12, 16-22 pp., J. van MIEGHEM (Ed.), (*Academic Press : New York and London*).
- LAKSHMI, V., and J. SUSSKIND, 2000, Comparison of TOVS-derived land surface variables with ground observations. *Journal of Geophysical Research*, 105, 2179-2190.
- HOWARD, J. N., 1991, Atmospheric Physics. *Encyclopedia of Physics*, edited by R. G. LERNER and G. L. TRIGG, 2nd edn (New York: VCH Publishers), pp. 63-66.
- LI, Z-L., F. BECKER, M. P. STOLL, and Z. WAN, 1999, Evaluating six methods for extracting relative emissivity spectra from thermal infrared images. *Remote Sensing of Environment*, 69, 197-214.
- LI, Z-L., and F. BECKER, 1993, Feasibility of land surface temperature and emissivity determination from AVHRR data. *Remote Sensing of Environment*, 43, 67-85.

- McCLAIN, E. P., W. G. PICHEL, and C. C. WALTON, 1985, Comparative performance of AVHRR-based multichannel sea surface temperatures. *Journal of Geophysical Research*, 90, 11587-11601.
- McMILLIN, L. M., 1975, Estimation of sea surface temperature from two infrared window measurements with different absorption. *Journal of Geophysical Research*, 80, 5113-5117.
- NERRY, F., F. PETITCOLIN, and M. P. STOLL, 1998, Bidirectional reflectivity in AVHRR channel 3: application to a region in northern Africa. *Remote Sensing of Environment*, 66, 298-316.
- NERRY, F., J. LABED, and M. P. STOLL, 1988, Emissivity signatures in the thermal IR band for remote sensing: calibration procedure and method of measurements. *Applied Optics*, 27, 758-764.
- NOAA Technical Report NESDIS 71, August 1993, Spectral Radiance-Temperature conversions for measurements by AVHRR thermal channels 3, 4, 5. *Washington D.C., US Department of Commerce*, NOAA-NESDIS. pp.9.
- NORMAN, J. M., and F. BECKER, 1995, Terminology in thermal infrared remote sensing of natural surfaces. *Agricultural and Forest Meteorology*, 77, 153-166.
- PETITCOLIN, F., F. NERRY, and M. P. STOLL, 2002a, Mapping directional emissivity at 3.7 μm using a simple model of bi-directional reflectivity, *International Journal of Remote Sensing*, 23, 3443-3472.
- PETITCOLIN, F., F. NERRY, and M. P. STOLL, 2002b, Mapping temperature independent spectral indice of emissivity and directional emissivity in AVHRR channels 4 and 5, *International Journal of Remote Sensing*, 23, 3473-3491.
- PRABHAKARA, C., G. DALU, and V. G. KUNDE, 1974, Estimation of sea surface temperature from remote sensing in 11-13 μm window region. *Journal of Geophysical Research*, 79, 5039-5044.
- PRATA, A. J., V. CASELLES, C. COLL, J. A. SOBRINO, and C. OTTLÉ, 1995, Thermal remote sensing of land surface temperature from satellites: Current status and future prospects. *Remote Sensing Reviews*, 12, 175-224.
- PRATA, A. J., 1993, Land surface temperatures derived from the advanced very high resolution radiometer and the Along-Track Scanning Radiometer 1. Theory. *Journal of Geophysical Research*, 98, 16689-16702.
- PRICE, J. C., 1984, Land surface temperature measurements from the split window channels of the NOAA-7 AVHRR. *Journal of Geophysical Research*, 89, 7231-7237.
- PRICE, J. C., 1983, Estimation of surface temperatures from satellite thermal infrared data- a simple formulation for the atmospheric effect. *Remote Sensing of Environment*, 13, 353-361.
- QIN, Z., and A. KARNIELI, 1999, Progress in remote sensing of land surface temperature and ground emissivity using NOAA-AVHRR data. *International Journal of Remote Sensing*, 20, 2367-2393.
- REUTTER, H., F.-S. OLESEN, and H. FISCHER, 1994. Distribution of the brightness temperature of land surfaces determined from AVHRR data. *International Journal of Remote Sensing*, 15, 95-104.
- RICHTER, R., and C. COLL, 2002, Bandpass-resampling effects for the retrieval of surface emissivity, *Applied Optics*, 41, 3523-3529.

- SALISBURY, W., and D. M. D'ARIA, 1992, Emissivity of terrestrial materials in the 8-14 μm atmospheric window. *Remote Sensing of Environment*, 42, 83-106.
- SCHÄDLICH, S., F.-M. GÖTTSCHE, and F.-S. OLESEN, 2001, Influence of land parameters and atmosphere on Meteosat brightness temperatures and generation of land surface temperature maps by temporally and spatially interpolating atmospheric correction. *Remote Sensing of Environment*, 75, 39-46.
- SCHROEDTER, M., F.-S. OLESEN, and H. FISCHER, 2003, Determination of LST distributions from single channel IR measurements: An effective spatial interpolation method for the use of TOVS, ECMWF and radiosonde profiles in the atmospheric correction scheme. *International Journal of Remote Sensing*, 24, 1189-1196.
- SCOTT, N. A., and A. CHÉDIN, 1981, A fast line by line method from atmospheric absorption computations: the Automatized Atmospheric Absorption Atlas. *Journal of Applied Meteorology*, 20, 802-812.
- SHEPARD, D., August 1968, A two-dimensional interpolation function for irregularly-spaced data, Proceedings of 23rd National Conference of the Association for Computing Machinery, Brandon/Systems Press, Inc., Princeton, NJ, *ACM Publications. P-68*, pp. 517-524.
- SLATER, P. N., 1980, Remote sensing, optics and optical systems, (Reading, Massachusetts: Addison-Wesley).
- SNYDER, W. C., Z. WAN, Y. ZHANG, and Y.-Z. FENG, 1998a, Classification-based emissivity for land surface temperature measurement from space. *International Journal of Remote Sensing*, 19, 2753-2774.
- SNYDER, W. C., and Z. WAN, 1998b, BRDF models to predict spectral reflectance and emissivity in the thermal infrared. *IEEE Transactions on Geoscience and Remote Sensing*, 36, 214-225.
- SNYDER, W. C., Z. WAN, and X. LI, 1998c, Thermodynamic constraints on reflectance reciprocity and Kirchhoff's law, *Applied Optics*, 37, 3464-3470.
- SOBRINO, J. A., and N. RAISSOUNI, 2000, Toward remote sensing methods for land cover dynamic monitoring, application to Morocco, *International Journal of Remote Sensing*, 21, 353-366.
- SOBRINO, J. A., and J. CUENCA, 1999, Angular variation of thermal infrared emissivity for some natural surfaces from experimental measurements. *Applied Optics*, 38, 3931-3936.
- SOBRINO, J. A., Z.-L. LI, M. P. STOLL, and F. BECKER, 1996, Multi-channel and multi-angle algorithms for estimating sea and land surface temperature with ATSR data. *International Journal of Remote Sensing*, 17, 2089-2114.
- SOBRINO, J. A., C. COLL, and V. CASELLES, 1991, Atmospheric correction for land surface temperature using NOAA-11 AVHRR channels 4 and 5. *Remote Sensing of Environment*, 38, 19-34.
- SPENCER, J. W., 1971, Fourier series representation of the position of the Sun, *Search*, 2, 172.
- SUN, Y.-Y., F.-M. GÖTTSCHE, F.-S. OLESEN, and H. FISCHER, 2002, Retrieval of land surface temperature from combined AVHRR data. *Annales Geophysicae*, 20, 1257-1259.
- SUSSKIND, J., J. ROSENFELD, D. REUTER, and M. T. CHAHINE, 1984, Remote sensing of weather and climate parameters from HIRS2/Msu on TIROS-N. *Journal of Geophysical Research*, 89, 4677-4697.

- VALOR, E., and V. CASELLES, 1996, Mapping land surface emissivity from NDVI: Application to European, African, and South American areas. *Remote Sensing of Environment*, 57, 167-184.
- van de GRIEND, A. A., and M. OWE, 1993, On the relationship between thermal emissivity and the normalized difference vegetation index for natural surfaces. *International Journal of Remote Sensing*, 14, 1119-1131.
- WAN, Z., and J. DOZIER, 1996, A generalized split-window algorithm for retrieving land-surface temperature from space. *IEEE Transactions on Geoscience and Remote Sensing*, 34, 892-905.
- WARK, D. Q., G. YAMAMOTO, and J. LIENESCH, 1962, Infrared flux and surface temperature determinations from TIROS radiometer measurements, Report (US Weather Bureau Meteorological Satellite Laboratory), no. 10. M07.362.2 U587re no.10, Washington, D.C.
- WALTON, C. C., 1988, Nonlinear multichannel algorithms for estimating sea surface temperature with AVHRR satellite data, *Journal of Applied Meteorology*, 27, 115-127.
- WATSON, K., 1992, Spectral ratio method for measuring emissivity. *Remote Sensing of Environment*, 42, 113-116.

Notations

<u>Variable</u>	<u>Explanation</u>	<u>Units</u>
$B(\lambda, T)$	radiance emitted from a blackbody (monochromatic)	$\text{Wm}^{-2}\mu\text{m}^{-1}\text{sr}^{-1}$
λ, T	wavelength, temperature	$\mu\text{m}, \text{K}$
$B_k(T)$	spectral integration of $B(\lambda, T)$ with f_k in channel k	$\text{mWm}^{-2}\text{sr}^{-1}\text{cm}$
f_k	normalized channel response function	---
$\varepsilon(\lambda), \varepsilon_k$	spectral emissivity, channel emissivity (for any surface)	---
$R(\lambda, T)$	spectral radiance [$B(\lambda, T) \cdot \varepsilon(\lambda)$]	$\text{Wm}^{-2}\mu\text{m}^{-1}\text{sr}^{-1}$
R_k	surface channel radiance ($= \varepsilon_k B_k(T_s) + (1 - \varepsilon_k)L_k^\downarrow$)	$\text{mWm}^{-2}\text{sr}^{-1}\text{cm}$
C_1	constant in Planck's function $= 2\pi hc^2$ ($3.7418 \cdot 10^{-16}$)	Wm^2
C_2	constant in Planck's function $= hc/k$ ($1.4388 \cdot 10^{-2}$)	mK
h	Planck's constant ($6.626076 \cdot 10^{-34}$)	Js
c	velocity of light ($2.99792458 \cdot 10^8$)	ms^{-1}
k	Boltzmann's constant ($1.380658 \cdot 10^{-23}$)	JK^{-1}
T_a, T_B	mean atmospheric temperature, Brightness temperature	K
$L_k^\uparrow(\theta)$	atmospheric upwelling radiance for θ (zenith angle) and channel k (path radiance)	$\text{mWm}^{-2}\text{sr}^{-1}\text{cm}$
L_k^\downarrow	downwelling atmospheric channel radiance	$\text{mWm}^{-2}\text{sr}^{-1}\text{cm}$
τ_k	channel transmissivity (through the atmosphere)	---
$F_r(\theta, \theta_{\text{Sun}}, \phi)$	angular form factor	---
$\theta, \theta_{\text{Sun}}$	satellite zenith angle, solar zenith angle	deg
ϕ	difference between satellite and Sun azimuth angles	deg
$E_{\text{Sun}}^{\text{TOA}}$	TOA solar spectral irradiance (for a channel)	mWm^{-2}cm
E_{Sun}	solar spectral irradiance at ground level (channel)	mWm^{-2}cm
$E_{\text{Sun}}^d(\theta, \theta_{\text{sun}}, \phi)$	diffused downward solar irradiance	mWm^{-2}cm
$E_{\text{Sun}}^s(\theta, \theta_{\text{sun}}, \phi)$	scattered path solar radiance	mWm^{-2}cm
$\rho_r(\theta, \theta_{\text{Sun}}, \phi)$	bi-directional reflectivity	---
α_k, n_k	channel and sensor specific constants for power law	$\text{mWm}^{-2}\text{sr}^{-1}\text{cm}^{-1}\text{K}^{-1}, \text{---}$

Abbreviations

AAC	Autonomous Atmospheric Compensation
AMSU	Advanced Microwave Sounding Unit
APOLLO	AVHRR Processing scheme Over cLOUDs, Land, and Ocean
ASCAT	Advanced Scatterometer
ASTER	Advanced Spaceborne Thermal Emission and Reflection Radiometer
ATSR	Along Track Scanning Radiometer
AVHRR	Advanced Very High Resolution Radiometer
BRDF	Bi-directional Reflection Distribution Function
BT	Brightness temperature
DEM	Digital Elevation Model
DN	Digital Number
ECMWF	European Centre for Medium-Range Weather Forecasts
EPS	EUMETSAT polar system
ERA	ECMWF Re-analysis
ERS	European Remote sensing Satellites
FOV	Field Of View
GAC	Global Area Coverage
GNSS	Global Navigation Satellite System
GOME	Global Ozone Monitoring Experiment
GRAS	GNSS Receiver for Atmospheric Sounding
HIRS	High-resolution IR Radiation Sounder
HRPT	High Resolution Picture Transmission
HRUS	High Rate User Station
IASI	Infrared Atmospheric Sounding Interferometer
IFOV	Instantaneous FOV
IR	Infrared
LAC	Local Area Coverage
LSE	Land Surface Emissivity
LST	Land Surface Temperature
MHS	Microwave Humidity Sounder
MIR	Mid-Infrared
MLS	Mid-Latitude Summer (model atmosphere)
MLW	Mid-Latitude Winter (model atmosphere)
MODIS	MODerate-resolution Imaging Spectroradiometer

MODTRAN	MODerate Resolution Transmittance (radiative transfer calculation code)
MSA	Meteorological Satellite Applications (group)
MSG	Meteosat Second Generation
NDVI	Normalized Difference Vegetation Index
NEM	Normalized Emissivity Method
NESDIS	National Environmental Satellite, Data, and Information Service
NIR	Near-Infrared
NOAA	National Oceanic and Atmospheric Administration
NWP	Numerical Weather Prediction
POES	Polar Orbiting Environmental Satellites
RTC	Radiative Transfer Calculation
RTE	Radiative Transfer Equation
RTM	Radiative Transfer Model
SAS	Sub-Arctic Summer (model atmosphere)
SAW	Sub-Arctic Winter (model atmosphere)
SBUV	Solar Backscatter Ultra-violet (instrument)
SEBASS	Spatially Enhanced Broadband Array Spectrograph System
SEVIRI	Spinning Enhanced Visible and Infrared Imager
SST	Sea Surface Temperature
SWT	Split-Window Technique
TES	Temperature-Emissivity Separation
TIGR	TOVS Initial Guess Retrieval
TIR	Terrestrial Infrared
TIROS	Television and Infrared Observation Satellite
TISI	Thermal Infrared Spectral Indices
TISIE	TISI for Emissivity
TOA	Top Of the Atmosphere
TOVS	TIROS Operational Vertical Sounder
TROP	Tropical (model atmosphere)
UMD	University of Maryland
USGS	Unites States Geological Survey
USS 1976	US standard 1976 (model atmosphere)
UTC	Coordinated Universal Time or <i>Universel Temps Coordonné</i>
WDB	World Data Bank

List of figures

Figure 1: Normalized response functions of NOAA-14 AVHRR channels 3, 4, and 5.....	7
Figure 2: Normalized response functions of MSG-1 SEVIRI channels 5, 10, and 11.....	7
Figure 3: Reflection of solar irradiance from Earth's surface with assumed reflectivity of 0.1 (solid line), and infrared terrestrial emission with assumed emissivity of 0.9 (dashed line). The terrestrial emission is maximum at about $9.7\mu\text{m}$, and reflection of solar irradiance and terrestrial emission are of same order of magnitude at about $3.8\mu\text{m}$	8
Figure 4: Geometry for deriving the fraction of Sun's irradiance that reaches Earth's surface.....	8
Figure 5: Comparison of $B(\lambda, T)$ versus $\partial B/\partial T$ dependant on λ for a blackbody at 300 K; the peaks are at $9.7\mu\text{m}$ and $8\mu\text{m}$ respectively.	9
Figure 6: Surface and TOA brightness temperatures differences (path contribution) as a function of LST, for NOAA-14 AVHRR channels 4 and 5, and MLW and MLS.....	13
Figure 7: Variation of path-radiance related to zenith angle for NOAA-14 AVHRR channel-5 and US standard 1976 model atmosphere.	14
Figure 8: Variation of top-of-the-atmosphere radiance related to NOAA-14 AVHRR channel-5 and US standard 1976 model atmosphere.	14
Figure 9: Regression line for power-law approximation of Planck's law of channel radiance. Equation (34) is employed for NOAA-14 AVHRR channels 3, 4, and 5, for a sampled temperature range of 270-320 K increment. Then n_k is obtained from the slope and α_k is derived from the exponent of the intercept for each of the channels.	25
Figure 10: Annual variation of TOA solar irradiance in AVHRR channel-3 for NOAA12, 14, 15, 16.....	28
Figure 11: NOAA-14 AVHRR input channel emissivities (derived by convolution of ASTER spectral library emissivities with corresponding channel response functions) versus estimated emissivities using the two-channel TISI scheme. Upper panel shows channel-3 emissivity, middle panel shows channel-4 emissivity, and lower panel shows channel-5 emissivity. Surface radiances were simulated for model atmospheres with emissivities of various surface types: (1) coniferous tree, (2) deciduous tree, (3) grass, (4) dry grass, (5) black loam soil, (6) brown silty loam soil, (7) dark brown sand, (8) yellow loamy sand, (9) construction concrete, (10) slate stone shingle (11) white marble, (12) sea water (13) sea foam.....	30
Figure 12: The two-channel TISI method for LSE and LST estimation.....	34
Figure 13: Metop spacecraft configuration with instruments (source: http://www.eumetsat.de).	36
Figure 14: USGS GTOPO30 DEM data over the study area. The black pixels represent the sea-surface and elevation is given in mts. [upper-left: $55^\circ\text{N}-5^\circ\text{E}$ lower-right: $40^\circ30'11.6''\text{N}-20^\circ21'09.4''\text{E}$].....	37
Figure 15: Frequency of distribution of land cover type over the study area.	38
Figure 16: University of Maryland land cover types for the study area. The land cover map is based on the seasonality of vegetation and classifies the surface of the globe into 14 cover types. The area is a part (upper-left: $55^\circ\text{N}-5^\circ\text{E}$ lower-right: $40^\circ30'11.6''\text{N}-20^\circ21'09.4''\text{E}$) of the so-called Italy-window and the data is at the spatial resolution of re-sampled 1 km AVHRR data provided by Institute of Meteorology, FU Berlin.....	39
Figure 17: Cloudmask over the study area for 20.08.1996. The daytime cloudmask is provided by Institute of Meteorology, FU Berlin, and the night-time cloud detection is based on a visual threshold approach.....	41
Figure 18: AVHRR channel 3 land surface emissivities over Europe (20.08.1996). The black pixels in the image represent areas covered by clouds. The gray area on the right hand side of the image are missing data. The emissivity of the sea surface was set to 0.975 (NOAA-14	

AVHRR channel 3 emissivity value from Table 2). [upper-left: 55° N–5° E lower-right: 40°30'11.6" N–20°21'09.4" E]	43
Figure 19: AVHRR channel 4 land surface emissivities over Europe (20.08.1996). The black pixels in the image represent areas covered by clouds. The gray area on the right hand side of the images are missing data. The emissivity of the sea surface was set to 0.990 (NOAA-14 AVHRR channel 4 emissivity value from Table 2). [upper-left: 55° N–5° E lower-right: 40°30'11.6" N–20°21'09.4" E]	44
Figure 20: AVHRR channel 5 land surface emissivities over Europe (20.08.1996). The black pixels in the image represent areas covered by clouds. The gray areas on the right hand side of the image are missing data. The emissivity of the sea surface was set to 0.986 (NOAA-14 AVHRR channel 5 emissivity value from Table 2). [upper-left: 55° N–5° E lower-right: 40°30'11.6" N–20°21'09.4" E]	45
Figure 21: LST map over the study area for 0200 hrs UTC (20.08.1996). The black pixels in the image represent areas covered by clouds or missing data data. [upper-left: 55° N–5° E lower-right: 40°30'11.6" N–20°21'09.4" E]	46
Figure 22: LST map over the study area for 1400 hrs UTC (20.08.1996). The black pixels in the image represent areas covered by clouds or missing data. [upper-left: 55° N–5° E lower-right: 40°30'11.6" N–20°21'09.4" E].....	47
Figure 23: NOAA-14 satellite zenith angles (in degrees) over the study area for 0200 hrs UTC (20.08.1996). The white pixels on the right hand side of the image are areas of no coverage. [upper-left: 55° N–5° E lower-right: 40°30'11.6" N–20°21'09.4" E]	48
Figure 24: NOAA-14 satellite zenith angles (in degrees) over the study area for 1400 hrs UTC (20.08.1996). The white pixels on the right hand side of the image are areas of no coverage. [upper-left: 55° N–5° E lower-right: 40°30'11.6" N–20°21'09.4" E]	49
Figure 25: Sun zenith angles (in degrees) over the study area for 1400 hrs UTC (20.08.1996). The white pixels on the right hand side of the image are areas of no coverage. [upper-left: 55° N–5° E lower-right: 40°30'11.6" N–20°21'09.4" E].....	50
Figure 26: LST difference map for 1400 hrs UTC (20.08.1996). The black pixels represent areas covered by clouds, the light-gray color represents missing data, and the dark-gray pixels represent sea surface and other water bodies. [upper-left: 55° N–5° E lower-right: 40°30'11.6" N–20°21'09.4" E]	51
Figure 27: AVHRR channel 3 LSE (20.08.1996).	54
Figure 28: AVHRR channel 4 LSE (20.08.1996).	54
Figure 29: AVHRR channel 5 LSE (20.08.1996).	54
Figure 30: AVHRR NDVI (20.08.1996).....	54
Figure 31: UMD land cover types.....	54
Figure 32: LST in °C for 0200 hrs UTC (20.08.1996).....	55
Figure 33: LST in °C for 1400 hrs LST (20.08.1996).	55
Figure 34: NOAA zenith (20.08.1996 0200 hrs UTC).	55
Figure 35: NOAA zenith (20.08.1996 1400 hrs UTC).	55
Figure 36: Solar zenith (20.08.1996 1400 hrs UTC).....	55
Figure 37: Elevation in km (USGS GTOPO30 DEM).....	55
Figure 38: AVHRR channel 3 LSE (15.04.1996).	57
Figure 39: AVHRR channel 4 LSE (15.04.1996).	57
Figure 40: AVHRR channel 5 LSE (15.04.1996).	57
Figure 41: AVHRR NDVI (15.04.1996).....	57
Figure 42: LST in °C for 0200 hrs UTC (15.04.1996).....	57
Figure 43: LST in °C for 1400 hrs UTC (15.04.1996).....	57
Figure 44: AVHRR channel 3 LSE (20.04.1996).	59
Figure 45: AVHRR channel 4 LSE (20.04.1996).	59
Figure 46: LST in °C for 0200 hrs UTC (20.04.1996).....	59

Figure 47: LST in °C for 1400 hrs UTC (20.04.1996).....	59
Figure 48: AVHRR NDVI (20.04.1996).....	59
Figure 49: UMD land cover (index as in figure 31).....	59
Figure 50: NDVI values over the study area for 20.08.1996. The white-pixels are missing data, the blue-pixels represent the sea surface and other water bodies, and the dark-gray pixels are areas covered by clouds during daytime (1400 hrs UTC). Vegetated areas are shown as green and non-vegetated areas tend towards red. The image gives an overview of the vegetation distribution over a large part of central Europe [upper-left: 55° N–5° E lower-right: 40°30'11.6" N–20°21'09.4" E].....	62
Figure 51: Vegetation fraction (P_V) derived from NDVI over the study area [upper-left: 55° N–5° E lower-right: 40°30'11.6" N–20°21'09.4" E] for 20.08.1996. The white-pixels are missing data, the blue-pixels represent the sea surface and other water bodies, and the dark-gray pixels represent daytime clouds (1400 hrs UTC) [upper-left: 55° N–5° E lower-right: 40°30'11.6" N–20°21'09.4" E].	64
Figure 52: Regression line for P_V and average LSE. P_V is derived NDVI and average-LSEs are obtained from TISIE derived LSEs. (slope = 0.022; intercept = 0.928; correlation coefficient = 0.28)	65
Figure 53: Regression line between $(1 - P_V)$ and difference in emissivities. P_V is derived from NDVI and LSEs are obtained based on TISIE approach. (slope = -0.0044; intercept = 0.012; correlation coefficient = -0.075).....	65
Figure 54: Regression line for AVHRR channel 1 reflectivity and channel 4 and channel 5 average LSE derived using TISIE. Only pixels with NDVI < 0.15 were considered. (slope = -0.034; intercept = 0.914; correlation coefficient = -0.04).....	65
Figure 55: Regression line for AVHRR channel 1 reflectivity and difference between channel 4 and channel 5 LSE (4 – 5). Only pixels with NDVI < 0.15 were considered. (slope = -0.069; intercept = 0.029; correlation coefficient = -0.12)	65
Figure 56: AVHRR channel 4 land surface emissivities over central Europe (for 20.08.1996) derived from a NDVI-based method combined with channel-1 reflectivities. The light-gray pixels are missing data, the dark-gray pixels represent the sea surface and other water bodies, and the black pixels represent daytime clouds (1400 hrs UTC) [upper-left: 55° N–5° E lower-right: 40°30'11.6" N–20°21'09.4" E].....	66
Figure 57: Emissivity difference map for 20.08.1996 derived by subtracting NDVI-based channel-4 emissivities from TISI-based AVHRR channel-4 emissivities. The black pixels represent area covered by clouds during daytime (1400 hrs UTC), the light-gray color represents missing data, and the dark-gray pixels represent the sea surface and other water bodies [upper-left: 55° N–5° E lower-right: 40°30'11.6" N–20°21'09.4" E].....	67

List of tables

Table 1: MSG-1 SEVIRI channels (5, 10, and 11) emissivity for various surfaces at nadir view. The $\varepsilon(\lambda)$ are reproduced from the ASTER spectral reflectivity library available courtesy of Jet Propulsion Laboratory, California Institute of Technology, Pasadena, Copyright ©1999. The measurements were made from the vertical and emissivities are derived from respective reflectivity values using Kirchoff's law. The channel emissivities ε_k are obtained by convolving $\varepsilon(\lambda)$ with channel response functions [equation (20)].....	19
Table 2: NOAA (12-16) AVHRR channels (3, 4, and 5) emissivity for various surfaces. $\varepsilon(\lambda)$ are reproduced from the ASTER spectral reflectivity library available courtesy of Jet Propulsion Laboratory, California Institute of Technology, Pasadena, Copyright ©1999. The channel emissivities ε_k are obtained by convolving $\varepsilon(\lambda)$ with channel response functions [equation (20)].	20
Table 3: The window channels of MSG-1 SEVIRI, their noise-equivalent temperature differences (NE Δ T), and channel-specific coefficients for the power-law approximation of Planck's law obtained by linear regression.....	26
Table 4: The window channels of NOAA AVHRR, their noise-equivalent temperature differences (NE Δ T), and channel-specific coefficients for the power-law approximation of Planck's law obtained by linear regression.....	26

Appendix 1

Simulated TOA radiances (L_k^{TOA}) at nadir view for a range of surface temperature (T_s), assumed constant emissivity of 0.98 (gray body), and various model atmospheres. For each of the model atmospheres transmissivities (τ_k) and path-radiances (L_k^\uparrow) are also calculated. Surface brightness temperatures (T_B^{sfc}), TOA brightness temperatures (T_B^{TOA}), and surface radiances (R_k) are then extracted from L_k^{TOA} , τ_k , and L_k^\uparrow .

The simulation is made for NOAA-14 AVHRR channels 3, 4, and 5. The temperatures are given in K, the radiances are given in $\text{mWm}^{-2}\text{sr}^{-1}\text{cm}$, and 'C' denotes a channel of AVHRR.

T_s : [T1 = 273.16, T2 = 283.16, T3 = 293.16, T4 = 303.16, T5 = 313.16, T6 = 323.16]

1. Atmosphere: Mid-latitude summer (MLS)												
Lowest air temperature = 294.2 K												
T_s	L_k^{sat}			T_B^{TOA}			R_k			T_B^{sfc}		
	C-3	C-4	C-5	C-3	C-4	C-5	C-3	C-4	C-5	C-3	C-4	C-5
T1	0.211	77.26	94.64	274.11	276.91	278.86	0.197	71.42	85.80	272.81	272.46	272.66
T2	0.310	86.50	102.47	281.96	283.51	284.01	0.321	84.84	100.20	282.66	282.31	282.51
T3	0.457	96.71	110.97	290.41	290.31	289.41	0.505	99.66	115.86	292.61	292.16	292.36
T4	0.670	107.88	120.15	299.26	297.31	294.96	0.771	115.89	132.77	302.56	302.06	302.21
T5	0.972	120.03	130.00	308.31	304.46	300.71	1.148	133.53	150.90	312.56	311.91	312.11
T6	1.389	133.13	140.50	317.56	311.76	306.56	1.668	152.56	170.24	322.51	321.81	321.96
τ_k : 0.801 (C-3), 0.688 (C-4), 0.543 (C-5); $L_k^\uparrow(\theta)$: 0.0524 (C-3), 28.1 (C-4), 48.06 (C-5)												
2. Atmosphere: Mid-latitude winter (MLW)												
Lowest air temperature = 272.2 K												
T_s	L_k^{sat}			T_B^{TOA}			R_k			T_B^{sfc}		
	C-3	C-4	C-5	C-3	C-4	C-5	C-3	C-4	C-5	C-3	C-4	C-5
T1	0.181	69.92	83.68	271.11	271.31	271.16	0.193	70.80	84.85	272.36	271.96	272.01
T2	0.288	82.44	96.43	280.46	280.66	280.06	0.314	84.24	99.26	282.26	281.86	281.91
T3	0.448	96.25	110.28	289.96	290.01	288.96	0.495	99.07	114.92	292.21	291.81	291.81
T4	0.680	111.38	125.24	299.56	299.41	297.96	0.759	115.31	131.83	302.16	301.71	301.71
T5	1.007	127.81	141.28	309.21	308.86	306.96	1.130	132.95	149.97	312.11	311.61	311.61
T6	1.459	145.55	158.37	318.86	318.26	316.01	1.643	151.10	169.30	322.06	321.56	321.51
τ_k : 0.8809 (C-3), 0.9315 (C-4), 0.8844 (C-5); $L_k^\uparrow(\theta)$: 0.0113 (C-3), 3.97 (C-4), 8.65 (C-5)												

3. Atmosphere: Sub-arctic summer (SAS) [Lowest air temperature = 287.2 K]

T_s	L_k^{sat}			T_B^{TOA}			R_k			T_B^{sfc}		
	C-3	C-4	C-5	C-3	C-4	C-5	C-3	C-4	C-5	C-3	C-4	C-5
T1	0.192	72.33	87.47	272.31	273.16	273.91	0.196	71.11	85.35	272.51	272.21	272.36
T2	0.294	83.08	97.37	280.91	281.11	280.66	0.319	84.54	99.76	282.56	282.11	282.21
T3	0.446	94.95	108.14	289.86	289.16	287.61	0.501	99.36	115.43	292.51	291.96	292.11
T4	0.666	107.94	119.76	299.06	297.36	294.71	0.767	115.60	132.33	302.46	301.86	302.01
T5	0.977	122.06	132.23	308.41	305.61	301.96	1.142	133.24	150.47	312.41	311.76	311.86
T6	1.406	137.31	145.52	317.86	313.96	309.26	1.660	152.28	169.80	322.36	321.66	321.76

τ_k : 0.8288 (C-3), 0.8005 (C-4), 0.6875 (C-5); $L_k^\uparrow(\theta)$: 0.0301 (C-3), 15.41 (C-4), 28.79 (C-5)

4. Atmosphere: Sub-arctic winter (SAW) [Lowest air temperature = 257.2 K]

T_s	L_k^{sat}			T_B^{TOA}			R_k			T_B^{sfc}		
	C-3	C-4	C-5	C-3	C-4	C-5	C-3	C-4	C-5	C-3	C-4	C-5
T1	0.179	69.80	83.46	270.86	271.21	271.01	0.191	70.73	84.78	272.21	271.91	271.89
T2	0.288	82.79	97.13	280.46	280.86	280.51	0.312	84.17	99.12	282.16	281.81	281.82
T3	0.451	97.12	111.99	290.16	290.56	290.01	0.493	99.10	114.79	292.11	291.76	291.71
T4	0.689	112.82	128.03	299.86	300.26	299.56	0.754	115.24	131.70	302.06	301.66	301.61
T5	1.024	129.87	145.23	309.61	309.96	309.11	1.124	132.88	149.83	312.01	311.56	311.53
T6	1.487	148.28	163.56	319.41	319.66	318.66	1.635	151.92	169.17	321.96	321.51	321.45

τ_k : 0.9064 (C-3), 0.9666 (C-4), 0.9484 (C-5); $L_k^\uparrow(\theta)$: 0.0050 (C-3), 1.43 (C-4), 3.13 (C-5)

5. Atmosphere: US standard 1976 [Lowest air temperature = 288.2 K]

T_s	L_k^{sat}			T_B^{TOA}			R_k			T_B^{sfc}		
	C-3	C-4	C-5	C-3	C-4	C-5	C-3	C-4	C-5	C-3	C-4	C-5
T1	0.190	71.34	86.15	272.11	272.41	272.96	0.194	70.94	85.09	272.51	272.07	272.16
T2	0.294	83.18	97.71	280.96	281.16	280.91	0.316	84.37	99.50	282.42	281.96	282.05
T3	0.450	96.26	110.29	290.11	290.01	288.96	0.499	99.20	115.17	292.36	291.87	291.95
T4	0.676	110.58	123.85	299.46	298.91	297.16	0.763	115.43	132.08	302.31	301.79	301.82
T5	0.996	126.14	138.40	308.91	307.91	305.41	1.136	133.08	150.21	312.26	311.67	311.72
T6	1.436	142.93	153.92	318.46	316.91	313.71	1.652	152.12	169.54	322.22	321.60	321.64

τ_k : 0.8550 (C-3), 0.8819 (C-4), 0.8024 (C-5); $L_k^\uparrow(\theta)$: 0.0243 (C-3), 8.7771 (C-4), 17.8766 (C-5)

6. Atmosphere: one of the TIGR 1996 tropical profiles [Lowest air temperature = 296.86 K]

T_s	L_k^{sat}			T_B^{TOA}			R_k			T_B^{sfc}		
	C-3	C-4	C-5	C-3	C-4	C-5	C-3	C-4	C-5	C-3	C-4	C-5
T1	0.223	81.37	99.59	275.26	279.86	282.16	0.199	71.65	86.09	272.96	272.63	272.88
T2	0.319	89.20	105.65	282.61	285.31	286.06	0.323	85.07	100.49	282.86	282.46	282.70
T3	0.462	97.84	112.24	290.66	291.01	290.16	0.508	99.88	116.15	292.79	292.32	292.53
T4	0.670	107.30	119.36	299.21	296.96	294.51	0.776	116.11	133.05	302.72	302.19	302.39
T5	0.962	117.58	126.99	308.06	303.06	298.96	1.155	133.74	151.18	312.67	312.05	312.24
T6	1.366	128.68	135.13	317.11	309.31	303.56	1.677	152.77	170.52	322.63	321.92	322.11

τ_k : 0.7737 (C-3), 0.5831 (C-4), 0.4209 (C-5); $L_k^\uparrow(\theta)$: 0.0689 (C-3), 39.5937 (C-4), 63.3554 (C-5)

Acknowledgements

When I undertook this task of deriving emissivity and temperature of the Earth's surface as my Ph.D. topic, I expected it might be more daunting than it appears. Looking back at all the stages, where there were numerous scopes to introduce errors, I wonder if any work of this type ever reaches a completion without professional support.

It is a matter of pleasure for me to give foremost thanks to the following persons:

Prof. Dr. Herbert Fischer (Institute of Meteorology and Climate Research-IMK, Forschungszentrum Karlsruhe, University of Karlsruhe), the supervisor of this thesis, for advising the thesis, sharing his profound knowledge on radiation Physics and Remote Sensing, and providing me the opportunity to undertake this thesis-work. I thank Prof. Dr. Christoph Kottmeier, the co-supervisor of this thesis, for his interest in my work, and for some useful discussions when I attended one of his lectures in Meteorology.

Folke-S. Olesen, the leader of the Meteorological Satellite Applications group, where I performed this job, for his pivotal scientific guidance and accurate role as a group leader.

Frank M. Göttsche, for sharing his high analytical abilities, numerous timely discussions about the subject, and for being an excellent office-mate.

Walter Fiebig, the system administrator at the MSA group, for ever-willing jovial attitude to render assistance, even for non computer-related problems.

Many thanks to D. Koslowsky, Free University of Berlin for pre-processing of AVHRR data. The ECMWF analyses model atmosphere data was provided by DWD (*Deutscher Wetterdienst*: German Weather Service). The USGS GTOPO30 DEM was available from EDC DAAC, Sioux Falls. The ASTER spectral reflectance library was available courtesy of JPL, California Institute of Technology, Pasadena. The UMD global 1 km land cover type data was available courtesy of University of Maryland. The radiative transfer model MODTRAN-3.7 was available free of charge from the Air Force Research Laboratory (AFRL), Hanscom AFB, MA.

It is indeed very much gratifying when you reach out to busy professionals seeking their assistance and receive a generous response. I wish to thank the colleagues, scientists, and professors, who have been keeping interest in my work and have provided me assistance, even from a distance, whenever it was required.

I am thankful to the secretaries of the IMK (Mrs. Wiessner, Mrs. Böttcher, and formerly Mrs. Wortmann) for their helpful attitude in solving many of the administrative processes and to all my IMK colleagues who kept interest in my work and have been supportive in one way or the other. Special thanks to colleagues who have pursued or are pursuing Ph.D. at IMK as they were generous to share their valuable experience.

My sincere thanks to my parents, guardians, friends, well-wishers, near and dear ones, and the guiding souls who have been supportive throughout the whole time in their own ways. The occasions of receiving assistance and help are numerous and it is difficult to mention all, hopefully, each will understand his or her own part of contribution.

Thank You All !